# Joint Pattern and Polarization Synthesis in Active Phased Arrays

## Design and Optimization Strategies

Eren Hamamcı

Delft University of Technology

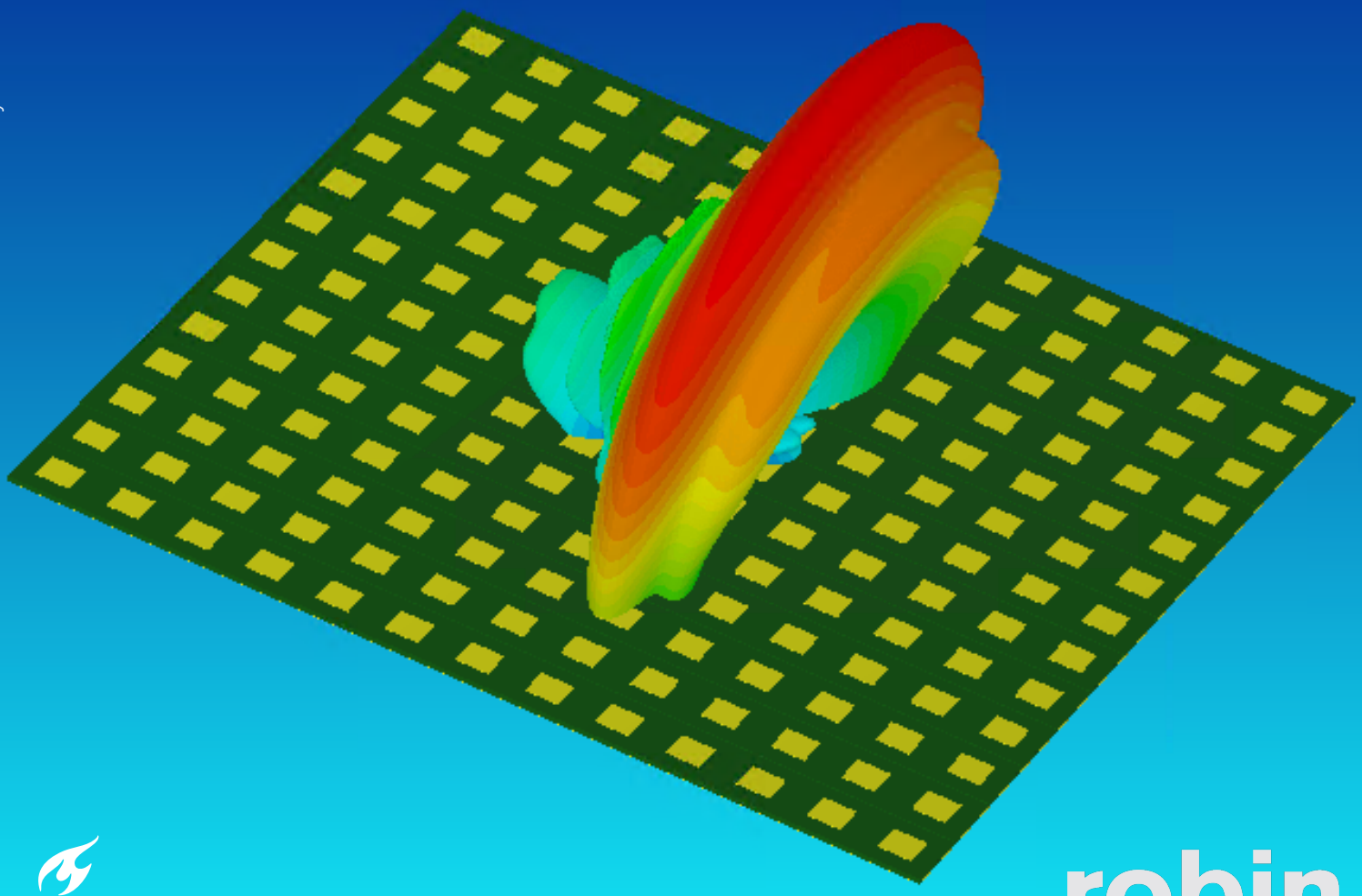

TU Delft

robin
radar systems

# Joint Pattern and Polarization Synthesis in Active Phased Arrays

## Design and Optimization Strategies

to obtain the degree of Master of Science

at the Delft University of Technology,

to be defended publicly on Wednesday July 2, 2025 at 15:30 PM.


| | | |
|---|---|---|
| Student number: | Eren Hamamcı | 6003222 |
| Project duration: | November 18, 2024 – July 2, 2025 | |
| Thesis committee: | Prof. dr. A. Yarovoy, | TU Delft |
| | Dr. Y. Aslan, | TU Delft, supervisor |
| | Dr. G. Joseph, | TU Delft |
| | G. Theis, | Robin Radar Systems, supervisor |


| | |
|---|---|
| First Supervisor: | Dr. Yankı Aslan |
| Industry Supervisor: | Mr. Guilherme Theis |
| Industry Partner: | Robin Radar Systems |
| Project Duration: | November, 2024 - June, 2025 |
| Faculty: | Faculty of Electrical Engineering, Delft |

Cover: A Polarimetric Phased Antenna Array

TU Delft

robin radar systems

# Acknowledgment

They say no one reads the acknowledgment, except the people who were part of the journey. So, if you are here, thank you: You have helped me survive this journey.

My dear family, without your endless support, this journey would be unimaginable. Your kindness and constant willingness to give provided comfort and encouragement along the way.

Prof. Olexander Yarovyi, your presence has been a source of motivation for all of us. Your unique way of approaching problems has truly broadened my perspective.

Dr. Yankı Aslan, your calm presence and patience were the most important forces behind this work. Whenever I needed help, you were there to support me with your boundless knowledge. Your support went far beyond what was expected; you generously offered your time for countless meetings, even on very short notice.

Mr. Guilherme Theis, your constant support and guidance have truly shaped this work. Throughout this journey, there were many moments when I struggled or failed to understand. Yet instead of stepping back, you continued to believe in me and offered your support when I needed it most.

Dear friends in Turkey, although we have not been physically close in the last two years, I have always felt your presence by my side. You were always there whenever I needed motivation.

Dear friends whom I have met along the way, although we come from different cultures, we have always managed to find common ground to connect and laugh. Your good company made this journey not only easier but also far more enjoyable.

Finally, I would like to thank all the colleagues, instructors, and friends from MS3 and Robin Radar Systems. Your feedback, insights, and innovative ideas have significantly improved the quality of this work.

*Eren Hamamcı*
*Delft, June 2025*

# Summary

Polarimetric Phased Antenna Arrays (PPAA) are widely used in many applications ranging from cellular and satellite communications to automotive and weather radars. To operate the phased array adaptively for the generation of multiple polarization states, the gain and phase of each antenna element (or each port in case of multiport antennas), so called the beamforming weights, have to be optimized. The optimization is performed based on the defined pattern goals and constraints such as the co- and cross- polarization gains and maximum side-lobe levels. By all means, the optimization of complex beamforming weights depends on the architecture of the phased array. Since a PPAA might consist of thousands of antennas, low-cost architectures, requiring a lower number of RF chains, are studied by the researchers through element polarization optimization techniques. Although low-cost solutions considerably lower the cost and complexity of a PPAA, they deteriorate the polarimetric performance of the array due to the lack of optimization studies considering polarimetry.

In this thesis, optimization strategies for low-cost PPAAs are discussed. It is found that the state of the art optimization algorithms limit the operation of a low-cost PPAA to two polarization states, and the polarimetric performance of the array deteriorates substantially for any other polarization state. However, the synthesis of more polarization states from a single array may be demanded for performance enhancement. A new optimization algorithm, mainly using convex optimization, is proposed to extend the capabilities of a low-cost PPAA to three polarizations with a minimal trade-off in the remaining two polarizations. It is shown that for a 16 by 16 ideal planar low-cost PPAA, the EIRP of an arbitrary third polarization (in addition to H and V) can be improved by $3$ dB with a negligible loss in H and V, compared to the state of the art algorithms. Moreover, the low-cost PPAA is simplified even further through subarraying. A new subarrayed architecture, built on the low-cost topology, is proposed along with a novel optimization strategy to further lower the cost of a PPAA. It is shown that with only a $1$ dB loss of EIRP in H and V, a low-cost PPAA can be subarrayed. Lastly, the pattern synthesis problem for low-cost PPAAs is discussed. To maintain polarization purity and the overall pattern shape, the cross-polarized field is also subjected to shaping constraints. The joint pattern and polarization synthesis are explained for the dual-polarized and low-cost architecture, full-wave simulations are integrated into the optimization, and effectiveness of the proposed algorithms are verified. It is shown that for a 13 by 13 array, the co-polarized field can be shaped with a maximum ripple size of $\pm 1$ dB, and the cross-polarized field can be suppressed more than $40$ dB with respect to the mask shape.

# Contents

# Nomenclature

## Abbreviations

| Abbreviation | Definition |
|---|---|
| PPAA | Polarimetric Phased Antenna Array |
| RF | Radio Frequency |
| IC | Integrated Circuit |
| SDR | Semidefinite Relaxation |
| RFFE | RF - Front End |
| SNR | Signal to Noise Ratio |
| AEP | Active Element Pattern |
| ML | Mainlobe |
| SL | Sidelobe |
| EIRP | Effective Isotropic Radiated Power |
| H | Horizontal Polarization |
| V | Vertical Polarization |
| LHCP | Left Hand Circular Polarization |
| XPL | Cross-Polarization Level inside the mainlobe |
| SLL | Sidelobe Level |
| PA | Polarization Averaging |
| CPS | Common Polarization Suppression |
| GSPD | Gain Shared - Phase Decoupled Tiles |
| FGPD | Fixed Gain - Phase Decoupled Tiles |

# 1

# Introduction

## 1.1. Motivation

In modern wireless systems, active polarimetric phased array antennas (PPAA) are widely used to receive and transmit waves with the desired direction, polarization, and shape. As active phased arrays do not need to be mechanically rotated, they attract the attention of various domains, such as telecommunications, weather radars, automotive radars, and tracking. By properly adjusting the amplitudes and phases of the antennas in the array, beamforming can be performed. In many scenarios, the transmitted beam is expected to have a certain and adjustable polarization state with minimal leakage to other polarization states, which can be used for classifying targets or enhancing the quality of service.

In weather radar applications, polarimetric information is used to classify precipitation particles based on their sizes, shapes, and orientations [1]. Generally, weather sensing is performed through the transmission of two orthogonal polarization states: horizontal (H) and vertical (V) polarizations. The H and V directions correspond to the angular unit vectors in a spherical coordinate grid. By alternately transmitting H and V, the polarimetric scattering matrix (**S**) can be generated, whose diagonal elements show the power of each polarimetric channel. Using the **S** matrix, differential reflectivity ($Z_{DR}$) and the correlation coefficient ($\rho_{HV}$) can be estimated, which can then be used for particle classification. An important thing to consider in the measurements is the purity of the synthesized beam; If the transmitted beam has low purity (e.g., high cross-polarization levels), there will be polarimetric bias in the measurements, resulting in off-diagonal elements of **S** to have high values and poor classification of the particles. In addition to weather radars, polarimetric information is used in automotive radars for target classification. By exploiting polarimetric measurements, road surfaces can be identified and traffic signs can be detected in any weather condition, assisting the autonomous drive.

Although sensing of precipitation particles is usually performed by alternately transmitting the H and V polarizations, obtaining all possible polarimetric information requires the retrieval of nine degrees of freedom. To retrieve nine degrees of freedom, at least three different polarization states must be transmitted in an alternating fashion [2]. This method is referred to as 3Pol1D in the weather radar literature [3–5]. Compared with the traditional methods, 3Pol1D allowed better estimation of rainfall rates, classification of hydrometeors with lower ambiguity, and robustness to measurement errors. Although it has many advantages, 3Pol1D is not widely used in weather radars as it requires complex hardware and a measurement scheme. As explained, for the utilization of 3Pol1D, a phased antenna array is expected

to be agile for at least three different polarization states while still maintaining the polarization purity and the required gain for the wireless link.

In addition to sensing applications, the synthesis of multiple polarization states is also useful for telecommunications. In communications, attention is given to increasing the capacity of a wireless link and using the spectrum as efficiently as possible at the same time. According to Shannon-Hartley Theorem, the capacity of a wireless link can be given as follows: $C = B \cdot log_2(1 + SNR)$, where $C$ represents the capacity, $B$ is the bandwidth of the wireless link, and $SNR$ is the signal-to-noise ratio of the channel. Since the spectrum is a limited resource and $SNR$ of the channel is an independent variable, increasing the capacity of a channel is not trivial. By exploiting polarization diversity, two orthogonal polarizations can be transmitted, and the capacity of the channel can be doubled without increasing the bandwidth:

$$C = B \cdot \{log_2(1 + SNR_H) + log_2(1 + SNR_V)\} \tag{1.1}$$

In fact, recent theoretical studies have also shown that channel capacity can be further tripled by transmitting three different electric field vectors [6].

A particular interest for the use of three polarization states is in dealing with transmitter and receiver misalignment in a dynamic communication link. When the transmitter and receiver are not aligned with each other, a polarization mismatch occurs, the received power decreases considerably, and the signal might not even be detected. In such a scenario, a tri-polarized antenna system can align the transmitter to the receiver through a dynamic feedback system through signal processing. Therefore, there is a clear need for the synthesis of at least three different polarization states as is demanded by several applications.

Although modern PPAAs have polarization agility (can synthesize three or more polarizations), they are complex and expensive, motivating the need for the synthesis of three polarization states without employing complex dual-polarized elements. By employing dual-polarized antenna elements across the array, polarization agility and purity can be easily achieved. Although employing dual-polarized elements might seem to be a straightforward solution, they need to be excited from at least two different ports independently, meaning that each port of an antenna element requires separate radiofrequency (RF) components, such as pre-drivers, low noise amplifiers, analog to digital converters, and corresponding matching circuitries at high frequencies. Despite the many examples of such arrays, they are costly, hard to calibrate, and generate a lot of heat because of the large number of RF components. An example of such a complex RF architecture can be seen in Fig. 1.1, where the circuit diagram of a single module of a polarization agile receiver is presented [7].

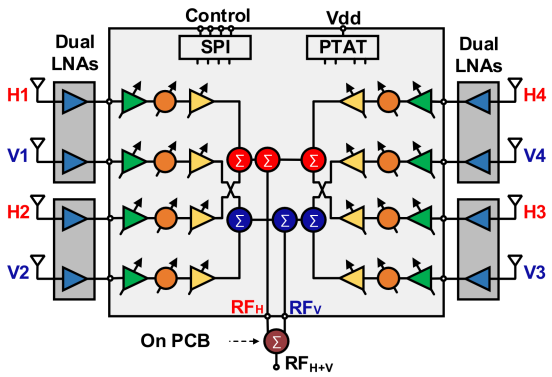


**Figure 1.1:** RF architecture of a polarization agile 256-element Ku-Band SATCOM receiver

## 1.2. Problem Formulation

As demanded by several different applications, there is a clear need for the synthesis of multiple, specifically three (e.g. three: H, V, and circular or slant), polarization states by the same array. As stated above, through the use of a dual-polarized array, any desired polarization can be synthesized as there is full amplitude and phase control on each port. However, this requires that each antenna port employs a separate RF chain along with separate RF components, resulting in complex hardware. Recently, an element polarization optimization technique was proposed in [8], which significantly reduces the complexity of the array by combining the H, V ports of each dual-polarized element into a single RF chain (see Fig. 1.2b). The fixed phase shift (or time delay) at the V-port of an element determines its polarization state. Comparing Fig. 1.2a (conventional&complex RF architecture) and Fig. 1.2b, it can be seen that the number of RF components nearly reduces to half, significantly decreasing the complexity and cost of the array. For PCB-based phased arrays with beamformer integrated circuits (IC), the required number of chips will be half of the conventional architecture.

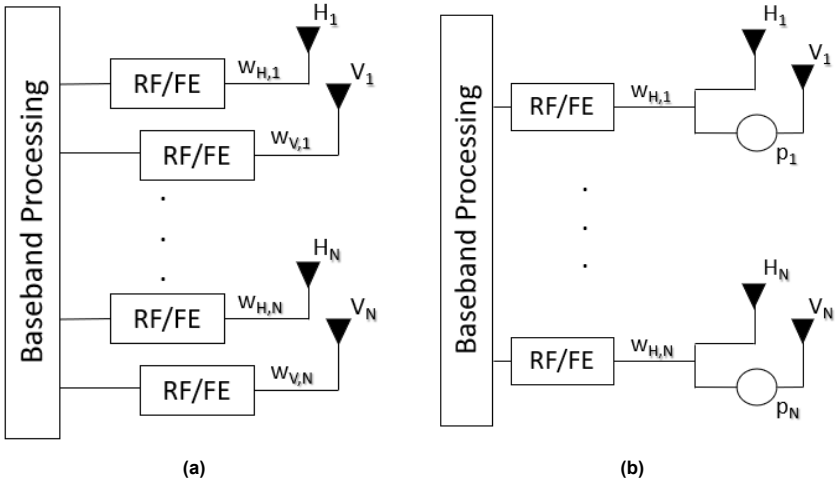


**Figure 1.2:** Polarimetric phased array architectures: (a) conventional, (b) low-cost with optimally polarized elements (RF/FE: RF front-end, $p_1, ...p_N$ are fixed).

The optimization framework proposed in [8] demonstrated that by optimizing fixed phase shifters at V-ports, and digital weights in baseband, two (H and V) polarizations can be generated by the low-cost topology in Fig. 1.2b, with similar gain, side-lobe, and cross-polarization performance of the conventional topology in Fig. 1.2a. The work in [8] demonstrated that the performance of the low-cost topology significantly deteriorates when a third (e.g., slant, circular) polarization is tried to be synthesized, as the array is not reconfigurable in the analog domain (phase shifts are fixed). It is found that the optimization framework demonstrated in [8] results in a considerable loss of directivity and Effective Isotropic Radiated Power (EIRP) for the third polarization state. The reasons for the significant loss of EIRP are constraints on the Side-Lobe Levels (SLL) and cross-polarization requirements (expected to be less than $-45$ dB for purity) inside the main-lobe. To satisfy these requirements, the optimization algorithm applies a taper on the beamforming weights, considerably reducing the EIRP and the range of the PPAA. To avoid this, a phase-only beamforming approach (applying full power at each port with optimized phases) could have been preferred, but that would further limit the freedom of already low-cost topology, and SLL&cross-polarization constraints would not be met. Therefore, there is a need for an optimization strategy that can make the low-cost topology in Fig. 1.2b synthesize a third polarization (in addition to H and V) without a significant loss of EIRP and meeting the required constraints at the same time.

Although the low-cost architecture reduces the cost of the PPAA by a large amount compared to the conventional architecture, complexity in Fig. 1.2b is still considerably high. In regular phased arrays with single-port antennas, it is common practice to divide the array into subarrays and lower the number of RF chains. Despite the optimization of subarrayed architectures being a trending research topic, its application to PPAAs is not common. Therefore, a novel optimization strategy is needed to decompose a PPAA into subarrays, which can lower the cost of the low-cost PPAA further. However, as the beamforming capabilities of the array will weaken after subarraying, polarimetric performance has to be maintained. The optimization algorithm has to preserve the polarimetric performance of the subarrayed architecture with a little compromise compared to the performance of the low-cost topology in Fig. 1.2b and the conventional dual-polarized architecture.

In addition to the cost and complexity of a phased array, pattern synthesis is a frequently faced problem in phased arrays. Despite the use of a shaped pattern is common for conventional phased arrays, its implementation to PPAAs is not widespread. Most of the current optimization algorithms that are trying to jointly synthesize pattern and polarization cannot maintain the purity of the polarization for a shaped beam. Besides, there is no application of it to low-cost PPAAs. Consequently, an optimization algorithm that is adaptable to low-cost PPAAs and capable of maintaining polarization purity is required for the joint pattern shaping and polarization synthesis.

Furthermore, mutual coupling effects are generally ignored in most of the studies regarding shaping, polarization synthesis, and subarraying. However, performing the optimization without coupling effects might considerably deteriorate the performance when the array is excited with those weights. Therefore, coupling effects must be included in all optimizations to avoid deterioration of polarimetric performance.

## 1.3. Scope of Research

The scope of this research is primarily based on novel optimization strategies to achieve PPAAs with low-cost topologies, such as the one shown in Fig. 1.2b. Other possible ways of generating a low-cost PPAA could be utilizing polarization switches or through tiling of the array with subarrays. Polarization switches that enable the alteration of the port used at a specific instant are not considered within the scope of this thesis, as the novelty is primarily on the optimization rather than the design. Tiling of the aperture through subarrays has been considered in this work with several constraints. It is assumed that the tile sizes and shapes are fixed, and the optimization variables are the orientations and placements of the tiles, along with the complex beamforming weights.

Another important topic covered within the scope of this work is the shaping of the transmitted wave while considering the polarization requirements. Shaping of the transmitted wave is widely used, especially in radar applications. The beam shaping intends to impinge an equal amount of power on each target so that the classification of the targets can be accurate. Throughout beam shaping, tiling is not considered, and the array is assumed to have the low-cost topology shown in Fig. 1.2b. Unlike the most of literature, shaping of the beam pattern is performed solely on the elevation plane, and the steering of the shaped pattern is performed on the azimuthal plane.

Although coupling effects are mostly considered inside optimization algorithms, all the other nonlinearities regarding the circuitry and RF components are neglected in this thesis. For instance, beamforming IC outputs are assumed to be ideal, losses due to the feeding circuitry and RF components are neglected, and distortions due to amplitude-phase coupling are not considered.

Through the derivations and simulations, 1D and 2D planar arrays are considered; conformal and 3D arrays are not discussed within the scope of this work. However, with slight adjustments in the field

equations, optimization strategies can be generalized to any array or antenna element type.

## 1.4. Literature Review

The problem of pattern and polarization synthesis in active-phased arrays is a hot research topic. Although there are some algorithms for polarization synthesis, it has been found that the algorithms are primarily based on pattern synthesis without considering the polarization requirements. Studies that consider polarization synthesis can be grouped according to the complexity of the architecture that they require from the array. In other words, some of the algorithms utilize single-polarized antennas with a single RF chain per element, whereas some algorithms require complex dual or tri-polarized architectures with at least two RF chains per element. In addition to polarization requirements, few works consider pattern shaping and polarization synthesis jointly; however, they require dual-polarized antenna elements.

### 1.4.1. Single-Polarized Antenna Elements

In this section, algorithms that are based on the usage of single-polarized antenna elements, and therefore a single RF chain per element, are examined. These studies demonstrate that, in general, PPAAs with single-optimally polarized elements can synthesize at most two polarization states with acceptable polarimetric performance. It is found that studies employ different algorithms, such as convex optimization, numerical algorithms, genetic algorithms, and iterative algorithms. As the problem dealt with can be put into a convex format, convex optimization is widely used across studies. In fact, compared to other algorithms, convex optimization approaches to the optimal solution faster. This is why, as part of the optimization framework, convex optimization is preferred in [8] after finding the polarization states of the individual elements. However, as detailed in Section 1.2, their algorithm can only be used to synthesize H and V with acceptable polarimetric performance, since it results in a considerable EIRP loss for any third polarization.

In addition to polarization synthesis, convex optimization is further used for pattern shaping in [9]. To deal with the pattern and polarization requirements jointly, semidefinite relaxation (SDR) has been used. It must be noted that SDR does not necessarily find the optimal solution to the problem, but rather attains a suboptimal solution satisfying the constraints of the system. The strategy presented in [9] is to suppress cross-polarization below $-30$ dB and shape the co-polarized component, resulting in an overall field close to the shaped co-polarized component. However, the algorithm presented in [9] is limited to a single linear polarization.

A numerical pattern synthesis algorithm has been implemented in [10] that iteratively searches for a beamformer until the cross-polarization and purity requirements are met. This algorithm does not employ dual-polarized elements, making the array low-cost, and it searches for the ideal boundaries (main-lobe and side-lobe regions) itself; unlike convex optimization algorithms, where boundaries have to be set by the user through a direct search. The disadvantage of the algorithm is that the synthesized polarization depends on the polarization of the antenna element, meaning that the array can synthesize only a single polarization without reconfiguring the antenna.

A novel rotation and phase optimization technique is presented in [11], where planar antenna elements are physically rotated (see Fig. 1.3) and excited for joint pattern and polarization synthesis. As it does not require a complicated feed network, a phase-only beamforming approach is preferred. To jointly solve for the rotation angles and phases, particle swarm optimization (PSO) is used. It must be noted that, unlike any of the previous cases, mutual coupling between elements will change as they are rotated, which is taken care of by integrating full-wave simulations into the optimization problem.

After rotations are updated at each step, active element patterns (AEP) are re-simulated and updated. The objective function of PSO contains the weighted sum of non-linear terms regarding the shape of the pattern and polarization purity, making it complex. Although the suggested algorithm uses single-polarized antennas, it can be used to synthesize any polarization. However, once the array is optimized, it cannot be used to synthesize any other polarization as the element orientations will be fixed. Moreover, physically rotating elements complicates the manufacturing process (increasing the array cost), and the optimization process takes a couple of hours.

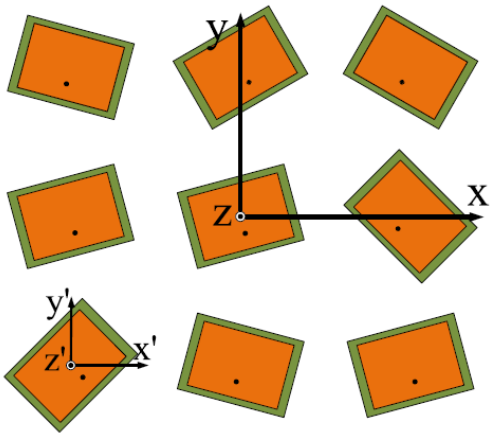


**Figure 1.3:** Physically rotated patch antennas

### 1.4.2. Dual &Tri-Polarized Antenna Elements

Contrary to the previous section, studies that are explained in this part are polarization agile, but they require the use of dual-polarized elements with at least two RF chains, or they require complex element designs. Unlike [8], where the objective function is based on maximizing the gain of the co-polarized component, [12] uses the objective function of the convex problem to perfectly meet the polarization requirements. Through the relations between electric field components (E-field), constraints on the axial ratio can be set, which can help to perfectly synthesize any linear, circular, or elliptic polarization state with a focused beam. Similar to [12], the research in [13] suggests the use of sequential convex optimizations for polarization synthesis. A sequential approach is preferred in [13] to relax the polarization constraints and reduce the required number of antennas. The main studies considering polarization synthesis are briefly reviewed below.

In addition to the polarization agile focused beam synthesis technique explained in [12] and [13], pattern shaping along with polarization synthesis is explained in [14]. Constraints of the optimization are solely used to suppress the peak SLL and arrange the axial ratio. Unlike [12], the objective function of [14] is used to shape the pattern; however, pattern shaping constraints do not define a convex set by nature and must be adjusted to be solved by convex optimization. To convert the problem into a convex format, an iterative approach is preferred, where the shaping constraints are rewritten in terms of the power pattern, and constraints in quadratic form are treated as linear through the iterations. Although [12] and [14] suggest algorithms that can synthesize any polarization, and even synthesize the pattern, they require dual-polarized antenna elements, increasing the complexity; similarly, [13] requires the use of even more complex tri-polarized antenna elements.

As mentioned before, many studies have utilized convex optimization through different aspects as a tool to solve for beamforming coefficients. [15] used linear algebra as a tool to generate the solution

space for the problem with the aim of removing the axial ratio from the objective function and achieving a lower peak SLL while still satisfying the polarization requirements. The beamforming weight vector is expressed through the polarization requirement in a certain direction:

$$\mathbf{w}_p = \mathbf{Q}\eta, \quad \mathbf{Q} = \begin{bmatrix} \mathbf{q}^T \\ \mathbf{I} \end{bmatrix} \tag{1.2}$$

where $\mathbf{w}_p$ is the $N$ by $1$ beamforming vector, $\mathbf{Q}$ is an $N$ by $(N-1)$ matrix containing polarization requirements, $\eta$ is a $(N-1)$ by $1$ coefficient vector to be solved, and $\mathbf{I}$ is an $(N-1)$ by $(N-1)$ identity matrix. It is clear that $\mathbf{Q}$ has a rank of $(N-1)$ whose column space spans the subspace of the excitation domain satisfying the polarization requirements. For any coefficient vector $\eta$, polarization requirements can be satisfied. It is claimed that with this strategy, a lower peak SLL can be obtained while perfectly satisfying polarization requirements. However, it is observed that this method cannot be implemented in the low-cost topology given in Fig. 1.2b, and as before, dual-polarized antenna elements are required.

An implementation of a genetic algorithm is presented in [16] for weather radars with multiple simultaneous transmit beams. Since the genetic algorithm can handle non-linear and non-convex constraints, phase-only beamforming is demonstrated, increasing the EIRP of the radar. It has been shown that multiple beams with pre-defined locations can be generated while satisfying the cross-polarization requirements expected from weather radars. Moreover, although the synthesis of H and V are demonstrated in the work, the algorithm can be extended to other polarizations as the considered PPAA is fully polarized. However, as with the previous cases, dual-polarized antenna elements are utilized.

**Table 1.1:** Overview of the studies considering polarization synthesis, grouped according to element polarizations.

| | Ref. # | Beam type | Polarization type | Control Parameters | SLL constraint | XPL constraint |
|---|---|---|---|---|---|---|
| **Dual-polarized antenna elements** | [12] | Focused | Multiple, arbitrary | Amplitude, phase | ✓ | ✓ |
| | [14] | Shaped | Multiple, arbitrary | Amplitude, phase | ✓ | ✓ |
| | [15] | Focused | Multiple, arbitrary | Amplitude, phase | ✓ | ✓ |
| | [16] | Comb-like | Multiple, arbitrary | Phase | ✓ | ✓ |
| **Tri-polarized antenna elements** | [13] | Focused | Multiple, arbitrary | Amplitude, phase | ✓ | ✓ |
| **Single-polarized antenna elements** | [8] | Focused | Two, fixed | Amplitude, phase | ✓ | ✓ |
| | [9] | Shaped | Single, fixed | Amplitude, phase | ✓ | ✓ |
| | [10] | Focused | Single, fixed | Amplitude, phase | ✓ | ✓ |
| | [11] | Shaped | Single, arbitrary | Rotation, phase | ✓ | ✓ |
| | This work | Focused or Shaped | Three, fixed | Amplitude, phase | ✓ | ✓ |

From the literature (see Table 1.1), it can be seen that there are many ways of synthesizing polarization and pattern, and a few methods for doing it jointly. However, it is clear that achieving agility in polarization with or without pattern synthesis requires the use of dual-polarized elements. There are also optimization methods based on low-cost topologies (single feed per radiator); however, they can synthesize at most two polarization states while meeting the purity and EIRP criteria. Furthermore, mutual coupling between antenna elements is generally ignored in the polarimetric optimization procedure.

## 1.5. Research Objectives

From the state of the art, it is clear that there are lacking points and challenges associated with each technique, and the following gaps from the literature will be primarily addressed as the objective of this research:

- **Increased polarization agility:** As detailed in Section 1.2, the algorithm described in [8] can synthesize H and V polarizations without resulting in a significant EIRP loss (compared to a conventional fully-polarized array) and maintaining polarization purity. However, as motivated, there is a demand for the synthesis of a third polarization in addition to H and V. Therefore, a new optimization strategy that will increase the directivity and EIRP of an arbitrary third polarization, for the low-cost topology given in Fig. 1.2b, will be explained.
- **Subarray tiling optimization:** Complexity and the cost of a phased array can be further reduced by subarray tiling. However, tiling will further reduce the freedom in beamforming, which was already reduced after combining both ports of the antenna into a single RF chain. Tiling will also be included in the optimization framework, but the shape and size of the tiles will remain fixed.
- **Joint pattern and polarization synthesis:** Pattern shaping along with polarization synthesis will be performed. It is observed that there is a demand for pattern shaping even in the case of polarization synthesis, especially by weather radars. Pattern synthesis for the low-cost topology will be carried out through novel optimization methods.
- **Inclusion of Coupling Effects into Optimization:** Most of the studies neglect the coupling effects between ports (and radiating surfaces) and assume isotropic radiation, which might deteriorate the performance of an actual PPAA. Through full-wave simulations, it will be shown that coupling effects can be handled by including them in the optimization.

The goals of this thesis are enhancing the agility of the low-cost array, reducing the complexity of the low-cost array even more through tiling, and jointly synthesizing pattern along with polarization using the low-cost topology. Novel optimization strategies will be presented for each goal.

## 1.6. Novelties of the Thesis

To achieve the goals explained in Section 1.5, novel optimization methods and frameworks, inspired by the state of the art, are introduced:

- **Polarization State Optimization for Tri-pol Operation:** A sequential approach for the optimization of phase shifts $(p_1, \cdots, p_N)$ and beamforming weights $(w_1, \cdots, w_N)$ in the low-cost topology (Fig. 1.2b) is proposed by [8]. Suggested method by [8] gives importance to H and V polarizations; an adjustment is made to the proposed algorithm, and a trade-off among polarization states is found, increasing the performance of the desired third polarization.
- **Quantization of Polarization States**: A different quantization method, where an optimal reference phase is iteratively found, is used to quantize continuous shifts into discrete ones, which demonstrates that an improvement can be made compared to traditional methods.
- **Joint Subarray Tiling and Polarization Synthesis:** Subarray tiling of polarimetric phased arrays is not common in the literature, as it limits the capabilities of the array. To the best of the authors' knowledge, there is no implementation of subarray tiling for polarization synthesis when the low-cost topology is utilized. A novel optimization framework is devised that enables antennas in the same tile to be excited with the same amplitude but with a different phase.
- **Shaped Pattern Synthesis with Polarimetry:** As mentioned previously, shaped patterns are

also useful for PPAA applications. Polarization purity must still be satisfied when pattern shaping is performed; otherwise, the obtained measurements of precipitation particles will be biased. Common pattern shapes used in real-life radar applications are flat-top and cosecant decaying masks. It is observed that studies considering polarization synthesis along with a cosecant decaying mask jointly, do not consider the fact that cross-polarization requirements also have to change with the mask. The algorithm suggested in this thesis takes care of this by also making cross-polarization inside the shaped region decay with respect to the mask shape, maintaining the required power difference between co- and cross-polarized fields.

As can be seen, the main challenge is optimizing a large number of variables and including electromagnetic effects, like mutual coupling, within the optimization problem, which is nonlinear and nonconvex.

## 1.7. Thesis Outline

The thesis starts by explaining the signal model for phased arrays and the optimization procedure of conventional fully-polarized phased arrays. The optimization algorithm for the dual-polarized architecture, explained in Chapter 2, is a baseline for the strategies suggested in the later chapters, whose polarimetric performance will serve as a benchmark to evaluate the performance of algorithms to optimize the low-cost architecture. Afterwards, several strategies to optimize the low-cost architecture are explained in Chapter 3 and compared against the state of the art. It is shown that a trade-off among the polarization states can be obtained and exploited to enhance the performance of the low-cost architecture in the synthesis of an additional polarization state. The robustness of the suggested algorithms against mutual coupling is shown through full-wave simulations.

A trending application in active phased arrays is to decompose the array into subarrays to lower the cost. To the best of the authors' knowledge, other than utilizing polarization switches, subarraying is not implemented within the domain of polarimetric phased arrays, which is shown to even lower the cost of the low-cost architecture. After the optimization of the low-cost architecture is performed and the element polarization states are obtained in Chapter 3, subarray optimization is performed in Chapter 4. Several subarrayed architectures are discussed, and their performances are presented. It is shown that with a slight deterioration in polarimetric performance, a subarrayed architecture can be used for polarimetric arrays.

In Chapter 5, the joint pattern and polarization synthesis procedure is explained for the dual-polarized and the low-cost architectures. Different pattern shapes are tried to be synthesized with different polarizations acting as co-polarization. Although pattern synthesis is a frequently encountered problem and can be performed with different techniques, application to polarimetric arrays is not widespread. In addition to the co-polarized field, the cross-polarized field also has to be constrained with respect to the mask, to ensure the polarization purity. Through full-wave simulations, it is shown that joint pattern and polarization synthesis are indeed possible for the fully-polarized architecture, and also for the low-cost architecture with reasonable deterioration.

Finally, conclusions from the thesis and directions for future work are given in Chapter 6.

# 2

# Polarimetric Arrays with Dual-Polarized Elements

In this chapter, the theoretical background related to the examined problem will be clarified. In Section 2.1, the signal model related to antenna array theory will initially be derived for a single-polarized array and then extended to a fully polarized PPAA. Through the signal model, the objective function and the constraints of the optimization problem will be generated. In Section 2.2, the structure of the optimization problem will be explained. Convex optimization will be used to solve the optimization problems, requiring the problem to be put into a convex format.

## 2.1. Signal Model

Deriving the signal model for antenna arrays requires an understanding of electromagnetic wave propagation. The propagation of waves in space can be described by the wave equation:

$$(\nabla^2 - \frac{1}{c^2}\frac{\partial^2}{\partial t^2})s(\mathbf{r},t) = \mathbf{0} \tag{2.1}$$

where $\mathbf{r} = [x, y, z]^T$ is the position vector in space, $c$ is the speed of the wave and $\nabla$ is the Laplacian operator in the rectangular coordinate system. A well-known solution for the wave equation can be given as:

$$s(\mathbf{r},t) = e^{j(wt-\mathbf{k}\cdot\mathbf{r})}, \quad with \quad \mathbf{k} = -\frac{2\pi}{\lambda}\begin{bmatrix}\sin\vartheta\cos\phi\\ \sin\vartheta\sin\phi\\ \cos\vartheta\end{bmatrix} \tag{2.2}$$

$w$ represents the frequency of the wave in $[rad/s]$, $\mathbf{k}$ is the wavenumber vector indicating the direction of propagation, $\vartheta$ and $\phi$ are the elevation and azimuth angles. For phased arrays with multiple elements on receive, each antenna will receive an incoming signal with a time delay due to the geometry of the array. As can be seen in Fig. 2.1, the time delay between incident signals depends on the spacing between the elements. Using (2.2), the time-delayed incident signal can be written as:

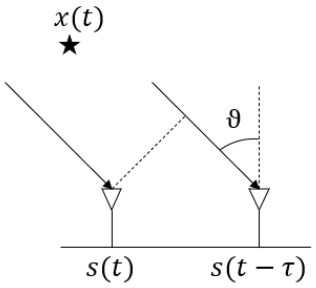


**Figure 2.1:** Geometrical delay of signal

$$s_\tau(\mathbf{r},t) = s(\mathbf{r},t-\tau) = e^{j(w(t-\tau)-\mathbf{k}\cdot\mathbf{r})} = e^{j(wt-w\tau-\mathbf{k}\cdot\mathbf{r})} \tag{2.3}$$

(2.3) shows the term generated due to the time delay, $\tau$. Through the narrow-band assumption ($|B\tau| << 2\pi$), time delays can be represented as phase shifts:

$$s_\tau(t) = s(t)e^{-jw\tau} \tag{2.4}$$

The property in (2.4) suggests that each element in an array receives the phase-shifted replica of the incoming signal, where the phase shift depends on the incidence angle $\vartheta$. For an array of $N$ elements, an $N$ by $1$ steering vector can be associated with the phase shifts between the elements:

$$\mathbf{a}(\vartheta,\phi) = \begin{bmatrix} g_1(\vartheta,\phi)e^{-jw\tau_1} & \cdots & g_N(\vartheta,\phi)e^{-jw\tau_N} \end{bmatrix}^H \tag{2.5}$$

where $g_i(\vartheta)$ represents the term arising due to the coupling effect between the antennas. The signals received or transmitted by antennas are highly affected by the individual AEPs. Each antenna in an array has a specific gain and phase pattern because of the electromagnetic interactions between the feed lines and the apertures. These field interactions can be accounted for by integrating element patterns into the optimization problem through expressing the steering vector in terms of complex element patterns and phase delays jointly.

The array response to any input can be given through the beamforming coefficients to be optimized and the steering vector given in (2.5). For a single-polarized array composed of N radiators, the far-field pattern in spherical coordinates can be given as follows:

$$F(\vartheta,\phi) = \sum_{i=1}^{N} w_n a_n(\vartheta,\phi) = \mathbf{a}^H(\vartheta,\phi)\mathbf{w} \tag{2.6}$$

where **w** is the vector containing beamforming coefficients. The previous discussion on the single-polarized array can be extended to the fully polarized array in Fig. 1.2a, where the field components (H, V) can be obtained through:

$$F_H(\vartheta,\phi) = \mathbf{a}^H_{HH}(\vartheta,\phi)\mathbf{w}_H + \mathbf{a}^H_{HV}(\vartheta,\phi)\mathbf{w}_V \tag{2.7}$$

$$F_V(\vartheta,\phi) = \mathbf{a}^H_{VV}(\vartheta,\phi)\mathbf{w}_V + \mathbf{a}^H_{VH}(\vartheta,\phi)\mathbf{w}_H \tag{2.8}$$

where the second subscript denotes the port, and the first subscript denotes the resulting field (e.g.,

$\mathbf{a}_{HH}$ represents the H field due to the H port). Due to coupling effects between the H and V ports of a dual-polarized element, cross-polarization terms ($\mathbf{a}_{HV}, \mathbf{a}_{VH}$) appear in the above field equations, deteriorating the purity of the desired polarization. Although H and V fields can be expressed through these field equations, the motivation is to synthesize an arbitrary third polarization state, which requires a similar analytical formulation. Using the Jones transformation matrix, any arbitrary polarization can be expressed through the H and V fields:

$$\begin{bmatrix} F_{co} \\ F_{cr} \end{bmatrix} = \begin{bmatrix} \cos(\varphi) & \sin(\varphi) \\ -\sin(\varphi) & \cos(\varphi) \end{bmatrix} \begin{bmatrix} 1 & 0 \\ 0 & e^{-j\eta} \end{bmatrix} \begin{bmatrix} F_H \\ F_V \end{bmatrix} \tag{2.9}$$

$$F_{co}(\vartheta, \phi) = \cos(\varphi) F_H(\vartheta, \phi) + \sin(\varphi) e^{-j\eta} F_V(\vartheta, \phi) \tag{2.10}$$

$$F_{cr}(\vartheta, \phi) = -\sin(\varphi) F_H(\vartheta, \phi) + \cos(\varphi) e^{-j\eta} F_V(\vartheta, \phi) \tag{2.11}$$

where $\varphi$ is the ellipticity angle and $\eta$ is the phase difference between the orthogonal fields. The field expressions in (2.10) and (2.11) will be used to set up the constraints and objective function of the optimization problem.

## 2.2. Convex Optimization

To optimize the complex beamforming coefficients ($\mathbf{w}_H, \mathbf{w}_V$), convex optimization is used, as it is a faster approach compared to numerical algorithms, and the problem can be put into a convex format. A standard convex optimization problem has the form [17]:

$$\begin{aligned} \text{minimize} \quad & f_0(x) \\ \text{subject to} \quad & f_i(x) \leq 0, \quad i = 1, \ldots, m \\ & h_i(x) = a_i^T x - b_i = 0, \quad i = 1, \ldots, p \end{aligned} \tag{2.12}$$

The objective function ($f_0(x)$) and all inequality constraint functions ($f_1(x) \cdots f_m(x)$) have to be convex; and equality constraints ($h_1(x) \cdots h_p(x)$) have to be affine. A function is convex if the domain of the function is a convex set and satisfies:

$$f(\theta x + (1-\theta)y) \leq \theta f(x) + (1-\theta) f(y) \tag{2.13}$$

for all x and y within the domain of the function, where $0 \leq \theta \leq 1$. For affinity, both sides of (2.13) must be equal. Another way to observe convexity is to check the Hessian of the function. The Hessian of a convex function $f$ is positive semidefinite (PSD): $\nabla^2 f(x) \succeq 0$, and the Hessian of an affine function is 0: $\nabla^2 f(x) = 0$ for all x in the domain. In Section 2.3, the problem for the dual-polarized antenna shown in Fig. 1.2a will be formulated.

## 2.3. Problem Formulation for the Dual-Polarized Architecture

The performance of the phased array employing the dual-polarized architecture will be a benchmark for the algorithm proposed in [8] and the algorithms proposed in this study. Problem formulation will initially be performed for the dual-polarized architecture, and similar formulations will be adapted to other architectures and algorithms.

The optimization problem formulation is performed on a 2D discretized u-v grid, called the $\sin\vartheta$ space. When dealing with planar antenna arrays, it is a common practice to utilize the u-v grid, where the transformation from spherical coordinates to u-v space can be performed through: $u = \sin\vartheta\cos\phi$ and $v = \sin\vartheta\sin\phi$ ($\vartheta$ represents elevation, $\phi$ represents azimuth angle). As there will be different requirements for different regions of the output beam, the strategy is to divide the u-v grid into different regions and express the constraints through the discrete points in each region (see Fig. 2.2). Fig. 2.2 illustrates the strategy on an azimuthal cut in the spherical coordinate system (transformation to u-v space is trivial). Across the discrete points in the side-lobe region, the aim is to suppress the magnitude of the co- and cross-polarized fields; and across the points in the main-lobe region, the cross-polarized field should be suppressed more for the desired polarization purity, and the co-polarized field should be maximized at the center of the region ($\| F_{co}(\vartheta_0) \|_2$). $\vartheta_0$ defines the center of main-lobe, specifying the steering angle in elevation. It is important to note that the main-lobe and side-lobe regions should not overlap, as it might result in an infeasible problem. The density of the u-v grid (the number of points) determines the precision of the optimized beamforming weights in terms of meeting the constraints; a coarse grid might fail to satisfy the constraints when tested on an actual PPAA, but a very fine grid might drastically increase the duration of the optimization because of the high number of constraints.

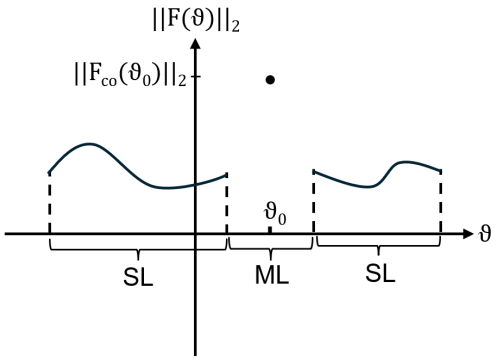


**Figure 2.2:** Dividing the angular space into two regions at a specific azimuthal cut (ML: Main-lobe, SL: Side-lobe)

The structure of the optimization problem compatible with the dual-polarized architecture can be written as:

$$
\begin{aligned}
\min_{\mathbf{w}_H,\mathbf{w}_V} \quad & -\mathbb{R}(F_{co}(\vartheta_0,\phi_0)) = -\rho \\
\text{s.t.} \quad & \mathbb{I}(F_{co}(\vartheta_0,\phi_0)) = 0 \\
& \|F_{cr}(\vartheta_i,\phi_i)\|_2 \le \rho\cdot 10^{\frac{XPL}{20}}, \quad \forall(\vartheta_i,\phi_i)\in ML \\
& \|F_{cr}(\vartheta_i,\phi_i)\|_2 \le \rho\cdot 10^{\frac{SLL_{cr}}{20}}, \quad \forall(\vartheta_i,\phi_i)\in SL \\
& \|F_{co}(\vartheta_i,\phi_i)\|_2 \le \rho\cdot 10^{\frac{SLL_{co}}{20}}, \quad \forall(\vartheta_i,\phi_i)\in SL \\
& \|\mathbf{w}_{H,n}\|_2 \le 1, \quad \forall n = 1,\cdots,N \\
& \|\mathbf{w}_{V,n}\|_2 \le 1, \quad \forall n = 1,\cdots,N
\end{aligned}
\tag{2.14}
$$

As the dual-polarized architecture does not impose any limitations on the ports, optimization can be carried out separately over the beamforming weights ($\mathbf{w}_H, \mathbf{w}_V$) corresponding to separate ports. The analytical expressions for the co- and cross-polarized fields in (2.14) can be found in (2.10), (2.11). It is easy to see that the format of the optimization problem given in (2.14) has the format of a standard convex optimization problem in (2.12). The objective of optimization is to maximize the gain in the direction of radiation (defined by $(\vartheta_0,\phi_0)$) for a given polarization state $(\varphi,\eta)$. However, the $l2$-norm of gain in

the radiation direction cannot be used in the objective, as it has the form: $\| F_{co}(\vartheta_0, \phi_0) \|_2 = \| \mathbf{a}^H \mathbf{w} \|_2 = \mathbf{w}^H \mathbf{a}\mathbf{a}^H \mathbf{w} = \mathbf{w}^H \mathbf{A} \mathbf{w}$, where the Hessian is $\nabla^2 F_{co}(\mathbf{w}) = A \succeq 0$. As $\mathbf{A}$ is PSD, $\| F_{co}(\vartheta_0, \phi_0) \|_2$ is a convex function and can be minimized; however, this will minimize the gain. Subsequently, $- \| F_{co}(\vartheta_0, \phi_0) \|_2$ is concave and can be maximized; however, this, in turn, will minimize the gain. Therefore, as detailed in [18], $\mathbb{R}(F_{co}(\vartheta_0, \phi_0))$ can be used instead of $\| F_{co}(\vartheta_0, \phi_0) \|_2$, with only the phase of the gain being different in the radiation direction (as the suggested strategy will result in a phaseless gain).

Throughout the literature search, it is observed that expressing the problem in the form of minimization is a common practice, which requires the objective function to be convex. In the examined case, $\mathbb{R}(F_{co}(\vartheta_0, \phi_0))$ is a linear function of $\mathbf{w}_H$ and $\mathbf{w}_V$ (can be seen from (2.10) and (2.11)); any linear function is convex and concave, as the strict equality condition in (2.13) holds. Moreover, maximizing a concave function $f(x)$ is equivalent to minimizing the negative of that function $g(x) = -f(x)$, as $g(x)$ is convex. Therefore, negative of $\mathbb{R}(F_{co}(\vartheta_0, \phi_0))$ is minimized instead of maximizing $\mathbb{R}(F_{co}(\vartheta_0, \phi_0))$, as they are equivalent. It must be noted that $-F_{co}(\vartheta_0, \phi_0)$ is a complex number with phase and simply the real part of it is minimized instead of the $l2$-norm magnitude. For the real part of $F_{co}(\vartheta_0, \phi_0)$ to imitate the $l2$-norm, the imaginary part ($\mathbb{I}(F_{co}(\vartheta_0, \phi_0))$) must be enforced to be zero, which is the first constraint of the optimization problem. As mentioned in Section 2.2, an equality constraint has to be affine (has to be in the form of $h_i(x)$ in (2.12)) in an optimization problem. $\mathbb{I}(F_{co}(\vartheta_0, \phi_0))$ is a linear function and the Hessian of it is equal to 0, hence it is an affine function.

The second constraint in (2.14) suppresses the cross-polarized field inside the main lobe. XPL is a user-defined value that indicates by how many dB the level of cross-polarization should be lower than that of the co-polarized field. To ensure the convexity of this constraint, a norm cone can be associated to it. For any norm, a norm cone $\mathbb{C}$ has the structure [17]:

$$\mathbb{C} = \{(x, t) \quad | \quad \| x \| \leq t\} \subseteq \mathbf{R}^{n+1} \tag{2.15}$$

Any set having the form of the norm cone described in (2.15) is a convex set. As the cross-polarized field described in the constraint is a complex number, its magnitude can be obtained through the $l2$-norm: $\| F_{cr,i} \|_2 = \sqrt{\mathbb{R}(F_{cr,i})^2 + \mathbb{I}(F_{cr,i})^2}$. Using the $l2$-norm, a second order cone (SOC) can be associated with each of the discrete points in the main-lobe region corresponding to the cross-polarized field and tried to be suppressed:

$$\mathbb{K} = \{(\mathbb{R}(F_{cr}(\vartheta_i, \phi_i)), \mathbb{I}(F_{cr}(\vartheta_i, \phi_i)), \rho \cdot 10^{\frac{XPL}{20}}) \quad | \quad \| F_{cr}(\vartheta_i, \phi_i) \|_2 \leq \rho \cdot 10^{\frac{XPL}{20}}\} \subseteq \mathbf{R}^3 \tag{2.16}$$

where $\mathbb{K}$ is a second-order cone in $\mathbf{R}^3$. Similar cones can be associated with the second and third sets of inequality constraints in (2.14), where the purpose is to suppress the co- and cross-polarized field in the side-lobe region. $\text{SLL}_{cr}$ and $\text{SLL}_{co}$ are user-defined values that indicate by how many dB the level of co- and cross-polarization in the side-lobe region should be lower than the gain of the co-polarized field in the direction of radiation.

The remaining two sets of inequality constraints are used to suppress the magnitude of the beamforming coefficients for both ports. In a real phased array, the maximum excitation magnitude is determined by the maximum power that can be supplied to each port, which is dictated by the hardware. In this work, the maximum amplitude that can be supplied to any of the ports is assumed to be 1. Similarly, a second-order cone can be associated with these constraints:

$$\mathbb{U} = \{(\mathbb{R}(\mathbf{w}_{H,n}), \mathbb{I}(\mathbf{w}_{H,n}), 1) \quad | \quad \| \mathbf{w}_{H,n} \|_2 \leq 1\} \subseteq \mathbf{R}^3 \tag{2.17}$$

The same second-order cone can also be associated with the V port weights as well. All inequality constraints in (2.14) are in the form of a second-order cone and therefore convex, and the inequality constraint is shown to be affine. Such an optimization problem falls under quadratic optimization problems, specifically the second-order cone program, because of the structure of the inequality constraints. As the overall optimization problem is convex, existing libraries [19] can be used to solve it for complex beamforming coefficients.

## 2.4. Performance of the Dual-Polarized Architecture

Throughout the optimizations, the simulation settings and simplifications of [8] are used. The coupling effects between the ports are neglected ($\mathbf{a}_{HV} = \mathbf{a}_{VH} = \mathbf{0}$), and the ports are assumed to radiate isotropically. A 16 by 16 array where the elements are located half wavelength apart from each other in the two axes is chosen for the simulations [8]. The chosen polarization states are: H ($\varphi = 0°, \eta = 0°$), V ($\varphi = 90°, \eta = 0°$), and LHCP ($\varphi = 45°, \eta = 90°$) as the arbitrary third polarization. A discretized u-v grid is used with a regular step size of 0.05 during optimization to relax computational complexity. Constraints are set as: XPL$= -45$ dB, SLL$_{cr}$=SLL$_{co} = -20$ dB [8], and two different scenarios are considered: broadside radiation and steering to $45°$ in both elevation ($\vartheta$) and azimuthal ($\phi$) planes, which is $u_s = v_s = 0.5$. The co-polarized directivity values are computed numerically by taking the ratio of radiation intensity (U) in the scan direction to the average radiated power:

$$D_0 = \frac{U(\vartheta_0, \phi_0)}{U_0} = \frac{4\pi U(\vartheta_0, \phi_0)}{\int_0^{2\pi} \int_0^{\pi} U(\vartheta, \phi) \sin\vartheta d\vartheta d\phi} \tag{2.18}$$

As mentioned in Section 2.3, the maximum allowed magnitude for each port is $1$. The power allowed at each port can be found by squaring the amplitude and dividing it by two. As the maximum allowed magnitude is $1$, the maximum allowed power per port is $0.5$ W and per antenna is $1$ W. However, for the synthesis of H and V, the dual-polarized architecture does not excite the port that synthesizes the opposite polarization (due to the ideality assumptions). Therefore, for a fair comparison with the upcoming low-cost algorithms, the power levels obtained for H and V will be doubled. Another important performance metric is the Effective Isotropic Radiated Power (EIRP), which shows the measured radiated power in a single direction. As the antenna is assumed to be lossless and perfectly matched at all scan angles for the examined case, EIRP can be obtained through: $EIRP = Directivity \cdot P_{in}$.

**Table 2.1:** Polarimetric performance of the dual-polarized architecture

| **Direction** | $(\varphi, \eta)$ | **Directivity** [dBi] | **Pin** [W] | **EIRP**[dBW] | **SLL**$_{co}$[dB] |
|---|---|---|---|---|---|
| **Broadside**$(u_s = v_s = 0)$ | (0,0) | 25.25 | 203.42 | 48.33 | -18.62 |
| | (90,0) | 25.25 | 203.34 | 48.34 | -18.65 |
| | (45,90) | 25.20 | 205.32 | 48.33 | -18.60 |
| **Steered**$(u_s = v_s = 0.5)$ | (0,0) | 23.75 | 239.11 | 47.53 | -17.73 |
| | (90,0) | 23.75 | 239.09 | 47.53 | -17.74 |
| | (45,90) | 23.74 | 239.00 | 47.52 | -17.74 |

The polarimetric performance of the conventional dual-polarized architecture is shown in Table 2.1. Convex optimization is utilized to derive the results. The absolute values of the directivities are shown, while SLL$_{co}$ is normalized with respect to the maximum gain, which is aimed to be less than $-20$ dB. XPL and SLL$_{Cr}$ are not given, as the algorithm does not excite the port synthesizing cross-polarization for a predefined co-polarization. It should be noted that the constraints in (2.14) are not fully met even with the conventional architecture due to the u-v grid discretization. Improving the grid resolution will

improve the SLL results, but this will significantly increase the computational burden. Moreover, Fig. 2.3 shows the u-v plots of the co-polarized components of the three examined polarization states for different radiation directions. It can be seen that the conventional dual-polarized architecture can easily synthesize any desired polarization, steer the main-lobe, and suppress the side-lobes.

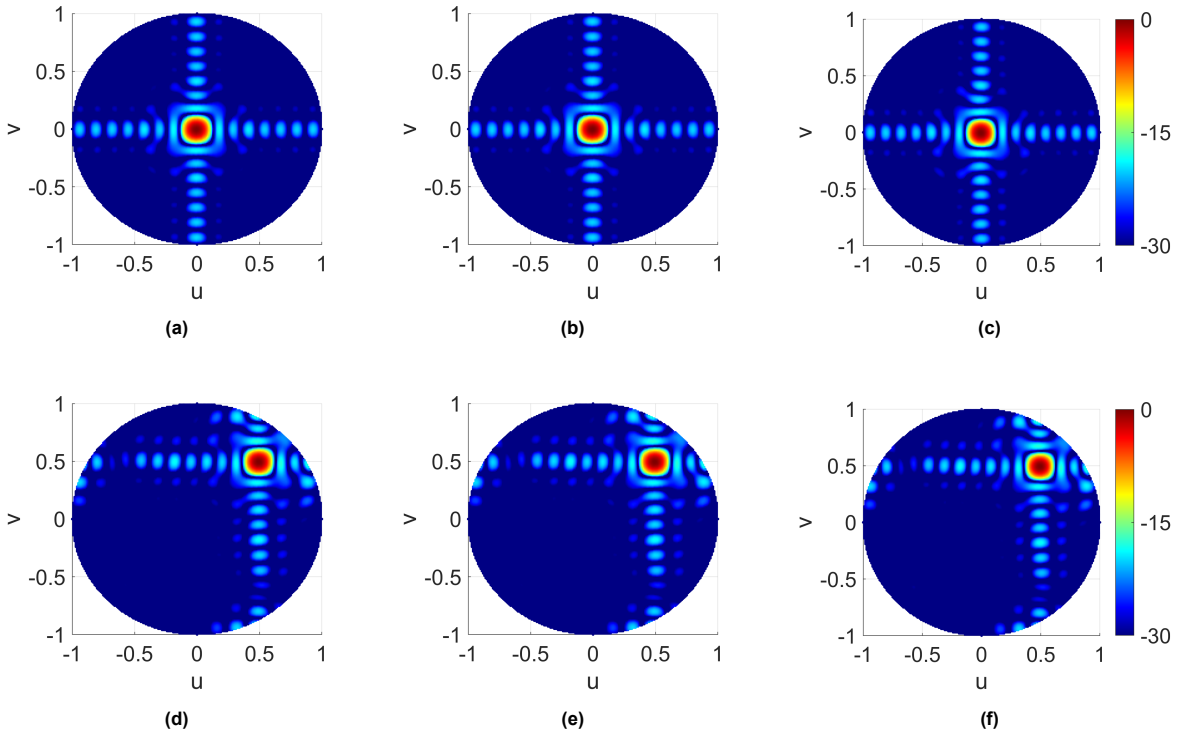


**Figure 2.3:** Co-polarized radiation patterns in the $uv$-plane (normalized, in dB) with the conventional dual-polarized architecture for a broadside [$u_s = v_s = 0$] and a steered [$u_s = v_s = 0.5$] beam: (a) ($\varphi = 0°, \eta = 0°$) - broadside, (b) ($\varphi = 90°, \eta = 0°$) - broadside., (c) ($\varphi = 45°, \eta = 90°$) - broadside, (d) ($\varphi = 0°, \eta = 0°$) - steered, (e) ($\varphi = 90°, \eta = 0°$) - steered, (f) ($\varphi = 45°, \eta = 90°$) - steered

## 2.5. Full Wave Simulations

To examine the robustness of the algorithm against coupling effects between elements, a 13 by 13 (not 16 by 16 due to computational burden) planar antenna array is designed in the CST Studio Suite, where the elements are located half a wavelength apart from each other (at $15.5$ GHz). The array consists of dual-polarized stacked patch antenna elements (see Fig. 2.4a) with two feeds per element, where both feeds are matched to $50\Omega$ with $S_{11} = S_{22} \leq -12$ dB between $15.05 - 15.95$ GHz (see Fig. 2.5). The entire array is simulated with sequential excitation in the time domain to obtain the active element patterns from each feed port at the center frequency of $15.5$ GHz. The variation of AEPs due to the coupling effect is shown in Fig. 2.6 for a center, edge, and corner element. Active element patterns are obtained with a resolution of $5°$ in elevation and azimuth, resulting in 441 points on the u-v grid for optimization.

The optimization is performed using the simulation settings of [8]: XPL$= -45$ dB, SLL$_{co}$ =SLL$_{cr} = -20$ dB. The polarimetric performance of the planar array is shown in Table 2.2. Unlike in the previous section, the optimization grid and the simulation grid (the grid used to obtain the performance metrics in Table 2.2) are the same. As arbitrary precision levels cannot be selected from CST, the only finer grid size was $1°$, resulting in more than 10500 data points, which was not feasible for optimization and resulted in significant deterioration in SLL levels when used only as the simulation grid. As the

optimization and simulation grids are the same, it can be seen from Table 2.2 that all XPL and SLL constraints are perfectly met for any polarization and radiation direction. Table 2.2 will serve as a benchmark for the comparison of the algorithms in Chapter 3. It should be noted that the maximum amplitude is normalized with respect to one, and the power stimulated to a port is calculated by squaring the amplitude and dividing the result by two. Therefore, the maximum power that can be supplied to the array is $169$ W.

**Table 2.2:** Polarimetric performance of the designed fully-polarized planar array

| **Direction** | $(\varphi, \eta)$ | **Gain** [dBi] | **Pin**[W] | **EIRP**[dBW] | **XPL**[dB] | **SLL**$_{co}$[dB] | **SLL**$_{cr}$[dB] |
|---|---|---|---|---|---|---|---|
| **Broadside** $(u_s = v_s = 0)$ | (0,0) | 24.49 | 168.89 | 46.77 | -45.00 | -20.00 | -20.36 |
| | (90,0) | 24.45 | 167.78 | 46.70 | -45.00 | -20.00 | -20.00 |
| | (45,90) | 27.08 | 169.00 | 49.36 | -45.00 | -20.00 | -29.38 |
| **Steered** $(u_s = v_s = 0.5)$ | (0,0) | 23.25 | 166.70 | 45.47 | -45.00 | -20.00 | -20.00 |
| | (90,0) | 23.27 | 167.10 | 45.50 | -45.00 | -20.00 | -20.00 |
| | (45,90) | 25.27 | 168.29 | 46.52 | -45.00 | -20.00 | -20.69 |

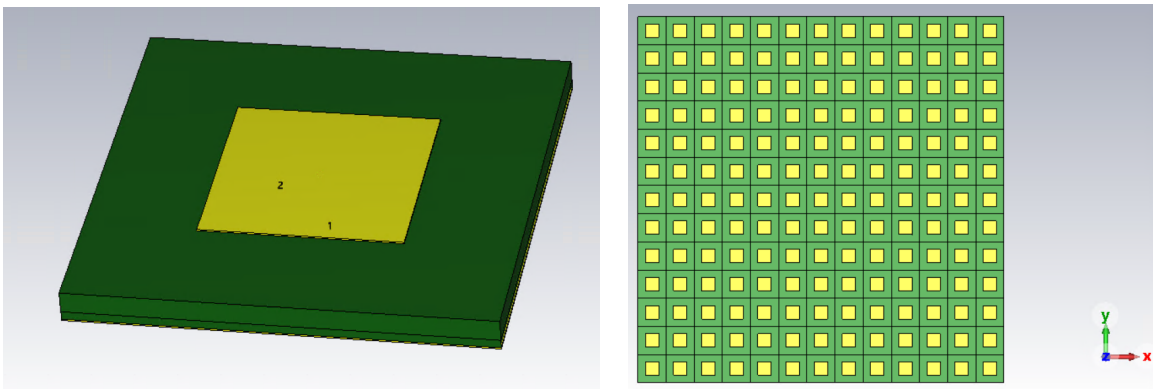


**(a)** Wideband stacked patch antenna **(b)** 13 by 13 planar array

**Figure 2.4:** Antenna design in CST Studio Suite

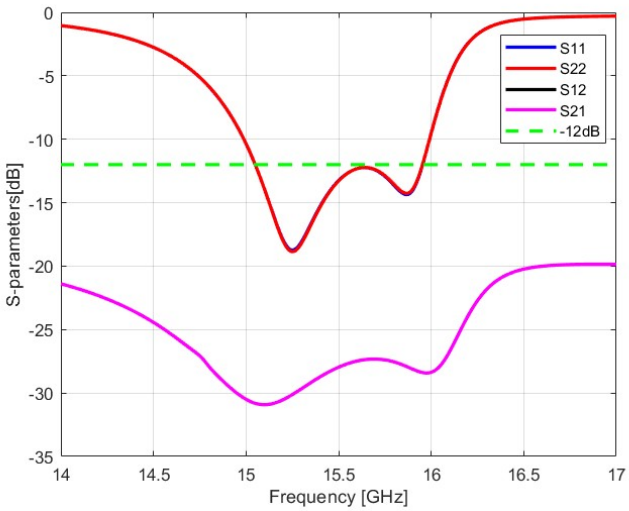


**Figure 2.5:** S-parameters of a single element, simulated with unit-cell boundaries in boresight

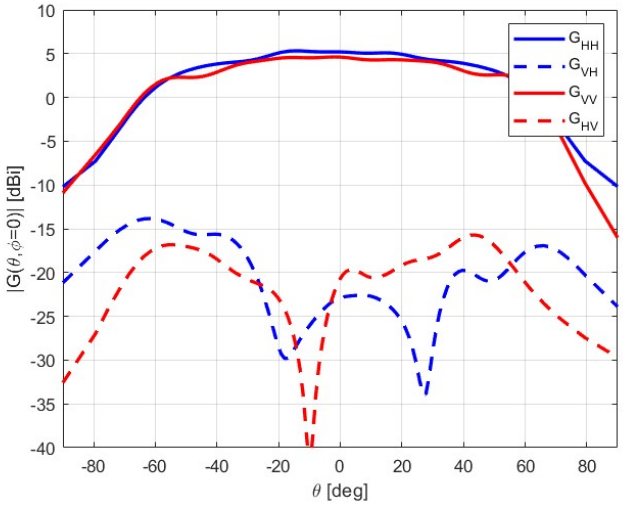


**(a)** Center element AEP

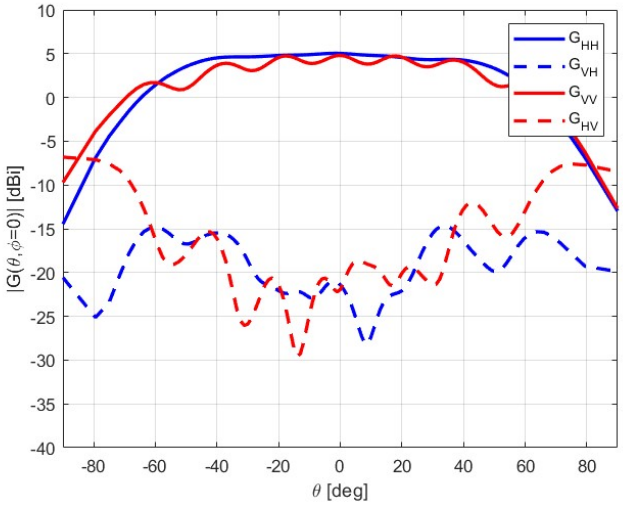


**(b)** Edge element AEP

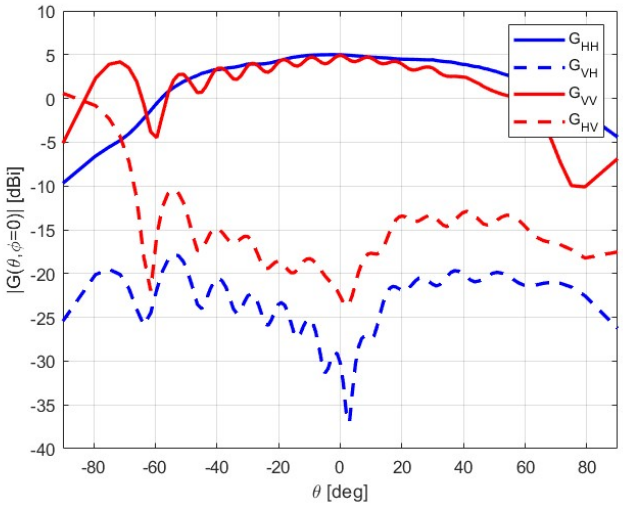


**(c)** Corner element AEP

**Figure 2.6:** Active element patterns obtained with full-wave simulations from the designed array

## 2.6. Intermediate Conclusions

In this chapter, the signal model required to express fields is derived. Derivations are first performed for a single-polarized array and then extended to a fully-polarized array. Afterwards, it is shown that for the conventional fully-polarized PPAA, problem can be put into convex format and solved efficiently. Simulations are initially performed by neglecting coupling effects and assuming isotropic radiation. Finally, the convex algorithm is performed on a planar array designed in CST Studio Suite, and supported with full-wave simulations. It is shown that coupling effects can be included in optimization process, and beamforming coefficients can be optimized respectively by considering the electromagnetic effects. Moreover, it has also been demonstrated that the dual-polarized architecture can synthesize any polarization with excellent performance.

# 3

# Element Polarization Optimization for the Low-Cost Topology

The conventional fully-polarized array can perfectly synthesize any desired polarization. However, the intention is to create a PPAA using the architecture in Fig. 1.2b, where the excitations of the ports of the same patch differ solely by a phase. The phase difference between the ports of an element determines the polarization state of the element. In addition to excitation amplitudes being constant across the ports, another limiting factor is that the phase difference between the ports will be fixed after being optimized; which means that the analog part of the array will not be reconfigurable. As will be shown, low-cost architecture will limit the gain and EIRP of the array for each polarization: however, through the optimization of element polarization states ($\mathbf{p} = [p_1 \cdots p_N]$ in Fig. 1.2b), this loss can be minimized. Section 3.1 discusses the algorithm suggested in [8], where the optimization is performed for H and V, and presents the simulation results. Section 3.2 discusses the suggested optimization algorithms for the improved synthesis of 3 polarizations. Moreover, a novel quantization algorithm is also presented for the discretization of the optimized continuous phase shifts.

## 3.1. Benchmark Techniques

In this section, the algorithm proposed in [8] for the optimization of beamforming weights $(w_{H,1} \cdots w_{H,N})$ and phase shifts between the ports ($\mathbf{p}$) will be explained and compared with the dual-polarized architecture. As the low-cost architecture is different than the dual-polarized architecture, (2.7) and (2.8) need to be adjusted. Field equations for H/V polarization basis can be written as:

$$F_H(\vartheta, \phi) = \mathbf{a}_{HH}^H(\vartheta, \phi)\mathbf{w}_H + \mathbf{a}_{HV}^H(\vartheta, \phi)(\mathbf{w}_H \odot \mathbf{p}) \tag{3.1}$$

$$F_V(\vartheta, \phi) = \mathbf{a}_{VV}^H(\vartheta, \phi)(\mathbf{w}_H \odot \mathbf{p}) + \mathbf{a}_{VH}^H(\vartheta, \phi)\mathbf{w}_H \tag{3.2}$$

where $\odot$ is the Hadamard product and represents entry-wise product of the vectors. As before, coupling effects between the ports are neglected, and isotropic radiation is assumed:

$$F_H(\vartheta, \phi) = \mathbf{a}_{HH}^H(\vartheta, \phi)\mathbf{w}_H = \mathbf{a}^H(\vartheta, \phi)\mathbf{w}_H \tag{3.3}$$

$$F_V(\vartheta,\phi) = \mathbf{a}_{VV}^H(\vartheta,\phi)(\mathbf{w}_H \odot \mathbf{p}) = \mathbf{a}^H(\vartheta,\phi)(\mathbf{w}_H \odot \mathbf{p}) \tag{3.4}$$

The optimization problem in (2.14) can be adjusted according to the low-cost topology and field equations (3.3), (3.4):

$$\begin{aligned}
\min_{\mathbf{w}_H,\mathbf{p}} \quad & -\mathbb{R}(F_{co}(\vartheta_0,\phi_0)) = -\rho \\
\text{s.t.} \quad & \mathbb{I}(F_{co}(\vartheta_0,\phi_0)) = 0 \\
& \|F_{cr}(\vartheta_i,\phi_i)\|_2 \leq \rho \cdot 10^{\frac{XPL}{20}}, \quad \forall(\vartheta_i,\phi_i) \in ML \\
& \|F_{cr}(\vartheta_i,\phi_i)\|_2 \leq \rho \cdot 10^{\frac{SLL_{cr}}{20}}, \quad \forall(\vartheta_i,\phi_i) \in SL \\
& \|F_{co}(\vartheta_i,\phi_i)\|_2 \leq \rho \cdot 10^{\frac{SLL_{co}}{20}}, \quad \forall(\vartheta_i,\phi_i) \in SL \\
& \|\mathbf{p}_n\|_2 = 1, \quad \forall n = 1,\cdots,N \\
& \|\mathbf{w}_{H,n}\|_2 \leq 1, \quad \forall n = 1,\cdots,N
\end{aligned} \tag{3.5}$$

With the low-cost topology, optimization will be performed under $\mathbf{w}_H$ and $\mathbf{p}$. As $\mathbf{p}$ is solely a phase shifter, it has the form of a complex exponential: $\|p_i\|_2 = \|e^{j\alpha_i}\|_2 = \sqrt{\mathbb{R}(p_i)^2 + \mathbb{I}(p_i)^2} = 1$, and therefore the magnitude of it is constrained to be equal to 1 in (3.5). However, it can be proven that this constraint does not define a convex set, and so an affine set. For a convex set $\mathbf{C}$, any line segment passing through any two points in $\mathbf{C}$ must also be in the set [17]: $\theta x_1 + (1-\theta)x_2 \in \mathbf{C}$, where $0 \leq \theta \leq 1$ and $x_1, x_2 \in \mathbf{C}$. Let $x_1 = 1$, $x_2 = j$, and $\theta = 0.5$, where both $\|x_1\|_2 = \|x_2\|_2 = 1$ and hence in the set $\mathbf{C}$:

$$x_3 = \theta x_1 + (1-\theta)x_2 = \frac{1}{2} + \frac{1}{2}j$$

$$\|x_3\|_2 = \|\frac{1}{2} + \frac{1}{2}j\|_2 = 0.707 \neq 1$$

It can be seen that $x_3$, which lies between $x_1, x_2$, is not in the set $\mathbf{C}$, making it nonconvex and restricting affinity. Although in the upcoming chapters it will be shown that the problem can be put into a convex format through semidefinite relaxation and joint optimization of the variables is possible, a sequential approach is preferred in [8], where $\mathbf{p}$ and $\mathbf{w}_H$ are optimized separately. Initially, H port weights are assumed to be uniformly excited, $\mathbf{w}_H = \mathbf{1}$, and the $\mathbf{p}$ that would result in the least power of cross-polarization is tried to be obtained. As the purpose is to synthesize H and V with a polarimetric performance as close as possible to the dual-polarized architecture, the optimization of $\mathbf{p}$ is performed with respect to H. However, it should be noted that optimization of $\mathbf{p}$ with respect to H will not deteriorate the performance of the array when synthesizing V, since $\mathbf{w}_H$ can be optimized such that it multiplies the ports with the conjugate of $\mathbf{p}$, making $\mathbf{w}_V = \mathbf{w}_H \odot \mathbf{p} = \mathbf{p}^* \odot \mathbf{p} = \mathbf{1}$. When $\mathbf{w}_H = \mathbf{1}$, field expressions in (3.3), (3.4) become:

$$F_H(\vartheta,\phi) = \mathbf{a}^H(\vartheta,\phi)\mathbf{w}_H = \mathbf{a}^H(\vartheta,\phi)\mathbf{1} = \sum_{i=1}^{N} a_i(\vartheta,\phi) \tag{3.6}$$

$$F_V(\vartheta,\phi) = \mathbf{a}^H(\vartheta,\phi)(\mathbf{w}_H \odot \mathbf{p}) = \mathbf{a}^H(\vartheta,\phi)\mathbf{p} = \sum_{i=1}^{N} a_i(\vartheta,\phi)p_i \tag{3.7}$$

where $F_V(\vartheta,\phi)$ is the expression of the cross-polarization with respect to H. Moreover, for the broadside radiation case, there is no delay between the elements of a planar array, $\mathbf{a}^H(0,0) = \mathbf{1}$ (noting the isotropic radiation assumption), which makes the cross-polarization on the broadside simply equal

to the sum of phase shifts: $F_V(0,0) = \sum_{i=1}^{N} p_i$. Therefore, cross-polarization on the broadside can theoretically be set to zero by simply constraining the sum of the fixed phase shifts to be equal to zero. As equating the sum of complex exponentials is not a linear constraint, half of $\mathbf{p}$ is optimized: $\mathbf{q} = [q_1 \cdots q_{N/2}]$ and the remaining half is simply set to the negative of $\mathbf{q}$. The indices of the elements to be optimized and to be negated are chosen prior to optimization with a random selection-based algorithm, as explained in [8]. The minimization problem for this stage can be written as:

$$\begin{aligned} \min_{\mathbf{q}} \quad & \epsilon \\ \text{s.t.} \quad & \|F_V(\vartheta_i, \phi_i)\|_\infty \leq \epsilon, \quad \forall(\vartheta_i, \phi_i) \\ & \|\mathbf{q}_n\|_2 = 1, \quad \forall n = 1, \cdots, N/2 \end{aligned} \tag{3.8}$$

As explained previously, $\|\mathbf{q}_n\|_2 = 1$ does not define an affine set, making the problem non-convex. To solve this, the built-in *fmincon* function of Matlab is used [8], which is an iterative algorithm that can solve non-linear optimization problems with constraints. Once $\mathbf{q}$ is obtained through (3.8), $\mathbf{p}$ can be regenerated using the initially obtained index vectors. The next step is to quantize the continuous phases into discrete levels; a minimum distance function is utilized in [8] for quantization:

$$f_d(x, y) = \sqrt{(\cos x - \cos y)^2 + (\sin x - \sin y)^2} \tag{3.9}$$

where $x$ represents the continuous phase shifts and $y$ represents the quantization levels. Quantization is performed assuming two bits are available for the phase shifter and hence four quantization levels: $[-90°, 0°, 90°, 180°]$.

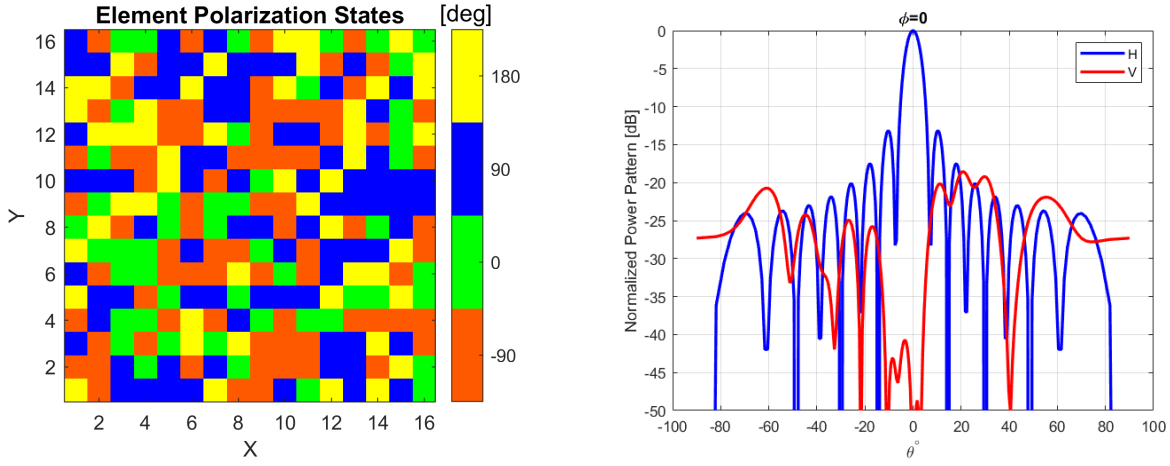


**(a)** Element polarization states

**(b)** Obtained co-pol: H and cross-pol: V levels, $\phi = 0$ plane

**Figure 3.1:** Optimization of polarization states using [8]

Fig. 3.1a shows the optimized and quantized phase shifts, and Fig. 3.1b shows the corresponding H and V fields. It can be seen that V is suppressed by approximately $20$ dB in the side-lobe region, and diverges to $-\infty$ on the broadside as the sum of the elements of $\mathbf{p}$ is constrained to be zero. Once $\mathbf{p}$ is obtained, it will be fixed and $\mathbf{w}_H$ can be optimized for the synthesis of any desired polarization. The

convex optimization problem for this case can be written as:

$$\begin{aligned}
\min_{\mathbf{w}_H} \quad & -\mathbb{R}(F_{co}(\vartheta_0,\phi_0)) = -\rho \\
\text{s.t.} \quad & \mathbb{I}(F_{co}(\vartheta_0,\phi_0)) = 0 \\
& \|F_{cr}(\vartheta_i,\phi_i)\|_2 \leq \rho \cdot 10^{\frac{XPL}{20}}, \quad \forall(\vartheta_i,\phi_i) \in ML \\
& \|F_{cr}(\vartheta_i,\phi_i)\|_2 \leq \rho \cdot 10^{\frac{SLL_{cr}}{20}}, \quad \forall(\vartheta_i,\phi_i) \in SL \\
& \|F_{co}(\vartheta_i,\phi_i)\|_2 \leq \rho \cdot 10^{\frac{SLL_{co}}{20}}, \quad \forall(\vartheta_i,\phi_i) \in SL \\
& \|\mathbf{w}_{H,n}\|_2 \leq 1, \quad \forall n = 1,\cdots,N
\end{aligned} \tag{3.10}$$

The field equations (3.3) and (3.4) can be used together with the desired polarization state $(\phi,\eta)$ to generate $F_{co}(\vartheta,\phi)$ and $F_{cr}(\vartheta,\phi)$ in (3.10). Similarly to the dual-polarized problem in (2.14), (3.10) is a convex problem and existing libraries [19] are used to solve it.

**Table 3.1:** Polarimetric performance of the low-cost architecture with the element polarization optimization technique used in [8]

| **Direction** | $(\varphi,\eta)$ | **Directivity** [dBi] | **Pin** [W] | **EIRP** [dBW] | **XPL** [dB] | **SLL**$_{co}$ [dB] | **SLL**$_{cr}$[dB] |
|---|---|---|---|---|---|---|---|
| **Broadside** $(u_s = v_s = 0)$ | (0,0) | 20.80 | 232.03 | 44.45 | -43.14 | -18.16 | -17.27 |
| | (90,0) | 20.80 | 232.03 | 44.45 | -43.14 | -18.16 | -17.27 |
| | (45,90) | 20.13 | 153.16 | 41.99 | -45.18 | -18.18 | -18.88 |
| **Steered** $(u_s = v_s = 0.5)$ | (0,0) | 20.21 | 235.41 | 43.93 | -42.16 | -18.15 | -18.48 |
| | (90,0) | 20.16 | 236.13 | 43.89 | -43.02 | -18.19 | -16.09 |
| | (45,90) | 19.38 | 181.10 | 41.96 | -42.58 | -14.95 | -17.67 |

Table 3.1 shows the polarimetric performance of the low-cost architecture optimized with the algorithm suggested in [8]. When the polarimetric performance presented in Table 3.1 is compared to the performance of the dual-polarized architecture (Table 2.1), it can be seen that the loss in directivity for the synthesis of LHCP can be greater than $5$ dB. Moreover, the loss in EIRP for H and V (on the broadside) is around $4$ dB and $6.3$ dB for LHCP, which clearly motivates this work on 3-pol synthesis with the same low-cost architecture.

## 3.2. 3-Pol Optimization

Section 3.1 motivated the need for a new strategy to improve the polarimetric performance of the LHCP synthesis of the array without deteriorating the H and V performance considerably. In this section, two new strategies for the optimization of **p** will be presented: Section 3.2.1 will discuss Polarization Averaging (PA), and Section 3.2.2 will discuss Common Polarization Suppression (CPS). In addition to the two algorithms, a new quantization technique named Lloyd-Max Quantization, differing from the method used in [8], will be introduced in Section 3.2.3. Associated performance results for PA and CPS, quantized with both methods, will be given in Section 3.2.4.

The flowchart for the overall synthesis procedure can be seen in Fig. 3.2. The initial step is to set the array size and geometry, and pick the desired polarizations that the array is intended to work for. The optimization of the element polarization states will be performed jointly with respect to these chosen polarization states. As the problem is explained to be non-convex, *fmincon* will be used to optimize **p**. After obtaining **p**, it will be quantized with two different methods: the regular quantization method explained in Section 3.1 and the Lloyd-Max method. The last stage is simply digital beamforming through the optimization of $\mathbf{w}_H$. $\mathbf{w}_H$ will be optimized separately for different polarizations and radiation directions.

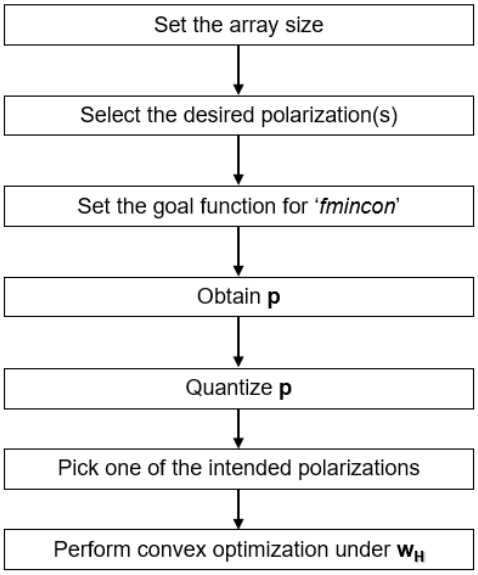


**Figure 3.2:** Flowchart of the overall polarimetric array synthesis procedure

### 3.2.1. Polarization Averaging (PA)

The strategy in PA is to consider the cross-polarization requirements of several polarizations together in the optimization function. As before, H-ports are assumed to be uniformly excited, $\mathbf{w}_H = \mathbf{1}$, and $\mathbf{p}$ is optimized. The architecture is intended to achieve good performance for three different polarization states where two of them are H/V, and the remaining one is a linear combination of the two. It was shown that when $\mathbf{p}$ is optimized with respect to one of H/V, the remaining polarization (out of H and V) can be easily synthesized by properly optimizing $\mathbf{w}_H$ in the second stage. Therefore, the constraints of this stage are based on the cross-polarization levels of one of the H/V and the third polarization:

$$\begin{aligned} \min_{\mathbf{p}} \quad & \epsilon \\ \text{s.t.} \quad & \|\kappa F_{cr,1}(\vartheta_i,\phi_i),(1-\kappa)F_{cr,2}(\vartheta_i,\phi_i)\|_\infty \leq \epsilon, \quad \forall(\vartheta_i,\phi_i) \\ & \|\mathbf{p}_n\|_2 = 1, \quad \forall n = 1,\cdots,N \\ & 0 \leq \kappa \leq 1 \end{aligned} \tag{3.11}$$

where $F_{cr,1}$ denotes the cross-polarized field with respect to one of H and V, and $F_{cr,2}$ denotes the cross-polarized field with respect to the third polarization: LHCP. Unlike [8], the complete $\mathbf{p}$ is optimized; therefore, the sum of the elements of $\mathbf{p}$ is not necessarily zero, and correspondingly the cross-polarization of H on the broadside. It is found that enforcing the constraint $\sum_{i=1}^{N} p_i = 0$ significantly narrows down the solution set, deteriorating the polarimetric performance of the LHCP synthesis. A slack variable $\kappa$ is introduced into the optimization to give importance to any desired polarization. By varying $\kappa$, cross-polarization levels can be manipulated. Through manual tuning $\epsilon$ is taken to be 0.6 as it results in a higher H/V gain without a significant loss in LHCP.

### 3.2.2. Common Polarization Suppression (CPS)

The CPS method optimizes $\mathbf{p}$ only with respect to a single polarization state. The cross-polarization level of a single polarization state is suppressed over the angular range. The chosen polarization state will act as a common basis for the H, V, and LHCP, describing the name of the method. Since it is

known that V can be synthesized with the same performance as H through the optimization of $\mathbf{w}_H$, the common polarization state is chosen with respect to H and LHCP. As before, H-ports are assumed to be uniformly excited:

$$\begin{aligned} \min_{\mathbf{p}} \quad & \epsilon \\ \text{s.t.} \quad & \|F_{cr,mid}(\vartheta_i, \phi_i)\|_\infty \leq \epsilon, \quad \forall(\vartheta_i, \phi_i) \\ & \|\mathbf{p}_n\|_2 = 1, \quad \forall n = 1, \cdots, N \end{aligned} \tag{3.12}$$

where $F_{cr,mid}$ denotes the cross-polarization of a state that is in-between the two reference cross-polarizations. The number of constraints in (3.12) is half the number of constraints in (3.11), resulting in a wider solution set for the optimization problem. Through direct search, the common polarization state for H and LHCP is found to be $(\varphi = 27, \eta = 90)$, which is an elliptical state.

### 3.2.3. Lloyd-Max Quantization

Once the continuous phase shifts are obtained through PA and CPS, they have to be quantized into discrete levels. Along with the method in [8], the Lloyd-Max technique is used for quantization, which is an iterative algorithm searching for the best possible set of discrete phases. Although the algorithm naturally results in nonuniform discrete levels (unequal differences between levels), for a fair comparison with [8], levels are constrained to be 90° apart (assuming 2 bits are available at the phase shifter) from each other. The flowchart for the quantization procedure can be found in Fig. 3.3.

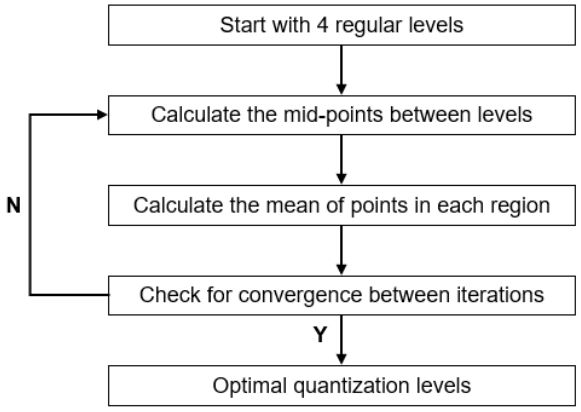


**Figure 3.3:** Flowchart of the Lloyd-Max quantization procedure

The algorithm starts with four uniform levels: $[-90°, 0°, 90°, 180°]$. The middle points, which define the border of each region, are calculated, and the continuous phases are distributed into the corresponding regions. In the next step, the mean of the points inside the same region is calculated. The calculated means are the quantization levels of that iteration. Afterward, new middle points can be calculated with the newly computed quantization levels. The algorithm should continue until there is a convergence between the quantization levels of consecutive iterations. The 90° difference can be enforced after the mean points are calculated at each iteration, resulting in uniform quantization levels. Compared with the regular quantization method (see (3.9)), the Lloyd-Max algorithm locates the quantization levels where the continuous phase shifts are denser. As 90° is enforced between levels, the only difference between the two quantization algorithms is the reference phase shift; the Lloyd-Max algorithm computes a non-zero reference phase. In practical applications, the calculated reference phase can be easily implemented through a transmission line of appropriate length. Then, each element across the array can be brought to the computed polarization state by combining the reference

transmission line with regular phase shifters. The element polarization states obtained through PA and CPS, and quantized with two methods, can be found in Fig. 3.4. Each of the four candidate polarization states will be used in the optimization problem in (3.10), and their polarimetric performances will be compared for the three polarizations.

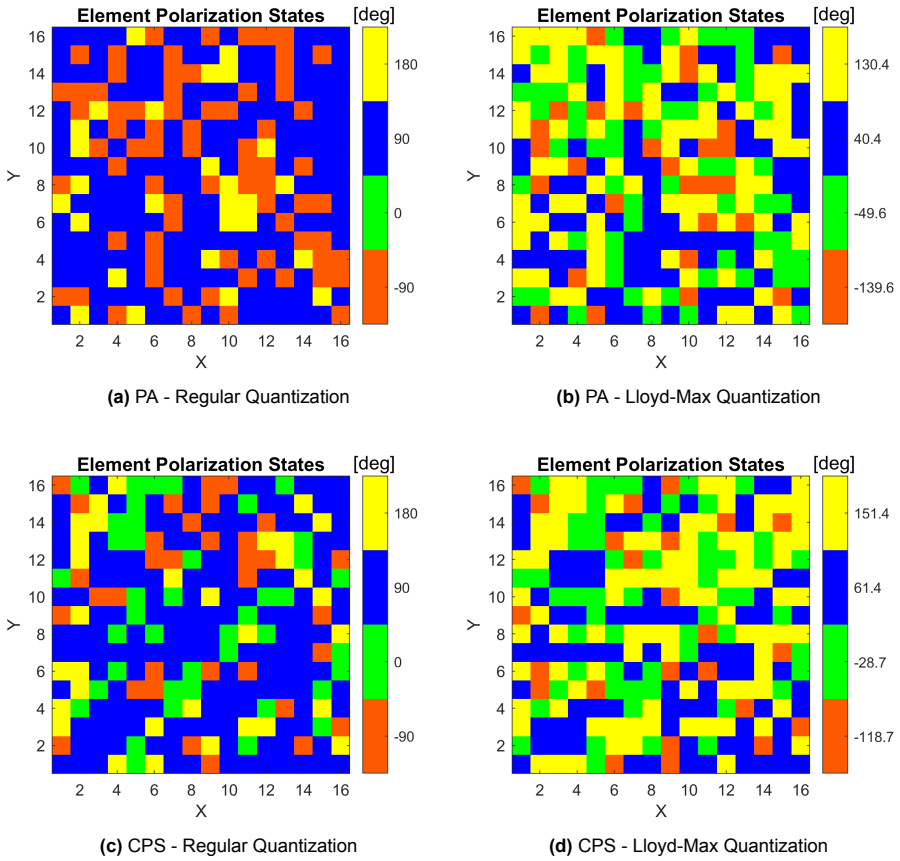


**(a)** PA - Regular Quantization

**(b)** PA - Lloyd-Max Quantization

**(c)** CPS - Regular Quantization

**(d)** CPS - Lloyd-Max Quantization

**Figure 3.4:** Candidate element polarization states

### 3.2.4. Polarimetric Performances of PA and CPS

The polarimetric performances of PA and CPS can be found in Tables 3.2 and 3.3 (same simulation parameters with Section 2.4 and [8] are used):

**Table 3.2:** Polarimetric performance of the PA algorithm quantized with both methods

| **Quant.** | **Direction** | $(\varphi, \eta)$ | **Directivity** [dBi] | **Pin** [W] | **EIRP** [dBW] | **XPL** [dB] | **SLL**$_{co}$ [dB] | **SLL**$_{cr}$[dB] |
|---|---|---|---|---|---|---|---|---|
| **Reg.** | **Broadside** $(u_s = v_s = 0)$ | (0,0) | 19.55 | 182.79 | 42.17 | -41.75 | -14.68 | -17.14 |
| | | (90,0) | 19.55 | 182.79 | 42.17 | -41.75 | -14.68 | -17.14 |
| | | (45,90) | 22.21 | 154.30 | 44.09 | -47.98 | -17.89 | -23.06 |
| | **Steered** $(u_s = v_s = 0.5)$ | (0,0) | 19.06 | 188.01 | 41.80 | -41.38 | -14.90 | -15.01 |
| | | (90,0) | 19.14 | 191.50 | 41.96 | -41.59 | -14.84 | -15.32 |
| | | (45,90) | 21.26 | 174.73 | 43.69 | -48.83 | -17.74 | -22.56 |
| **Lloyd** | **Broadside** $(u_s = v_s = 0)$ | (0,0) | 20.33 | 226.25 | 43.88 | -42.39 | -16.12 | -17.54 |
| | | (90,0) | 20.33 | 226.25 | 43.88 | -42.39 | -16.12 | -17.54 |
| | | (45,90) | 20.67 | 210.42 | 43.90 | -44.02 | -17.37 | -18.92 |
| | **Steered** $(u_s = v_s = 0.5)$ | (0,0) | 19.94 | 222.86 | 43.42 | -42.61 | -16.68 | -18.19 |
| | | (90,0) | 19.97 | 224.99 | 43.49 | -42.94 | -16.31 | -15.54 |
| | | (45,90) | 20.44 | 229.11 | 44.04 | -43.08 | -17.31 | -18.82 |

**Table 3.3:** Polarimetric performance of the CPS algorithm quantized with both methods

| Quant. | Direction | $(\varphi, \eta)$ | **Directivity** [dBi] | **Pin** [W] | **EIRP** [dBW] | **XPL** [dB] | **SLL**$_{co}$ [dB] | **SLL**$_{cr}$[dB] |
|---|---|---|---|---|---|---|---|---|
| **Reg.** | **Broadside** $(u_s = v_s = 0)$ | (0,0) | 19.29 | 165.07 | 41.46 | -43.32 | -18.01 | -16.11 |
| | | (90,0) | 19.29 | 165.07 | 41.46 | -43.32 | -18.01 | -16.11 |
| | | (45,90) | 23.01 | 171.81 | 45.41 | -45.60 | -17.05 | -20.98 |
| | **Steered** $(u_s = v_s = 0.5)$ | (0,0) | 19.13 | 181.03 | 41.71 | -43.51 | -14.25 | -16.44 |
| | | (90,0) | 19.08 | 173.54 | 41.45 | -43.78 | -13.73 | -15.38 |
| | | (45,90) | 22.16 | 183.74 | 44.80 | -45.16 | -17.09 | -20.50 |
| **Lloyd** | **Broadside** $(u_s = v_s = 0)$ | (0,0) | 20.22 | 220.64 | 43.66 | -43.41 | -17.65 | -17.79 |
| | | (90,0) | 20.22 | 220.64 | 43.66 | -43.41 | -17.65 | -17.79 |
| | | (45,90) | 21.37 | 220.22 | 44.80 | -44.63 | -18.27 | -18.24 |
| | **Steered** $(u_s = v_s = 0.5)$ | (0,0) | 19.92 | 229.16 | 43.52 | -42.48 | -17.14 | -17.56 |
| | | (90,0) | 19.72 | 218.30 | 43.12 | -42.90 | -16.66 | -17.39 |
| | | (45,90) | 20.73 | 234.51 | 44.43 | -42.04 | -17.59 | -18.64 |

To see the effect of optimization algorithms without the effect of quantization, the upper halves of both Tables (showing the regular quantization of PA and CPS) can be compared to Table 3.1. It can be seen that, in the broadside radiation case, both PA and CPS improved the EIRP in LHCP synthesis by approximately $2$ dB and $3.4$ dB, respectively. This shows that introducing the LHCP constraints into the optimization problem can enhance the performance of the array in LHCP synthesis. However, there is a considerable EIRP loss in the H and V synthesis performance of the array, $2.3$ dB for PA and $3$ dB for CPS. Moreover, the deterioration in the SLL of co- and cross-polarized fields (specifically for H and V) should be noted; it can be seen that some of the SLL levels exceeded $-15$ dB. Therefore, employing PA and CPS with regular quantization results in a relatively large trade-off for the directivity and EIRP.

When the regular and Lloyd-Max quantizations of PA are compared, from Table 3.2, it can be seen that the Lloyd-Max quantization balances the EIRP of the three polarizations, both for the broadside and for the steered radiation. Such a difference between the two quantization techniques was expected, as the Lloyd-Max technique computed the reference phase of the discrete levels as $40.4°$ (see Fig. 3.4b) depending on the continuous phases. Therefore, Lloyd-Max quantization of PA resulted in a superior performance than regular quantization, as it improved the EIRP of H and V by approximately $1.7$ dB and only resulted in a $0.2$ dB EIRP loss in LHCP. Comparing the Lloyd-Max quantization of PA to Table 3.1, it can be seen that the EIRP loss in H and V is only $0.5$ dB, whereas the EIRP of LHCP is improved considerably by $2$ dB.

When the Lloyd-Max quantization of CPS is compared with that of the PA, it can be seen that for broadside radiation the EIRP of H and V of CPS is only $0.2$ dB less than that of the PA, but at the same time the EIRP of LHCP of CPS is $1$ dB higher than that of PA. In other words, in general, CPS outperformed PA due to more intelligent selection of the common polarization state to be suppressed; it has less number of constraints and hence a wider solution set. Comparing the Lloyd-Max quantized CPS with Table 3.1, it can be seen that the EIRP loss in H and V due to CPS is around $0.8$ dB in the broadside, but the improvement in the EIRP of LHCP is $2.8$ dB. Moreover, when the XPL and SLL levels are considered, it can be seen that the Lloyd-Max quantized CPS maintained those levels approximately around the same level as the algorithm in [8] (see Table 3.1). Therefore, the proposed element polarization state is the one obtained with CPS and quantized with Lloyd-Max; for completeness, several array patterns obtained via the proposed CPS technique (see Fig. 3.4) are shown in Fig. 3.5 (co-pol) and Fig. 3.6 (cross-pol), and the corresponding H port excitation coefficients are shown in Fig. 3.7. Indeed, it can be seen that the suggested CPS algorithm and the proposed element polarization state can successfully steer the beam and suppress the cross-polarized field inside the main-lobe for any radiation direction.

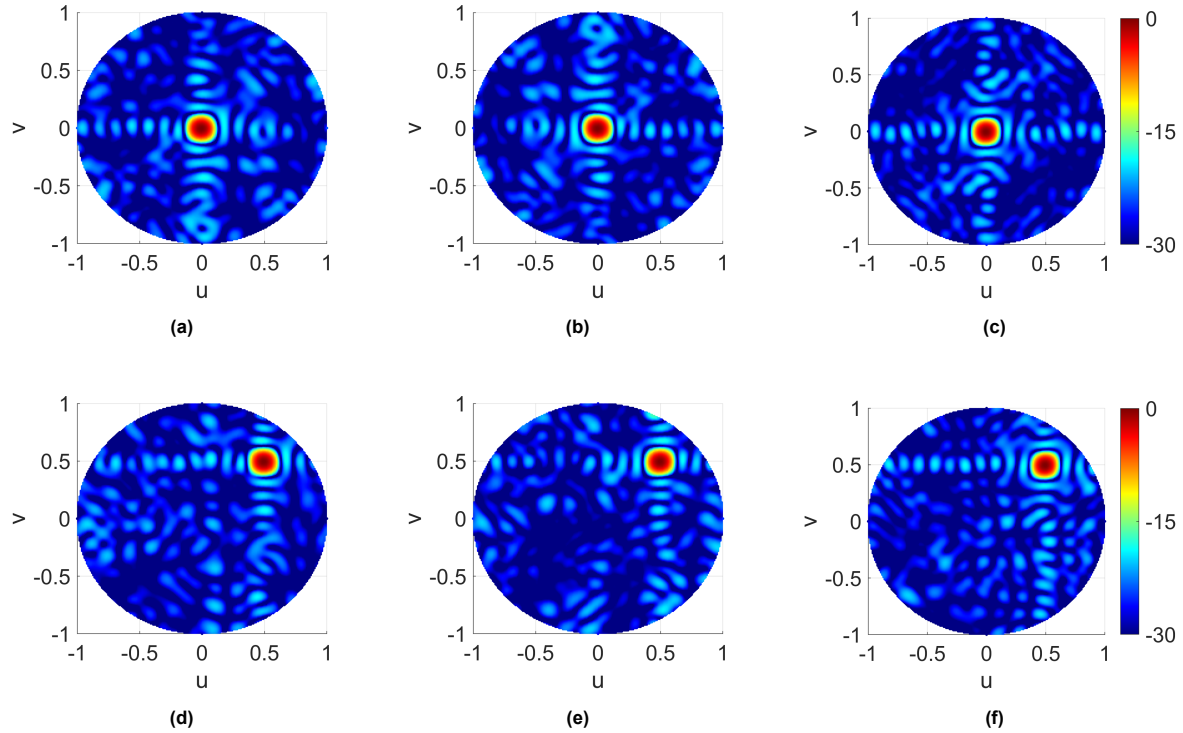


**Figure 3.5:** Co-polarized radiation patterns in the $uv$-plane (normalized, in dB) with the low-cost architecture for a broadside [$u_s = v_s = 0$] and a steered [$u_s = v_s = 0.5$] beam: (a) ($\varphi = 0°, \eta = 0°$) - broadside, (b) ($\varphi = 90°, \eta = 0°$) - broadside., (c) ($\varphi = 45°, \eta = 90°$) - broadside, (d) ($\varphi = 0°, \eta = 0°$) - steered, (e) ($\varphi = 90°, \eta = 0°$) - steered, (f) ($\varphi = 45°, \eta = 90°$) - steered

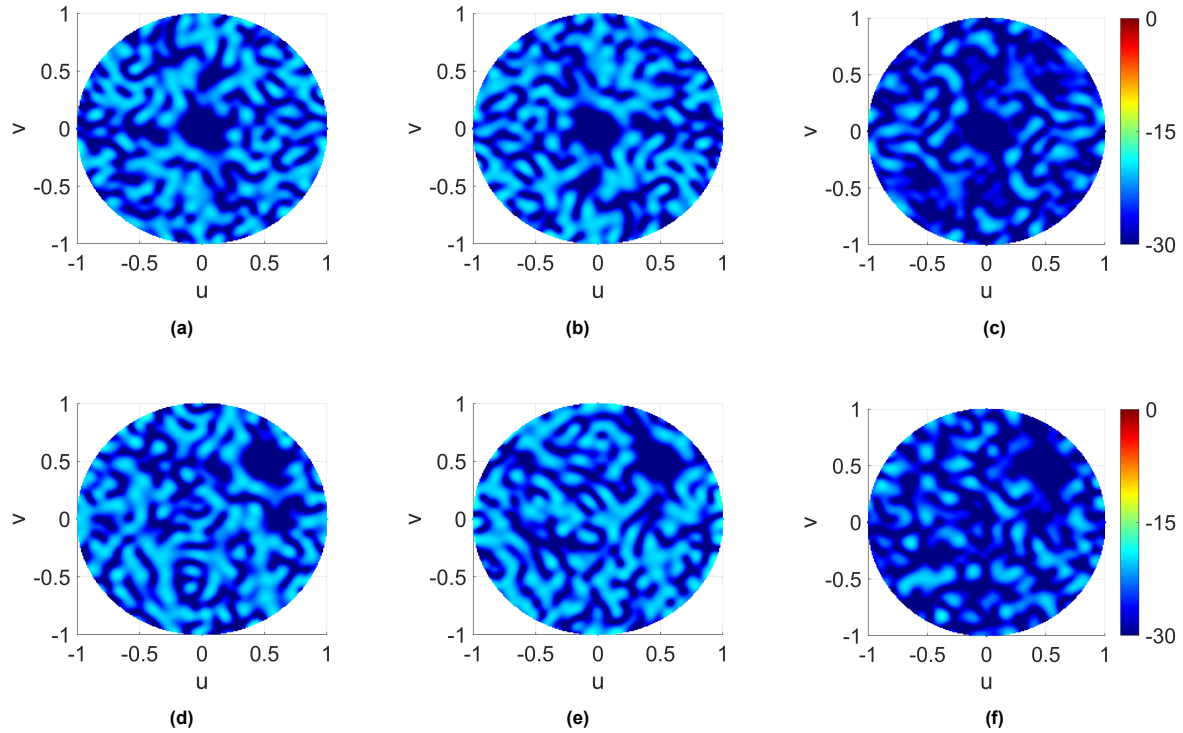


**Figure 3.6:** Cross-polarized radiation patterns in the $uv$-plane (normalized, in dB) with the low-cost architecture for a broadside [$u_s = v_s = 0$] and a steered [$u_s = v_s = 0.5$] beam: (a) ($\varphi = 0°, \eta = 0°$) - broadside, (b) ($\varphi = 90°, \eta = 0°$) - broadside., (c) ($\varphi = 45°, \eta = 90°$) - broadside, (d) ($\varphi = 0°, \eta = 0°$) - steered, (e) ($\varphi = 90°, \eta = 0°$) - steered, (f) ($\varphi = 45°, \eta = 90°$) - steered

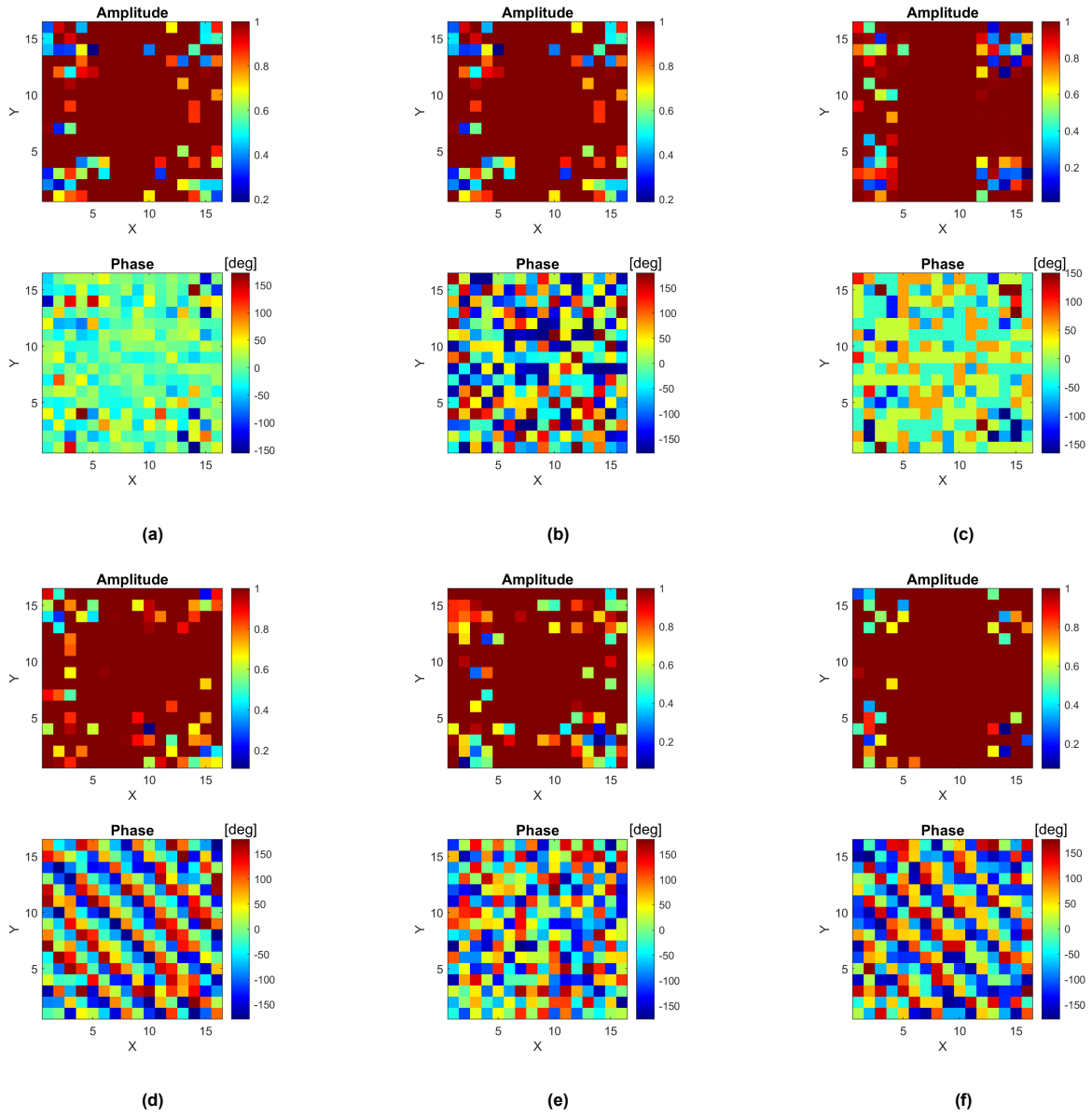


**Figure 3.7:** H-port coefficients for the low-cost architecture for a broadside [$u_s = v_s = 0$] and a steered [$u_s = v_s = 0.5$] beam: (a) ($\varphi = 0°, \eta = 0°$) - broadside, (b) ($\varphi = 90°, \eta = 0°$) - broadside., (c) ($\varphi = 45°, \eta = 90°$) - broadside, (d) ($\varphi = 0°, \eta = 0°$) - steered, (e) ($\varphi = 90°, \eta = 0°$) - steered, (f) ($\varphi = 45°, \eta = 90°$) - steered

## 3.3. Full Wave Simulations

Once the algorithms are examined under ideal assumptions, such as the negligence of coupling and bandwidth effects, full-wave simulations are performed to inspect the robustness of algorithms against non-idealities. In Section 3.3.1, the effect of the inclusion of complex AEPs in the optimization on the polarimetric performance of low-cost PPAA is analyzed. Furthermore, in Section 3.3.2, the effect of the bandwidth on the polarimetric performance of the PPAA is shown.

### 3.3.1. Inclusion of Coupling Effects Inside the Optimization

To examine the effect of the inclusion of coupling effects inside the optimization problem, initially, full-wave simulations are performed using the beamforming weights obtained with the ideal assumptions.

The digital weights and the element polarization states are optimized using the CPS algorithm, subsequently quantized with the Lloyd-Max technique, and applied to the 13 by 13 array shown in Section 2.5:

**Table 3.4:** Polarimetric performance of the CPS-Lloyd Max technique, without considering coupling inside the optimization

| **Direction** | $(\varphi, \eta)$ | **Gain** [dBi] | **Pin**[W] | **EIRP**[dBW] | **XPL**[dB] | **SLL**$_{co}$[dB] | **SLL**$_{cr}$[dB] |
|---|---|---|---|---|---|---|---|
| **Broadside** ($u_s = v_s = 0$) | (0,0) | 22.10 | 128.46 | 43.18 | -26.50 | -19.59 | -19.18 |
| | (90,0) | 22.04 | 128.46 | 43.13 | -32.60 | -19.66 | -20.02 |
| | (45,90) | 24.39 | 136.99 | 45.76 | -30.48 | -19.99 | -20.25 |
| **Steered** ($u_s = v_s = 0.5$) | (0,0) | 20.06 | 93.94 | 39.78 | -19.86 | -17.96 | -17.84 |
| | 90,0) | 20.17 | 94.41 | 39.92 | -20.49 | -17.80 | -18.21 |
| | (45,90) | 22.79 | 144.16 | 44.38 | -20.17 | -18.13 | -18.66 |

Table 3.4 shows the polarimetric performance of the proposed CPS-Lloyd Max technique, obtained with full-wave simulations. It can be seen that the XPL deteriorated considerably, as it exceeded the $-45$ dB constraint by at least more than $15$ dB for broadside radiation, and $25$ dB for steered radiation in each polarization. Therefore, the negligence of coupling effects in the optimization resulted in poor polarimetric performance, and assured that complex AEPs obtained from full-wave simulations have to be included in the optimization.

The algorithm in [8] (see Section 3.1) and the suggested CPS-Lloyd Max algorithm are executed with the AEPs obtained from full-wave simulations ($\mathbf{a}_{HH} \neq \mathbf{1}$, $\mathbf{a}_{VV} \neq \mathbf{1}$, $\mathbf{a}_{HV} \neq \mathbf{0}$, $\mathbf{a}_{VH} \neq \mathbf{0}$); Table 3.5 shows the polarimetric performance of the benchmark algorithm, and Table 3.6 shows the polarimetric performance of the suggested CPS algorithm with Lloyd-Max quantization. It can be seen that, unlike the performance shown in Table 3.4, both algorithms have perfectly met the XPL and SLL criteria, as the coupling effects are considered in the optimization procedure, and u-v grids used for optimization and simulation are the same. When Tables 2.2 and 3.5 are compared (comparing the dual-polarized architecture and the algorithm in [8]), it can be seen that optimizing the low-cost architecture with [8] resulted in an EIRP loss of approximately $1.2$ dB in broadside H and V, and a loss of $5$ dB in broadside LHCP. Moreover, losses are more significant in the steered radiation case. When the performance of the suggested method is considered, it can be seen that the EIRP of LHCP is improved by $1.8$ dB (compared to [8]) with a slight loss of $0.6$ dB in H and almost no loss in V, which is also the case in steered radiation.

**Table 3.5:** Polarimetric performance of the benchmark algorithm [8]

| **Direction** | $(\varphi, \eta)$ | **Gain** [dBi] | **Pin**[W] | **EIRP**[dBW] | **XPL**[dB] | **SLL**$_{co}$[dB] | **SLL**$_{cr}$[dB] |
|---|---|---|---|---|---|---|---|
| **Broadside** ($u_s = v_s = 0$) | (0,0) | 23.44 | 164.90 | 45.61 | -45.00 | -20.00 | -20.00 |
| | (90,0) | 23.33 | 163.30 | 45.46 | -45.00 | -20.00 | -20.00 |
| | (45,90) | 22.73 | 144.45 | 44.33 | -45.00 | -20.00 | -20.00 |
| **Steered** ($u_s = v_s = 0.5$) | (0,0) | 21.62 | 156.51 | 43.56 | -45.00 | -20.00 | -20.00 |
| | (90,0) | 21.57 | 156.72 | 43.52 | -45.00 | -20.00 | -20.00 |
| | (45,90) | 21.69 | 143.02 | 43.24 | -45.00 | -20.00 | -20.00 |

**Table 3.6:** Polarimetric performance of the CPS-Lloyd Max technique, considering coupling inside the optimization

| **Direction** | $(\varphi, \eta)$ | **Gain** [dBi] | **Pin**[W] | **EIRP**[dBW] | **XPL**[dB] | **SLL**$_{co}$[dB] | **SLL**$_{cr}$[dB] |
|---|---|---|---|---|---|---|---|
| **Broadside** ($u_s = v_s = 0$) | (0,0) | 22.96 | 161.18 | 45.03 | -45.00 | -20.00 | -20.00 |
| | (90,0) | 23.17 | 165.16 | 45.35 | -45.00 | -20.00 | -20.00 |
| | (45,90) | 24.22 | 155.51 | 46.14 | -45.00 | -20.00 | -20.00 |
| **Steered** ($u_s = v_s = 0.5$) | (0,0) | 21.14 | 151.03 | 42.93 | -45.00 | -20.00 | -20.00 |
| | (90,0) | 21.54 | 155.91 | 43.47 | -45.00 | -20.00 | -20.00 |
| | (45,90) | 22.97 | 156.42 | 44.41 | -45.00 | -20.00 | -20.00 |

### 3.3.2. Effect of Bandwidth

In the previous section, all optimizations and simulations are performed with respect to the center frequency of $15.5$ GHz. However, by all means, an antenna system does not operate at a single frequency, but at a full band. The designed antenna, explained in Section 2.5, can operate at any frequency between $15.05 - 15.95$ GHz. Indeed, depending on the operating frequency, the coupling effects between the elements will change, and the distance between the antennas, in terms of wavelength, will vary. In other words, AEPs will deviate depending on the frequency. The trivial solution to avoid the degradation of the array performance is to re-perform the optimization with the AEPs obtained at the desired frequency. Clearly, this will ensure the XPL and SLL to be maintained at the operating frequency. However, since the array has to operate at the entire continuous band, performing optimization at each frequency is not a feasible approach. A straightforward solution is to use the beamforming weights obtained at the center frequency for the entire band and examine the change in the polarimetric performance. With this aim, AEPs from $15.75$ GHz are obtained through full-wave simulations, and the previously obtained beamforming coefficients (obtained with the CPS method from $15.5$ GHz) are applied to the array. Table 3.7 illustrates the performance of the array at $15.75$ GHz, excited with the coefficients obtained at $15.5$ GHz. Compared to Table 3.6, it can be seen that the EIRP levels increased, which was expected as the spacing between the elements increased in terms of wavelength as frequency is increased, resulting in a wider array aperture. Moreover, it can be seen that the XPL levels considerably deteriorated, as the optimization is not performed with respect to $15.75$ GHz; however, since XPL levels are still lower than $-33$ dB, the array can be used for polarimetric measurements. Lastly, it can be seen that SLL levels have slightly deteriorated but are still lower than $-18$ dB.

**Table 3.7:** Polarimetric performance when the array is operating at $15.75$ GHz

| **Direction** | $(\varphi, \eta)$ | **Gain** [dBi] | **Pin**[W] | **EIRP**[dBW] | **XPL**[dB] | **SLL**$_{co}$[dB] | **SLL**$_{cr}$[dB] |
|---|---|---|---|---|---|---|---|
| **Broadside** ($u_s = v_s = 0$) | (0,0) | 24.56 | 161.18 | 46.63 | -38.39 | -19.26 | -19.04 |
| | (90,0) | 24.79 | 165.16 | 46.97 | -34.75 | -20.15 | -18.92 |
| | (45,90) | 25.82 | 155.51 | 47.74 | -38.49 | -19.50 | -19.85 |
| **Steered** ($u_s = v_s = 0.5$) | (0,0) | 22.32 | 151.03 | 44.11 | -33.10 | -18.12 | -18.55 |
| | (90,0) | 22.81 | 155.91 | 44.74 | -34.18 | -18.80 | -18.60 |
| | (45,90) | 24.26 | 156.42 | 46.20 | -37.44 | -18.12 | -19.05 |

## 3.4. Intermediate Conclusions

In this chapter, the low-cost solution presented in [8] is extended for the enhanced synthesis of three polarization states. It is observed that the algorithm presented in [8] can synthesize H and V with acceptable polarimetric performance, whereas the EIRP of an arbitrary third polarization state (LHCP in this case) decreases more than $6$ dB (for a 16 by 16 ideal planar array) in broadside compared to a fully-polarized array. To improve the EIRP of LHCP, while keeping the EIRP of H and V at an acceptable level, PA and CPS algorithms are proposed, and their outputs are quantized with regular quantization and Lloyd-Max quantization. It is observed that using CPS along with Lloyd-Max quantization results in an acceptable trade-off between the performances of polarization states. For an ideal 16 by 16 planar array, the proposed method increased the EIRP of LHCP by approximately $3$ dB with a loss of $0.8$ dB in H and V in broadside, compared to [8]. Moreover, the robustness of algorithms against mutual coupling is tested. It is shown that by including electromagnetic effects in the optimization problem, the polarimetric deterioration due to mutual coupling can be avoided. The algorithms are supported with full-wave simulations on a 13 by 13 planar array; it is shown that the proposed algorithm improves the EIRP of LHCP by $1.8$ dB (compared to [8]) on broadside, with negligible losses in H and V.

# 4

# Subarraying Through Tiling Optimization

In this chapter, the subarraying techniques for a PPAA with the low-cost topology shown in Fig. 1.2b will be explained. The subarraying of phased arrays with optimized tiles is a widely used technique to lower the cost of an array. Tile shapes, sizes, and complex excitations have to be optimized for the proper functioning of the array. Although subarraying drastically reduces the cost and complexity of an array, it is not commonly used for PPAAs, as a conventional polarimetric array employs dual-polarized elements, which makes subarraying impractical. However, as shown in Chapter 3, singly fed elements can be used to create a polarimetric array with a trade-off in EIRP, making the subarraying of polarimetric arrays convenient. In Section 4.1, the optimization of the tiling for two polarizations (H and V) will be discussed; this discussion will show that the low-cost architecture shown in [8] can be further made more low-cost, with negligible losses in EIRP. Section 4.2 will demonstrate the polarimetric performance of the array when it is intended to be used for three polarizations (H, V, LHCP).

## 4.1. Synthesis of 2-Polarizations

Subarraying can be performed with different array architectures; however, as will be shown, different architectures will require different optimization frameworks and problems for maintaining the highest achievable gain and EIRP from the array. In this section, optimization of three different subarray architectures and their polarimetric performances are shown.

### 4.1.1. Conventional Tiling

In conventional tiling, elements belonging to the same tile are excited with the same amplitude and phase, as shown in Fig. 4.1. As before, element polarization states will remain quantized and fixed. Moreover, optimization of subarray size and shape will not be discussed; it is assumed that subarrays are composed of two elements placed either horizontally or vertically. In other words, tiling of the array surface with subarrays of two elements will be performed. A similar optimization is performed in [20], where subarrays with two elements are used to cover the surface of the array and shape the output beam. As [20] mainly discusses the shaping effects, it does not discuss polarization synthesis and EIRP levels. Moreover, a steered radiation case is also not considered, where the gain and EIRP

highly depend on the tiling of the array. In this work, tiling of the array will remain fixed across different polarizations and steering scenarios. Therefore, initially, the tiling of the array surface will be performed with respect to H polarization and to the element polarization state given in Fig. 3.1a. Afterward, complex excitation weights for different polarizations and steering directions will be optimized with respect to the fixed tiles and element polarization states.

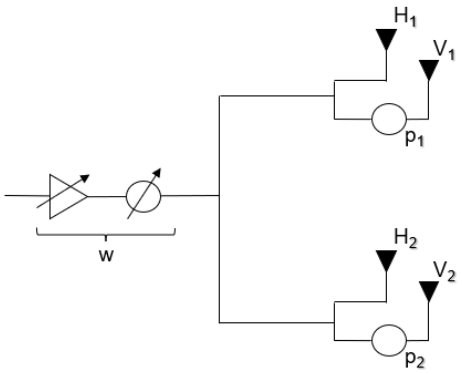


**Figure 4.1:** Subarrayed low-cost architecture

The strategy in this optimization problem is to jointly optimize the tiling and the corresponding excitation coefficients. As described in [20], a binary dictionary matrix **T** is used to hold the information of all possible tiles, $1$ indicates that the element exists in the subarray, and $0$ not. Since only two elements are allowed in a subarray, they can be either vertically or horizontally stacked; for a generic square array of size N by N, the number of candidate tile options for vertical and horizontal tiles is $(N-1)\cdot N$. Therefore, **T** is of size $N^2$ by $2\cdot(N-1)\cdot N$, where each column contains the antennas in the candidate subarray. As the optimal tiles are yet to be chosen by the optimization algorithm, the excitation coefficients have to be optimized for each candidate tile:

$$\mathbf{w} = \mathbf{T}\cdot\mathbf{u} \tag{4.1}$$

$$F_H(\vartheta,\phi) = \mathbf{a}^H(\vartheta,\phi)\mathbf{w} = \mathbf{a}^H(\vartheta,\phi)\mathbf{T}\cdot\mathbf{u} \tag{4.2}$$

$$F_V(\vartheta,\phi) = \mathbf{a}^H(\vartheta,\phi)(\mathbf{w}\odot\mathbf{p}) = \mathbf{a}^H(\vartheta,\phi)((\mathbf{T}\cdot\mathbf{u})\odot\mathbf{p}) \tag{4.3}$$

where **u** is the excitation vector (for all candidate tiles) of size $2\cdot(N-1)\cdot N$ to be optimized. Each entry in **u** shows the common excitation coefficient that the elements of that tile will share. However, (4.1) does not prevent an element from being used by two different subarrays or an element from being idle. To compensate for these, a constraint has to be imposed:

$$\mathbf{Tz} = \mathbf{1} \tag{4.4}$$

where **z** is a $2\cdot(N-1)\cdot N$ by 1 binary selection vector. The entry of **z** being 1 indicates that the corresponding candidate subarray from **T** will be employed in the array, whereas 0 indicates the opposite. In other words, **z** specifies antenna to subarray assignment. Moreover, **z** should be optimized in a way that it is a sparse vector, as most of the entries are ideally have to be 0. However, enforcing $z_i \in \{0,1\}$ is not a convex constraint, hence cannot be solved using convex optimization. To convert this problem into a convex structure, [20] used an iterative scheme and tried to make **z** a binary vector through sequential convex optimizations. As **z** is an optimization variable, its entries can be enforced to get close to 0 or 1 through sequential weighted summations. The optimization problem for this stage is as follows [20]:

$$
\begin{aligned}
\min_{\mathbf{u}^i,\mathbf{z}^i} \quad & \sum_{m=1}^{2N^2-2N} z_m^i \lambda_m^i \\
\text{s.t.} \quad & \mathbb{R}(F_{co}(\vartheta_0,\phi_0)) = 1 \\
& \mathbb{I}(F_{co}(\vartheta_0,\phi_0)) = 0 \\
& \|F_{cr}(\vartheta_k,\phi_k)\|_2 \leq 10^{\frac{XPL}{20}}, \quad \forall(\vartheta_k,\phi_k) \in ML \\
& \|F_{cr}(\vartheta_k,\phi_k)\|_2 \leq 10^{\frac{SLL_{cr}}{20}}, \quad \forall(\vartheta_k,\phi_k) \in SL \\
& \|F_{co}(\vartheta_k,\phi_k)\|_2 \leq 10^{\frac{SLL_{co}}{20}}, \quad \forall(\vartheta_k,\phi_k) \in SL \\
& \mathbf{Tz} = \mathbf{1} \\
& z_m^i \leq 1, \quad \forall m = 1,\cdots,2N^2-2N \\
& \|u_m^i\|_2 \leq z_m^i, \quad \forall m = 1,\cdots,2N^2-2N
\end{aligned}
\tag{4.5}
$$

where $\lambda_m^i = \frac{1}{z_m^{i-1}+\tau^i}$ and $\lambda_m^0 = 1$. The optimization problem in (4.5) should be computed sequentially for a user-defined upper limit: $i = 1,\cdots,K$, which will help the selection vector $\mathbf{z}$ to resemble a binary vector. The objective function improves the sparsity of $\mathbf{z}$, as it resembles an $l1$-norm with weighted elements, which is known to be a lower-bound for cardinality problems. Moreover, entries that are closer to 0 are penalized more. $\lambda_m^i$ is calculated using the $z_m^{i-1}$ (from the previous iteration), it is easy to see that a smaller $z_m^{i-1}$ will result in a greater $\lambda_m^i$, penalizing the smaller entries more. $\tau^i$ is just a small regularization term, avoiding the denominator from being $0$. As the objective function enforces the sparsity of $\mathbf{z}$, the obtained gain will not necessarily be maximal, which will be taken into account in the next step. Therefore, at this stage, the imaginary part of the co-polarized radiation is enforced to be 0 and the real part is enforced to be 1 (normalizing the magnitude to $0$ dB); in Section 2.3, such constraints are shown to be affine. As before, co-polarization in the side-lobe region, cross-polarization in the main-lobe and side-lobe regions are suppressed through inequality constraints, which have the form of a second-order cone and hence convex. $\mathbf{Tz} = \mathbf{1}$ is used to cover the entire array and ensure that none of the elements are used more than once; since it is in the form: $\mathbf{Ax} = \mathbf{b}$, it is affine. $z_m^i$ ensures that the magnitude of any entry in the selection vector does not exceed 1, which is a convex constraint. Lastly, the magnitude of each complex excitation is constrained to be less than the corresponding entry of the selection vector, so that a subarray that is left out ($z_m^i \approx 0$) is not excited ($\| u_m^i \|_2 \approx 0$).

Once the optimal selection vector $\hat{\mathbf{z}}$ satisfying the field constraints is obtained by (4.5), an excitation vector that maximizes the gain for any polarization and radiation direction can be computed:

$$
\begin{aligned}
\min_{\mathbf{u}} \quad & -\mathbb{R}(F_{co}(\vartheta_0,\phi_0)) = -\rho \\
\text{s.t.} \quad & \mathbb{I}(F_{co}(\vartheta_0,\phi_0)) = 0 \\
& \|F_{cr}(\vartheta_i,\phi_i)\|_2 \leq \rho \cdot 10^{\frac{XPL}{20}}, \quad \forall(\vartheta_i,\phi_i) \in ML \\
& \|F_{cr}(\vartheta_i,\phi_i)\|_2 \leq \rho \cdot 10^{\frac{SLL_{cr}}{20}}, \quad \forall(\vartheta_i,\phi_i) \in SL \\
& \|F_{co}(\vartheta_i,\phi_i)\|_2 \leq \rho \cdot 10^{\frac{SLL_{co}}{20}}, \quad \forall(\vartheta_i,\phi_i) \in SL \\
& \|u_n\|_2 \leq 1, \quad \forall n = 1,\cdots,2N^2-2N
\end{aligned}
\tag{4.6}
$$

where the equality constraint is proven to be affine and the inequality constraints are proven to be

convex. Co- and cross-polarized fields can be computed by inserting $\hat{\mathbf{z}}$ into (4.2) and (4.3):

$$F_H(\vartheta,\phi) = \mathbf{a}^H(\vartheta,\phi)\mathbf{w} = \mathbf{a}^H(\vartheta,\phi)\mathbf{T}\cdot(\mathbf{u}\odot\hat{\mathbf{z}}) \tag{4.7}$$

$$F_V(\vartheta,\phi) = \mathbf{a}^H(\vartheta,\phi)(\mathbf{w}\odot\mathbf{p}) = \mathbf{a}^H(\vartheta,\phi)((\mathbf{T}\cdot(\mathbf{u}\odot\hat{\mathbf{z}}))\odot\mathbf{p}) \tag{4.8}$$

It should be noted that $\hat{\mathbf{z}}$ is fixed after solving (4.5), which means that the tiling will remain the same for different polarization states and radiation directions.

The intention at this stage is to see the effect of subarraying on the polarimetric performance of a low-cost array. Therefore, optimizations are performed to make the array synthesize H and V with high performance, where the results will be compared to Table 3.1. The tiling optimization in (4.5) is performed with respect to the field requirements of H. Afterwards, using the obtained $\hat{\mathbf{z}}$, optimization of the excitation coefficients ($\mathbf{u}$) are performed with respect to three polarizations and two steering directions by solving (4.6), separately. The transformation from $\mathbf{u}$ to $\mathbf{w}$ can be made using (4.1). The polarimetric performance of the architecture in Fig. 4.1 is shown in Table 4.1, where the simulation settings of [8] (see Section 2.4) are used. For completeness, several H-port excitation amplitudes and phases are shown in Fig. 4.2, where tiles can be clearly seen.

**Table 4.1:** Polarimetric performance of the subarrayed low-cost architecture shown in Fig. 4.1

| **Direction** | $(\varphi,\eta)$ | **Directivity** [dBi] | **Pin** [W] | **EIRP**[dBW] | **XPL**[dB] | **SLL**$_{co}$[dB] | **SLL**$_{cr}$[dB] |
|---|---|---|---|---|---|---|---|
| **Broadside**$(u_s = v_s = 0)$ | (0,0) | 20.39 | 162.11 | 42.49 | -43.14 | -16.12 | -17.99 |
| | (90,0) | 17.37 | 65.28 | 35.51 | -23.51 | -13.51 | -12.85 |
| | (45,90) | 18.51 | 34.63 | 33.91 | -27.66 | -15.88 | -16.63 |
| **Steered**$(u_s = v_s = 0.5)$ | (0,0) | 17.02 | 42.58 | 33.31 | -21.02 | -13.26 | -12.85 |
| | (90,0) | 17.31 | 59.24 | 35.04 | -23.15 | -14.35 | -14.32 |
| | (45,90) | 17.31 | 54.96 | 34.71 | -25.36 | -14.42 | -14.55 |

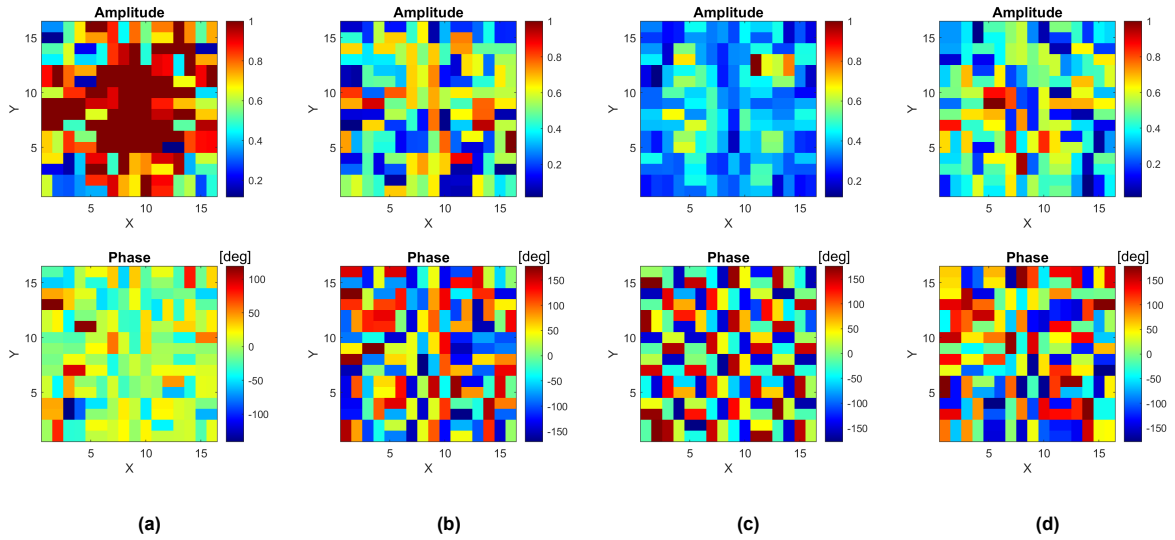


**Figure 4.2:** H-port coefficients for a broadside [$u_s = v_s = 0$] and a steered [$u_s = v_s = 0.5$] beam: (a) ($\varphi = 0°, \eta = 0°$) - broadside, (b) ($\varphi = 90°, \eta = 0°$) - broadside., (c) ($\varphi = 0°, \eta = 0°$) - steered, (d) ($\varphi = 90°, \eta = 0°$) - steered

As can be seen in Table 4.1, the cross-polarization requirements are only sufficient for H in the broadside. In other polarizations and directions, cross-polarization levels considerably exceeded the constraints, deteriorating the polarization purity of the beam. Moreover, when the performance of conventional tiling is compared to the performance of the regular low-cost architecture in Fig. 1.2b, it can be seen that the EIRP of H in broadside dropped by $2$ dB, and the other cases by more than $8$ dB.

It is observed that once tiles are optimized with respect to H and fixed, the polarimetric performance of V drastically deteriorates; unlike the optimization performed in Section 3.1, where optimizing element polarization states with respect to H did not deteriorate the performance of the array in V, as it could be accounted for with digital beamforming in the final stage. To overcome this problem, a new subarray architecture and an associated optimization strategy are proposed in Section 4.1.2.

### 4.1.2. Gain Shared - Phase Decoupled Tiles (GSPD)

In Section 4.1.1, it is shown that subarraying can be performed on a PPAA when each element with an optimized polarization state is excited by a single RF chain. However, it is also shown that exciting both antennas in the same subarray with the same amplitude and phase not only limits the EIRP, but also deteriorates the polarization purity and side-lobe levels. To overcome this, the array architecture can be relaxed such that the antennas in the same subarray will be excited with the same amplitude but with a different phase. The decoupling of the phase across the subarray will give additional freedom to the array, which can help to maintain the polarization purity without decreasing the EIRP. The proposed RF architecture is shown in Fig. 4.3:

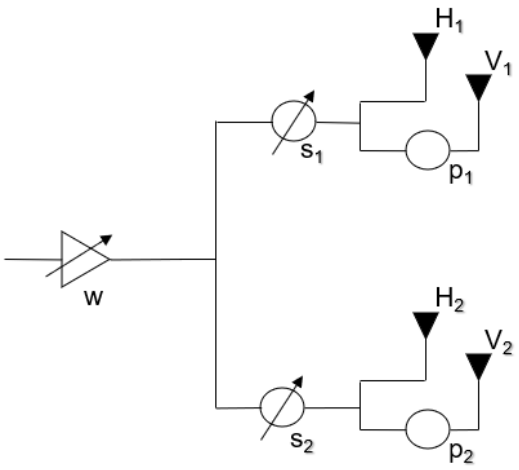


**Figure 4.3:** Gain Shared - Phase Decoupled (GSPD) architecture

where $w$ represents the variable gain amplifier supplying both antennas in the same subarray, $s_1$ and $s_2$ represent the variable phase shifters of the antennas, $p_1$ and $p_2$ represent the previously optimized fixed phase shifters (see Fig. 3.1a). The algorithm explained in Section 4.1.1 cannot be used for the architecture in Fig. 4.3, as it does not allow antennas in the same subarray to have different phases. To overcome this issue, an excitation synthesis algorithm explained in [21] is combined along with the algorithm in [20]. Once the optimal tiles are obtained with (4.5), excitation coefficients are optimized with the algorithm in [21]. The flow chart for the optimization procedure can be seen in Fig. 4.4.

As before, optimization starts with obtaining the element polarization states. The polarization states in Fig. 3.1a are used, as the intended polarizations at this stage are H and V. In the next step, the desired polarization is selected and the optimization problem in (4.5) is performed to obtain the optimal tiling ($\hat{\mathbf{z}}$) with respect to it and the previously picked element polarization states. In this section, tiling optimization is performed with respect to H; it will be shown that V can be synthesized with the same polarimetric performance as H (unlike the degradation observed in conventional tiling), because of the additional degree of freedom provided by the decoupling of phases. In the final stage, one of the intended polarizations is picked and the optimization problem in [21] is solved using $\hat{\mathbf{z}}$.

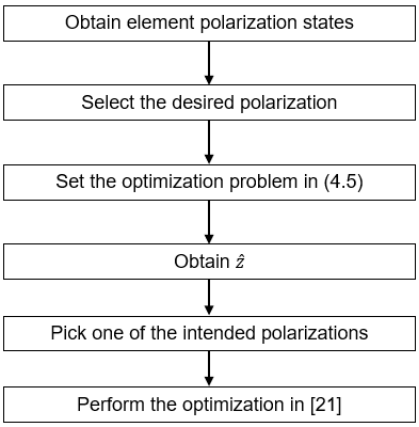


**Figure 4.4:** Flowchart of the overall synthesis procedure for the GSPD architecture

The optimization problem in [21] can provide antenna groups with uniform excitation magnitudes and varying phases. However, grouping has to be done prior to the process and must be an input since the algorithm does not optimize the way elements are grouped. The optimization problem for obtaining uniform amplitude excitation coefficients is as follows:

$$
\begin{aligned}
\min_{\mathbf{w}} \quad & -\kappa \cdot \mathbb{R}(F_{co}(\vartheta_0,\phi_0)) + \sum_{m=1}^{N/2} \|\mathbf{w}^m\|_\infty \\
\text{s.t.} \quad & \mathbb{I}(F_{co}(\vartheta_0,\phi_0)) = 0 \\
& \|F_{cr}(\vartheta_i,\phi_i)\|_2 \leq \mathbb{R}(F_{co}(\vartheta_0,\phi_0)) \cdot 10^{\frac{XPL}{20}}, \quad \forall(\vartheta_i,\phi_i) \in ML \\
& \|F_{cr}(\vartheta_i,\phi_i)\|_2 \leq \mathbb{R}(F_{co}(\vartheta_0,\phi_0)) \cdot 10^{\frac{SLL_{cr}}{20}}, \quad \forall(\vartheta_i,\phi_i) \in SL \\
& \|F_{co}(\vartheta_i,\phi_i)\|_2 \leq \mathbb{R}(F_{co}(\vartheta_0,\phi_0)) \cdot 10^{\frac{SLL_{co}}{20}}, \quad \forall(\vartheta_i,\phi_i) \in SL \\
& \|w_n\|_2 \leq 1, \quad \forall n = 1,\cdots,N \\
& 0 \leq \kappa \leq 1
\end{aligned}
\tag{4.9}
$$

The second term in the objective function is a mixed $l_1/l_\infty$-norm ($\|\cdot\|_{1,\infty}$) of subarrays with two elements, where $\mathbf{w}^m$ represents the vector containing the coefficients for the $m^{th}$ subarray. Minimizing the $l_1/l_\infty$-norm will force both elements of any $m^{th}$ subarray to be excited with the amplitude $\|\mathbf{w}^m\|_\infty$. However, the $l1$-norm in the second term is known to enforce sparsity, which decreases the gain. Therefore, as in the previous chapters, the first term in the objective function is included to increase the gain. A slack variable $\kappa$ is introduced to relax the effect of the first term, as it is observed that antennas in the same group are excited with different amplitudes when the two terms of the objective function are of equal importance. Since the objective function is convex and the constraints are the same as before, (4.9) is a convex problem and can be solved by existing libraries [19]. The polarimetric performance of the GSPD architecture is shown in Table 4.2, where $\kappa$ is taken to be 0.6 by manual tuning. For completeness, several array patterns and H-port coefficients are shown in Fig. 4.5 and Fig. 4.6.

As can be seen in Table 4.2, the suggested algorithm can maintain the XPL, SLL$_{co}$, and SLL$_{cr}$ of H and V around the same level as the architecture shown in Fig. 1.2b (see Table 3.1). However, as expected, the performance of the architecture drops considerably for LHCP (both in terms of EIRP and polarization purity), as the element polarization and tiling optimizations are performed with respect to H. Moreover, comparing the EIRP levels in Tables 3.1 and 4.2, it can be seen that EIRP only drops by $1$ dB when the tiling optimization is performed through the optimization framework given in Fig. 4.4,

while it was around $2$ dB for H and more than $8$ dB with the algorithm suggested in [20]. In other words, the architecture shown in Fig. 4.3 resulted in a slight EIRP loss of $1$ dB in H and V, while reducing the number of gain amplifiers by half compared to Fig. 1.2b.

**Table 4.2:** Polarimetric performance of the subarrayed low-cost architecture shown in Fig. 4.3

| **Direction** | $(\varphi, \eta)$ | **Directivity** [dBi] | **Pin** [W] | **EIRP** [dBW] | **XPL** [dB] | **SLL**$_{co}$ [dB] | **SLL**$_{cr}$[dB] |
|---|---|---|---|---|---|---|---|
| **Broadside** $(u_s = v_s = 0)$ | (0,0) | 21.11 | 171.66 | 43.45 | -43.28 | -17.80 | -18.01 |
| | (90,0) | 21.11 | 171.66 | 43.45 | -43.28 | -17.80 | -18.01 |
| | (45,90) | 20.05 | 95.35 | 39.84 | -42.28 | -15.76 | -19.15 |
| **Steered** $(u_s = v_s = 0.5)$ | (0,0) | 20.50 | 175.19 | 42.94 | -43.07 | -17.52 | -18.30 |
| | (90,0) | 20.49 | 170.15 | 42.80 | -43.31 | -16.69 | -15.89 |
| | (45,90) | 19.55 | 87.65 | 38.98 | -42.93 | -16.19 | -18.84 |

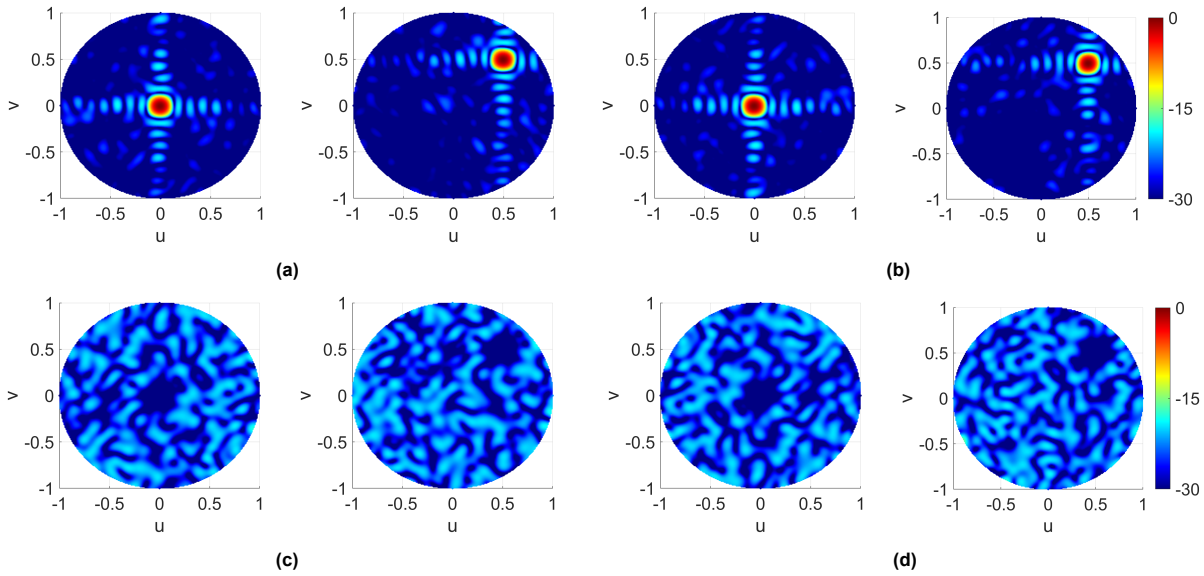


**Figure 4.5:** Array radiation patterns in the $uv$-plane (normalized, in dB) with the proposed architecture in Fig. 4.3 for a broadside $[u_s = v_s = 0]$ and a scanned $[u_s = v_s = 0.5]$ beam: (a) $(\varphi = 0°, \eta = 0°)$ - co-pol., (b) $(\varphi = 90°, \eta = 0°)$ - co-pol., (c) $(\varphi = 0°, \eta = 0°)$ - cross-pol., (d) $(\varphi = 90°, \eta = 0°)$ - cross-pol.

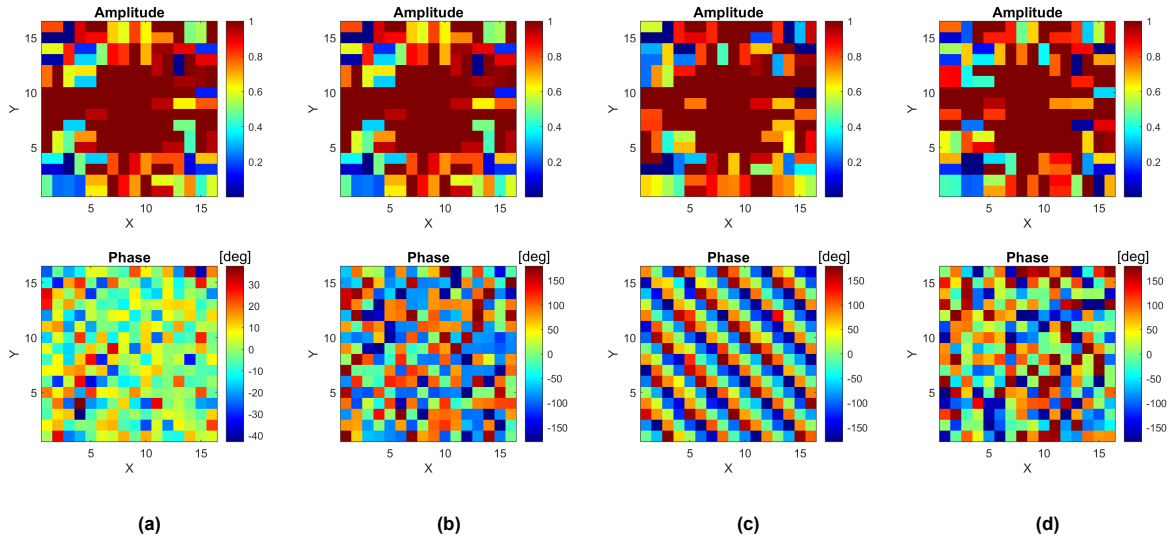


**Figure 4.6:** H-port coefficients for a broadside $[u_s = v_s = 0]$ and a steered $[u_s = v_s = 0.5]$ beam: (a) $(\varphi = 0°, \eta = 0°)$ - broadside, (b) $(\varphi = 90°, \eta = 0°)$ - broadside., (c) $(\varphi = 0°, \eta = 0°)$ - steered, (d) $(\varphi = 90°, \eta = 0°)$ - steered

### 4.1.3. Fixed Gain - Phase Decoupled Tiles (FGPD)

In the previous section, it was shown that subarraying of a PPAA is indeed possible using the architecture in Fig. 4.3 with a slight loss in EIRP. From the excitation amplitudes shown in Fig. 4.6, it can be seen that they have almost remained the same for different polarizations and radiation directions; in other words, polarization synthesis and beam steering are mainly performed through the phases, whereas side-lobe suppression is controlled both by the amplitudes and phases. Considering this fact, the architecture in Fig. 4.3 can be further simplified to have fixed-gain amplifiers as shown in Fig. 4.7. Fixing the amplifier gain will limit the beamforming and polarization synthesis capabilities of the array; however, it will reduce the complexity of the array by a large amount, as a variable gain amplifier requires a lot of sub-components. The new beamforming weights for different polarizations and radiation directions are obtained by multiplying the phases in Fig. 4.6 with the amplitudes given in Fig. 4.6a. The polarimetric performance of the FGPD architecture is shown in Table 4.3. For completeness, several array patterns are shown in Fig. 4.8.

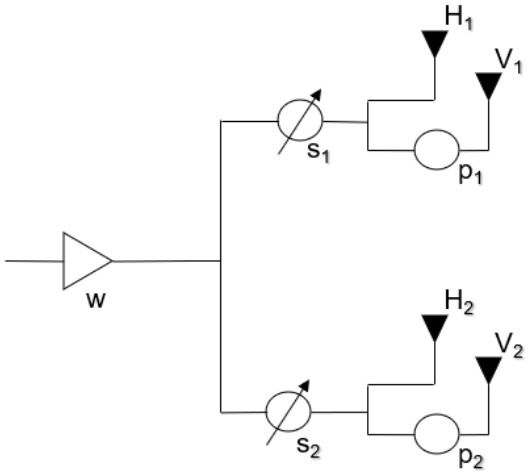


**Figure 4.7:** Fixed Gain - Phase Decoupled (FGPD) architecture

**Table 4.3:** Polarimetric performance of the subarrayed low-cost architecture shown in Fig. 4.7

| **Direction** | $(\varphi, \eta)$ | **Directivity** [dBi] | **Pin** [W] | **EIRP** [dBW] | **XPL** [dB] | **SLL**$_{co}$ [dB] | **SLL**$_{cr}$[dB] |
|---|---|---|---|---|---|---|---|
| **Broadside** $(u_s = v_s = 0)$ | (0,0) | 21.11 | 171.66 | 43.45 | -43.28 | -17.80 | -18.01 |
| | (90,0) | 21.11 | 171.66 | 43.45 | -43.28 | -17.80 | -18.01 |
| | (45,90) | 19.31 | 171.66 | 41.65 | -16.54 | -15.85 | -14.58 |
| **Steered** $(u_s = v_s = 0.5)$ | (0,0) | 20.42 | 171.66 | 42.77 | -34.54 | -17.63 | -16.26 |
| | (90,0) | 20.47 | 171.66 | 42.82 | -35.61 | -17.39 | -16.00 |
| | (45,90) | 18.65 | 171.66 | 41.00 | -14.17 | -15.62 | -13.34 |

Comparing Tables 4.2 and 4.3, it can be seen that SLL$_{cr}$ slightly deteriorated for steered radiation after fixing the amplifier gain, which was expected since the amplitudes of beamforming weights have a huge impact on side-lobe levels. When polarization purity is considered, it can be seen that XPL levels of H and V for broadside radiation maintained at $-43.28$ dB as before, but deteriorated to $-35$ dB for steered radiation. Although $-35$ dB is poor compared to the $-45$ dB purity requirement, it is still acceptable for weather and automotive radar applications. Moreover, the EIRP levels of the FGPD architecture for H and V remained the same as those of the GSPD architecture, which was expected since the amplitudes of the beamforming coefficients in Fig. 4.6 are close to each other. Since the intention of Section 4.1 is to make the low-cost solution given in [8] even more low-cost, deterioration in LHCP is not of concern at this point.

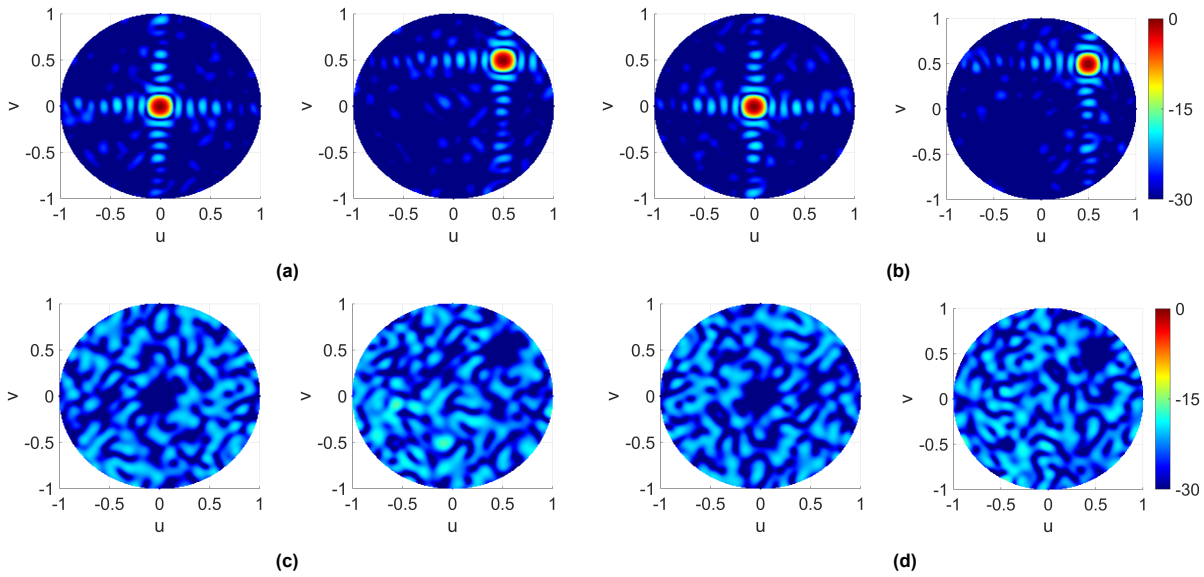


**Figure 4.8:** Array radiation patterns in the $uv$-plane (normalized, in dB) with the proposed architecture in Fig. 4.7 for a broadside [$u_s = v_s = 0$] and a scanned [$u_s = v_s = 0.5$] beam: (a) ($\varphi = 0°, \eta = 0°$) - co-pol., (b) ($\varphi = 90°, \eta = 0°$) - co-pol., (c) ($\varphi = 0°, \eta = 0°$) - cross-pol., (d) ($\varphi = 90°, \eta = 0°$) - cross-pol.

## 4.2. Synthesis of 3-Polarizations

The synthesis of H and V with low-cost subarrayed phased arrays can be extended to the synthesis of an arbitrary third polarization, LHCP. Sections 4.1.2 and 4.1.3 showed that once the element polarization state and the tiling optimizations are performed with respect to H, polarimetric performance of array for LHCP synthesis considerably drops. As there is a demand for the synthesis of three polarizations, subarraying is also performed to make the GSPD architecture (see Fig. 4.3) synthesize H, V and LHCP with improved polarimetric performance. The CPS algorithm is used to optimize the tiling of the array. Initially, the previously obtained element polarization state in Fig. 3.4d, which was shown to yield the best trade-off among the three polarizations, is fixed, and then the tiling optimization (see Fig. 4.4) is performed with respect to it and the desired polarization: $(\phi = 27, \eta = 90)$, which was shown to act as a common state for H and LHCP. The polarimetric performance is shown in Table 4.4, where $\kappa$ in (4.9) is taken to be between 0.6-0.7 through manual tuning. For completeness, several array patterns and H-port coefficients are shown in Fig. 4.9, Fig. 4.10, and Fig. 4.11.

**Table 4.4:** Polarimetric performance of the GSPD architecture for the synthesis of 3 polarizations

| **Direction** | $(\varphi, \eta)$ | **Directivity** [dBi] | **Pin** [W] | **EIRP**[dBW] | **XPL**[dB] | **SLL**$_{co}$[dB] | **SLL**$_{cr}$[dB] |
|---|---|---|---|---|---|---|---|
| **Broadside**$(u_s = v_s = 0)$ | (0,0) | 20.41 | 140.54 | 41.89 | -39.43 | -16.04 | -17.92 |
| | (90,0) | 20.41 | 140.54 | 41.89 | -39.43 | -16.04 | -17.92 |
| | (45,90) | 21.56 | 163.63 | 43.70 | -41.87 | -16.56 | -18.85 |
| **Steered**$(u_s = v_s = 0.5)$ | (0,0) | 19.88 | 140.48 | 41.36 | -39.34 | -16.40 | -17.73 |
| | (90,0) | 19.61 | 129.39 | 40.73 | -39.69 | -15.53 | -16.57 |
| | (45,90) | 21.04 | 172.62 | 43.42 | -39.86 | -16.43 | -19.07 |

When Tables 3.3 and 4.4 are compared (to observe the effect of subarraying on the synthesis of 3 polarizations), subarraying only resulted in a loss of $1.8$ dB of EIRP in H and V (slightly more in steered radiation) and around $1$ dB in LHCP. Moreover, compared to Table 4.2, where tiling is performed considering only the performances of H and V, the EIRP of H and V dropped by approximately $1.5$ dB; however, the EIRP of LHCP is improved by approximately $4$ dB. Although EIRP levels did not deteriorate by a large amount after subarraying, XPL levels dropped to approximately $-40$ dB, which is

still acceptable. In addition to XPL, there is a considerable deterioration in $SLL_{co}$ of each polarization, which is around $-16$ dB. In other words, it is shown that tiling can be used to enhance the performance of H, V, and LHCP jointly at the cost of a slight deterioration in purity and side-lobe levels.

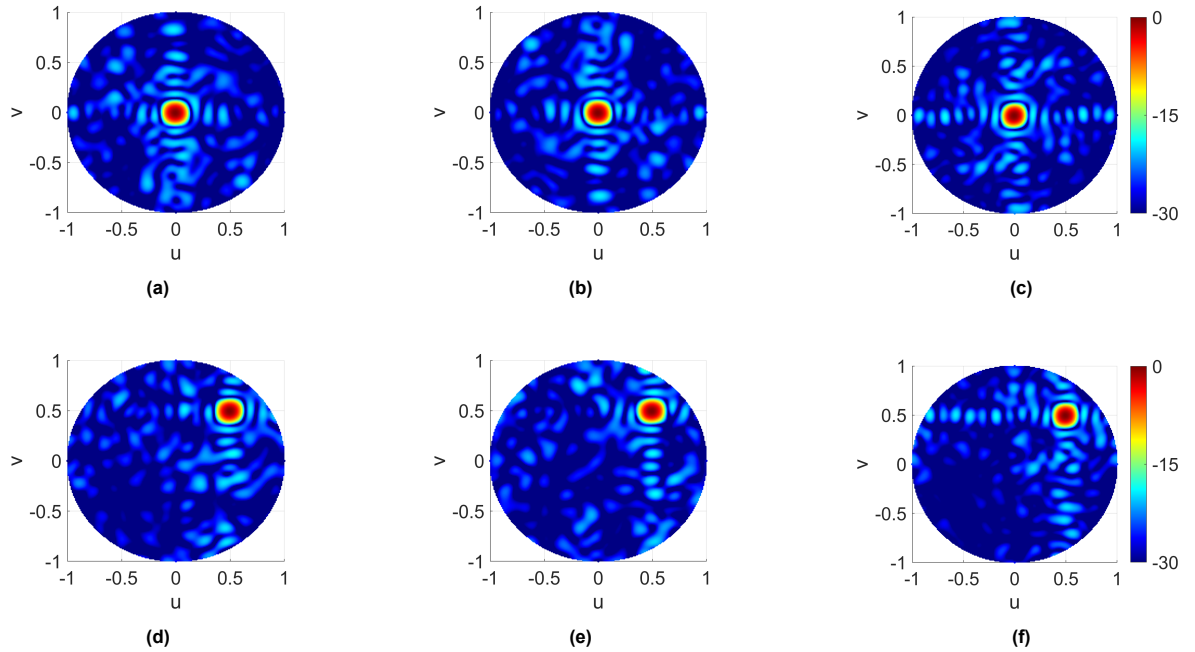


**Figure 4.9:** Co-polarized radiation patterns in the $uv$-plane (normalized, in dB) with the GSPD architecture for a broadside [$u_s = v_s = 0$] and a steered [$u_s = v_s = 0.5$] beam: (a) ($\varphi = 0°, \eta = 0°$) - broadside, (b) ($\varphi = 90°, \eta = 0°$) - broadside., (c) ($\varphi = 45°, \eta = 90°$) - broadside, (d) ($\varphi = 0°, \eta = 0°$) - steered, (e) ($\varphi = 90°, \eta = 0°$) - steered, (f) ($\varphi = 45°, \eta = 90°$) - steered

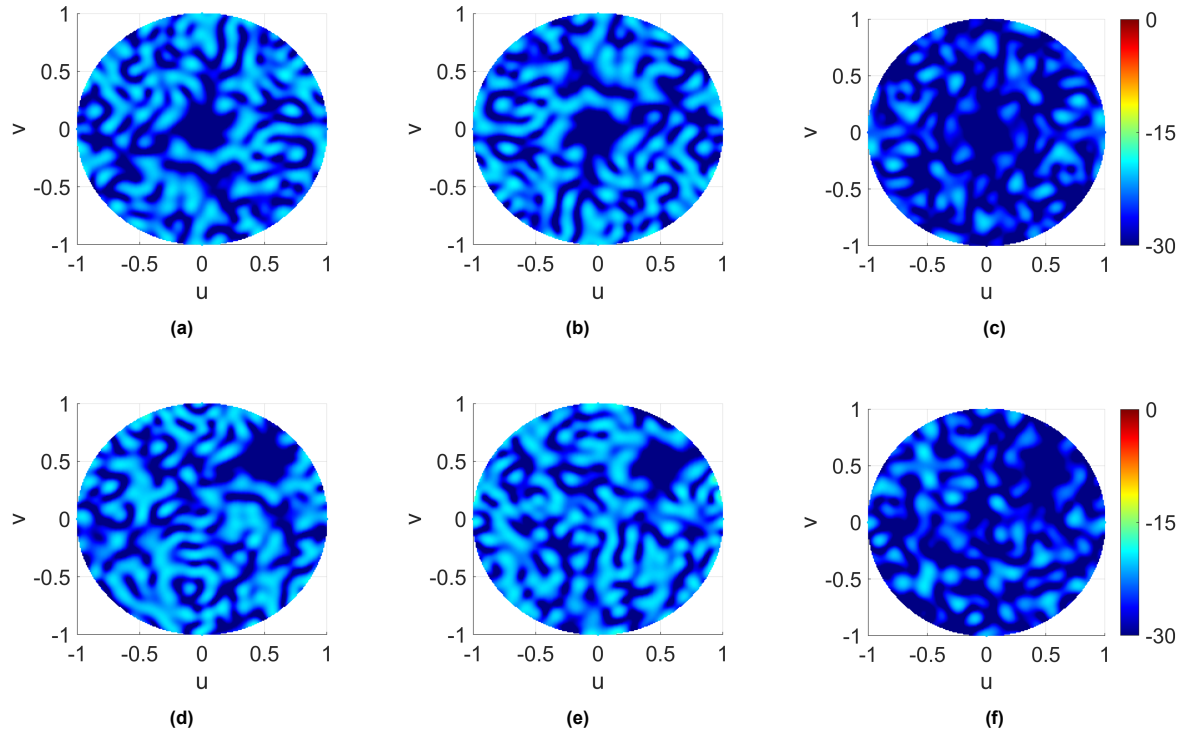


**Figure 4.10:** Cross-polarized radiation patterns in the $uv$-plane (normalized, in dB) with the GSPD architecture for a broadside [$u_s = v_s = 0$] and a steered [$u_s = v_s = 0.5$] beam: (a) ($\varphi = 0°, \eta = 0°$) - broadside, (b) ($\varphi = 90°, \eta = 0°$) - broadside., (c) ($\varphi = 45°, \eta = 90°$) - broadside, (d) ($\varphi = 0°, \eta = 0°$) - steered, (e) ($\varphi = 90°, \eta = 0°$) - steered, (f) ($\varphi = 45°, \eta = 90°$) - steered

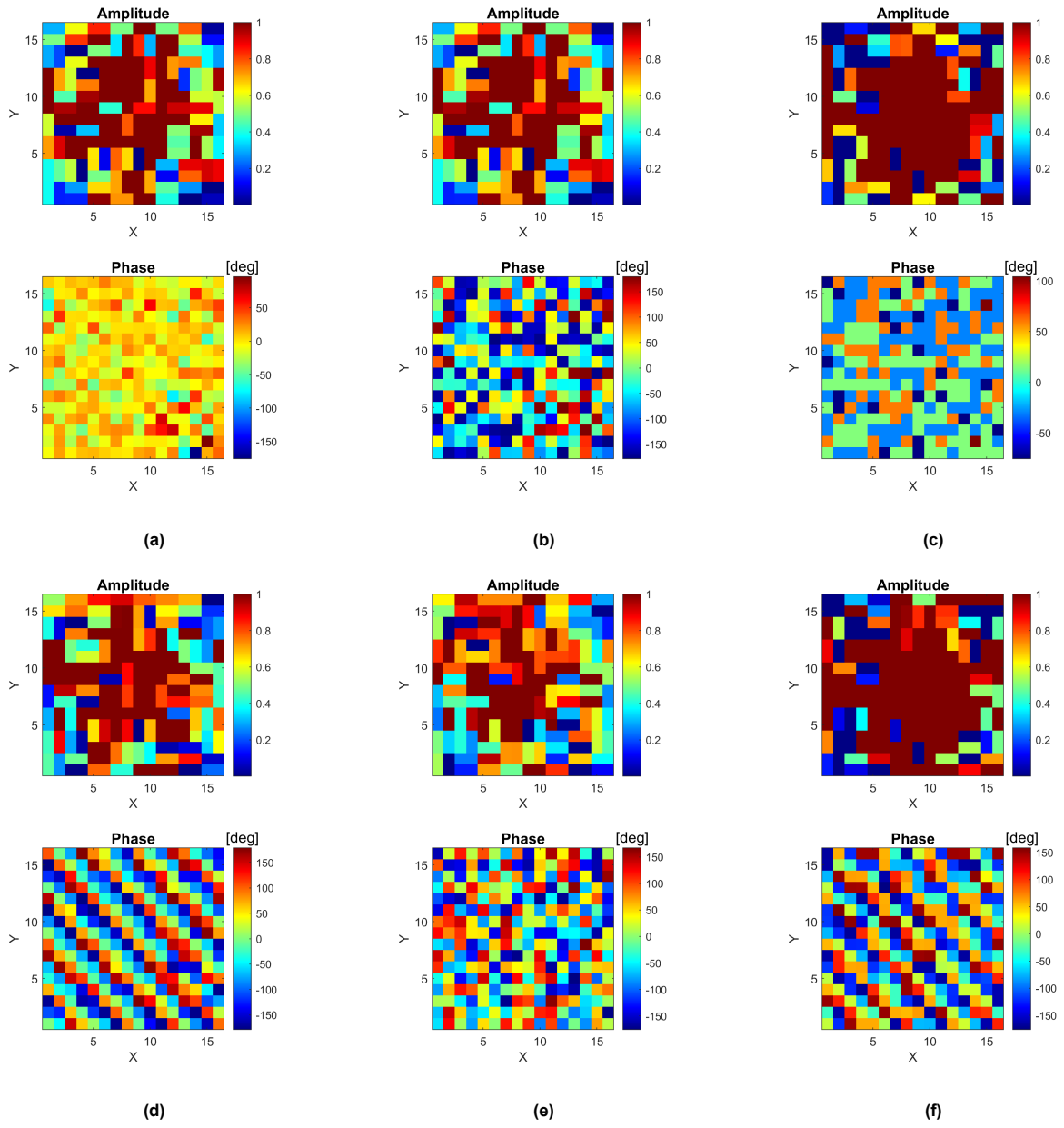


**Figure 4.11:** H-port coefficients for the GSPD architecture for a broadside [$u_s = v_s = 0$] and a steered [$u_s = v_s = 0.5$] beam: (a) ($\varphi = 0°, \eta = 0°$) - broadside, (b) ($\varphi = 90°, \eta = 0°$) - broadside., (c) ($\varphi = 45°, \eta = 90°$) - broadside, (d) ($\varphi = 0°, \eta = 0°$) - steered, (e) ($\varphi = 90°, \eta = 0°$) - steered, (f) ($\varphi = 45°, \eta = 90°$) - steered

## 4.3. Intermediate Conclusions

In this chapter, subarraying of a low-cost PPAA is discussed. After element polarization states are optimized and ports are combined into a single RF chain in Chapter 3, the low-cost topology in Fig. 1.2b is made even more low-cost by subarraying. Initially, conventional subarraying optimization is performed, where the antennas in the same subarray are excited with the same amplitude and phase. It is observed that the polarimetric performance deteriorates considerably for any polarization other than H and scanned radiation. Subsequently, a new subarray architecture (GSPD) is proposed, along with an optimization framework, which allows antennas in the same subarray to be excited with different phases, but with the same amplitude. Initially, optimizations are performed to operate the PPAA for

H and V; it is found that with only a $1$ dB (for an ideal 16 by 16 planar array) loss of EIRP in H and V in broadside and in steered directions compared to [8], PPAA cost can be significantly lowered. Afterwards, it is observed that the subarray amplitudes roughly remain the same for H and V in broadside and steered radiation. To exploit this and make the array further low-cost, variable-gain amplifiers in the GSPD architecture are fixed, and the FGPD architecture is proposed. Fixing the amplifier gain has been shown to result in a deterioration of cross-polarization levels for steered radiation; however, as XPL did not exceed $-35$ dB, it can be used in PPAAs. Finally, the GSPD architecture is optimized for the synthesis of three polarizations. The tiling optimization is performed with respect to the common polarization state (as in CPS), and it is shown that with only an EIRP loss of approximately $1.5$ dB in H and V, and $1$ dB in LHCP, the cost of the architecture in Fig. 1.2b can be reduced further.

# 5

# Joint Pattern Shaping and Polarization Synthesis with Convex Relaxation

Pattern shaping is a widely used technique in phased arrays. For example, shaped beams can be used in weather radars to relax operational burden and help the operator to analyze a wider angular region in the elevation plane simultaneously. However, as explained before, many applications require high polarization purity, which necessitates the joint synthesis of pattern and polarization. Although there are many studies in the literature dealing with pattern shaping, polarization synthesis is not considered along with it. Indeed, studies considering pattern and polarization requirements jointly, require the use of a dual-polarized antenna element, increasing the complexity of the array. In Section 5.1, the joint pattern and polarization synthesis will be carried out for an array employing dual-polarized elements; in Section 5.2, the joint synthesis problem will be performed with the low-cost architecture in Fig. 1.2b by replacing fixed phase shifters with variable phase shifters.

## 5.1. Pattern&Polarization Synthesis with Dual-Polarized Elements

The problem of pattern synthesis is not convex by nature, unlike the polarization synthesis with a focused beam discussed in Chapter 2. The non-convexity of the problem comes from the shaping constraints of the pattern. In addition to upper-bound constraints imposed to suppress side-lobes, lower-bound constraints have to be imposed on the main-lobe for shaping. However, as can be seen from (2.12), a convex problem in standard form does not allow lower-bound constraints. To handle such non-convex constraints, semidefinite relaxation (SDR) can be utilized; as summarized in [22], SDR can solve non-convex and quadratically constrained optimization problems. It must be noted that, unlike convex optimization, the solution of SDR is not necessarily optimal with respect to the original non-convex problem; however, it provides a highly accurate solution.

In [23], SDR is used to shape the pattern for a phased array with singly fed antennas. A similar approach can be carried out to jointly synthesize pattern and polarization for a phased array with dual-polarized elements. A standard SDR problem has the form [22]:

$$\begin{aligned} \min_{X\in\mathbb{S}^n} \quad & \mathrm{Tr}(CX) \\ \text{s.t.} \quad & \mathrm{Tr}(A_iX) \leq, b_i, \quad i=1,\ldots,m, \\ & \mathrm{Tr}(B_iX) \geq, c_i, \quad i=1,\ldots,m, \\ & \mathrm{Tr}(D_iX) = d_i, \quad i=1,\ldots,m, \\ & X \succeq 0. \end{aligned} \tag{5.1}$$

where $\mathbf{X}=\mathbf{x}\mathbf{x}^T$, $\mathrm{Tr}$ is the trace operator and $\mathbf{X} \succeq 0$ indicates positive semidefiniteness (PSD). The field expressions in (2.10) and (2.11) can be manipulated to express the problem in the form of (5.1):

$$F_{co,i} = \{\cos(\varphi)\mathbf{a}^H_{HH,i} + \sin(\varphi)e^{-j\eta}\mathbf{a}^H_{VH,i}\}\mathbf{w}_H + \{\cos(\varphi)\mathbf{a}^H_{HV,i} + \sin(\varphi)e^{-j\eta}\mathbf{a}^H_{VV,i}\}\mathbf{w}_V \tag{5.2}$$

$$F_{cr,i} = \{-\sin(\varphi)\mathbf{a}^H_{HH,i} + \cos(\varphi)e^{-j\eta}\mathbf{a}^H_{VH,i}\}\mathbf{w}_H + \{-\sin(\varphi)\mathbf{a}^H_{HV,i} + \cos(\varphi)e^{-j\eta}\mathbf{a}^H_{VV,i}\}\mathbf{w}_V \tag{5.3}$$

Rewriting in simpler terms:

$$F_{co,i} = \mathbf{a}^H_{Hco,i}\mathbf{w}_H + \mathbf{a}^H_{Vco,i}\mathbf{w}_V \tag{5.4}$$

$$F_{cr,i} = \mathbf{a}^H_{Hcr,i}\mathbf{w}_H + \mathbf{a}^H_{Vcr,i}\mathbf{w}_V \tag{5.5}$$

The rest of the derivations will be performed for the co-polarized field using (5.4), the same approach can be carried out for the cross-polarized field using (5.5). (5.4) can be further expressed through a vector product:

$$F_{co,i} = \begin{bmatrix}\mathbf{a}^H_{Hco,i} & \mathbf{a}^H_{Vco,i}\end{bmatrix}\begin{bmatrix}\mathbf{w}_H \\ \mathbf{w}_V\end{bmatrix} = \mathbf{a}^H_{co,i}\mathbf{w}_{co} \tag{5.6}$$

The constraints on the field equations can be expressed with the trace operator, as in the standard form in (5.1), by converting them into a quadratic format. The real and imaginary parts of the fields can be used to convert complex field expressions into real power patterns, which will result in a quadratic form:

$$\mathbb{F}_{co,i} = \begin{bmatrix}\mathbb{R}(F_{co,i}) \\ \mathbb{I}(F_{co,i})\end{bmatrix} = \begin{bmatrix}\mathbb{R}(\mathbf{a}^H_{co,i}) & -\mathbb{I}(\mathbf{a}^H_{co,i}) \\ \mathbb{I}(\mathbf{a}^H_{co,i}) & \mathbb{R}(\mathbf{a}^H_{co,i})\end{bmatrix}\begin{bmatrix}\mathbb{R}(\mathbf{w}_{co}) \\ \mathbb{I}(\mathbf{w}_{co})\end{bmatrix} = \mathbf{A}_{co,i}\mathbf{w} \tag{5.7}$$

where $\mathbf{A}_{co,i} \in \mathbb{R}^{2\mathrm{x}4N}$, $\mathbf{w} \in \mathbb{R}^{4N\mathrm{x}1}$. (5.7) can be used to express the radiated power in the $i^{th}$ direction:

$$|\mathbb{F}_{co,i}|^2 = \mathbb{F}^T_{co,i}\mathbb{F}_{co,i} = \mathbf{w}^T\mathbf{A}^T_{co,i}\mathbf{A}_{co,i}\mathbf{w} = \mathbf{w}^T\mathbf{Q}_{co,i}\mathbf{w} \tag{5.8}$$

As $\mathbf{Q}_{co,i}$ is a real and symmetric matrix, and $\mathbf{w}$ is real, (5.8) can be expressed through the trace [23]:

$$|\mathbb{F}_{co,i}|^2 = \mathbf{w}^T\mathbf{Q}_{co,i}\mathbf{w} = \mathrm{Tr}(\mathbf{w}^T\mathbf{Q}_{co,i}\mathbf{w}) = \mathrm{Tr}(\mathbf{Q}_{co,i}\mathbf{w}\mathbf{w}^T) = \mathrm{Tr}(\mathbf{Q}_{co,i}\mathbf{W}) \tag{5.9}$$

where $\mathbf{W} \in \mathbb{R}^{4N\mathrm{x}4N}$, which is the optimization variable. All of the constraints, to suppress cross-polarization and side-lobes and shape the beam, will be set using (5.9). In the end of the optimization, $\mathbf{w}$ will be extracted from the optimization variable $\mathbf{W}$; therefore, two constraints must be imposed on $\mathbf{W}$:

- The rank of $\mathbf{W}$ must be forced to be 1, since theoretically $\mathbf{W} = \mathbf{w}\mathbf{w}^T$.
- As $\mathbf{W}$ is real and symmetric, and also has a single positive eigenvalue (due to $\mathbf{W} = \mathbf{w}\mathbf{w}^T$), it must be forced to be a PSD matrix.

The optimization problem with the SDR format and the constraints explained above is as follows:

$$
\begin{aligned}
\min_{\mathbf{W}} \quad & -\operatorname{Tr}(\mathbf{Q}_{co,0}\mathbf{W}) = -\rho \\
\text{s.t.} \quad & \rho \cdot l_i \leq \operatorname{Tr}(\mathbf{Q}_{co,i}\mathbf{W}) \leq \rho \cdot u_i, \quad \forall(\vartheta_i, \phi_i) \in ML \\
& \operatorname{Tr}(\mathbf{Q}_{cr,i}\mathbf{W}) \leq \rho \cdot \frac{u_i + l_i}{2} \cdot \left(10^{\frac{XPL}{20}}\right)^2, \quad \forall(\vartheta_i, \phi_i) \in ML \\
& \operatorname{Tr}(\mathbf{Q}_{co,i}\mathbf{W}) \leq \rho \cdot \left(10^{\frac{SLL_{co}}{20}}\right)^2, \quad \forall(\vartheta_i, \phi_i) \in SL \\
& \operatorname{Tr}(\mathbf{Q}_{cr,i}\mathbf{W}) \leq \rho \cdot \left(10^{\frac{SLL_{cr}}{20}}\right)^2, \quad \forall(\vartheta_i, \phi_i) \in SL \\
& \mathbf{W} \succeq 0 \\
& \operatorname{rank}(\mathbf{W}) = 1
\end{aligned}
\tag{5.10}
$$

From (5.10) it can be seen that the objective function and the first five constraints comply with the standard form of an SDR optimization problem given in (5.1). The first constraint is used to shape the co-polarized field inside the main-lobe, where $u_i$ represents the upper bound of the desired shape and $l_i$ represents the lower bound. The strategy, as seen in many studies, behind beam shaping in PPAAs is to shape the co-polarized component and suppress the cross-polarized component as much as possible. However, that strategy may deteriorate the purity of the polarization at certain regions in the elevation plane. For instance, when a mask with a cosecant decaying main-lobe is considered, the main-lobe of the cross-polarized field also has to decay with a cosecant to ensure that polarization purity is the same at each point inside the main-lobe; if the cross-polarized field is constant, then the polarization purity will deteriorate as the difference between the orthogonal fields will decrease with the decay of the mask. Therefore, the second constraint is set to ensure that the cross-polarized field inside the main-lobe is lower than the mask. The third and fourth constraints are set to suppress the side-lobes of the fields; $\text{SLL}_{co}$ and $\text{SLL}_{cr}$ are squared as the fields are represented by the power patterns (due to the SDR format). Moreover, as explained previously, **W** is constrained to be a PSD matrix, which complies with the standard SDR form in (5.1). The final constraint is set to ensure that **W** resembles the multiplication of two vectors (recall $\mathbf{W}=\mathbf{w}\mathbf{w}^T$) and has only a single and positive eigenvalue. However, enforcing the rank of **W** to be one is not convex and does not comply with the SDR format in (5.1) and cannot be used. A possible way to overcome the rank problem is to minimize the rank of **W** using the objective function, as discussed in [23] and [24]. The strategy explained in [24] is to lower the rank of the matrix by minimizing the trace, as it is known to minimize the sum of the eigenvalues. A good substitute for lowering the rank instead of minimizing the trace is to minimize the so called log-det heuristic: $log\left(det\left(\mathbf{W}+\delta\mathbf{I}\right)\right)$. With the $1^{st}$ order Taylor expansion [24], the log-det heuristic can be represented by the following iterative minimization problem:

$$
\begin{aligned}
\min_{\mathbf{W}^k} \quad & \operatorname{Tr}\left(\left(\mathbf{W}^{k-1} + \delta\mathbf{I}\right)^{-1}\mathbf{W}^k\right) \\
\text{s.t.} \quad & \operatorname{Tr}(\mathbf{Q}_{co,0}\mathbf{W}) = 1 \\
& l_i \leq \operatorname{Tr}(\mathbf{Q}_{co,i}\mathbf{W}) \leq u_i, \quad \forall(\vartheta_i, \phi_i) \in ML \\
& \operatorname{Tr}(\mathbf{Q}_{cr,i}\mathbf{W}) \leq \frac{u_i + l_i}{2} \cdot \left(10^{\frac{XPL}{20}}\right)^2, \quad \forall(\vartheta_i, \phi_i) \in ML \\
& \operatorname{Tr}(\mathbf{Q}_{co,i}\mathbf{W}) \leq \left(10^{\frac{SLL_{co}}{20}}\right)^2, \quad \forall(\vartheta_i, \phi_i) \in SL \\
& \operatorname{Tr}(\mathbf{Q}_{cr,i}\mathbf{W}) \leq \left(10^{\frac{SLL_{cr}}{20}}\right)^2, \quad \forall(\vartheta_i, \phi_i) \in SL \\
& \mathbf{W} \succeq 0
\end{aligned}
\tag{5.11}
$$

The objective function of (5.11) is iteratively minimizing the log-det term linearized by the Taylor approx-

imation, where $\delta$ is a small regularization term ensuring the stability. For the first iteration **W** can be set as the identity matrix: $\mathbf{W}^0 = \mathbf{I}$, which will make the objective function to simply minimize the trace of $\mathbf{W}^k$ in the first iteration. Therefore, objective function starts by minimizing the trace of **W** and the rank of it will be lowered further with the iterations. As the objective function is minimizing the rank, the peak power radiated is normalized to 1 and all of the constraints are re-arranged with respect to it.

Once the **W** is optimized, **w** can be easily obtained. Although the rank of **W** is minimized, there will be more than one non-zero eigenvalues with magnitudes much smaller than the greatest eigenvalue. The effect of non-zero eigenvalues, other than the first one, can be removed by making a rank one approximation: $\mathbf{W}_1 = \sigma_1 \mathbf{u}_1 \mathbf{u}_1^T$, where $\sigma_1$ is the greatest eigenvalue and $\mathbf{u}_1$ is the corresponding eigenvector, which can be obtained through eigenvalue decomposition [23]. Similarly, the excitation vector can be obtained:

$$\hat{\mathbf{w}} = \sqrt{\sigma_1}\mathbf{u}_1 \tag{5.12}$$

The port excitation coefficients can be extracted from (5.12): $\hat{\mathbf{w}} = [\mathbb{R}(\mathbf{w}_H)^T \quad \mathbb{R}(\mathbf{w}_V)^T \quad \mathbb{I}(\mathbf{w}_H)^T \quad \mathbb{I}(\mathbf{w}_V)^T]$ (see (5.6), (5.7)). As the peak radiation power is constrained to be 0 dB, the peak excitation coefficient magnitude is not necessarily one. Once the coefficients are obtained using (5.12), the maximum magnitude can be normalized to 1.

### 5.1.1. Application on Linear Arrays

The synthesis procedure explained above is initially applied to a linear array. The middle column of the 13 by 13 planar array explained in Section 2.5 is used. AEPs of elements from the middle column are used through the optimization process; therefore, all mutual coupling effects are included ($\mathbf{a}_{HH} \neq \mathbf{1}, \quad \mathbf{a}_{VV} \neq \mathbf{1}, \quad \mathbf{a}_{HV} \neq \mathbf{0}, \quad \mathbf{a}_{VH} \neq \mathbf{0}$) in the optimization. The shaping is performed on the $u = 0$ plane; two different masks with cosecant-decaying and flat-top main-lobes are tried to be synthesized with the linear array. It should be noted that with the dual-polarized architecture, any polarization state can be selected as co-polarization and shaped, while suppressing the orthogonal cross-polarization. However, it is observed that with the low-cost architecture, unlike solely suppressing the cross-polarization, shaping criteria cannot be met for H and V while suppressing the cross-polarization, as both ports have to be excited with the same amplitude. In the previous chapters, the purpose with the low-cost architecture was to suppress the cross-polarized field and the side-lobes of both fields, which were shown to be achievable mainly by the phases with a slight loss in EIRP. However, for pattern synthesis, the amplitude applied to each port also plays an important role. Therefore, in this chapter, the examined polarization states are: 45-slant ($\varphi = 45, \eta = 0$), 135-slant ($\varphi = 135, \eta = 0$), and LHCP ($\varphi = 45, \eta = 90$). Ideally, to synthesize any of these polarizations, both ports would be excited with equal amplitude, which can ease the problem of joint pattern and polarization synthesis with the low-cost architecture.

For synthesizing a cosecant-decaying mask, the goal is to achieve a $csc(\theta)$ decay for the co-polarized field with a maximum ripple size of $\pm$ 0.8 dB over the main-lobe region ($0.2 \leq v \leq 0.47$), cross-polarized field is constrained to be $45$ dB lower than the mask over the main-lobe, and side-lobe levels ($v \leq 0, v \geq 0.56$) for both fields are constrained to be lower than $-17$ dB. For the flat-top mask, a ripple size of $\pm$ 0.8 dB over the main-lobe region ($-0.44 \leq v \leq 0.44$) is allowed, cross-polarized field is constrained to be $45$ dB lower than the mask over the main-lobe, and side-lobe levels ($v \leq -0.72, v \geq 0.72$) for both fields are constrained to be lower than $-17$ dB.

To show the necessity for the constraining of cross-polarized field (in addition to the shaping of co-polarized field) on polarization purity, initially, the optimization for the synthesis of a cosecant shaped

beam is performed without the cross-polarization shaping constraints (the second inequality constraint is removed from (5.11)). Fig.5.1 demonstrates the synthesis of a cosecant shaped beam with 45-Slant polarization, without enforcing any constraints on the shape of cross-polarization. It can be seen that although the co-polarized field is shaped finely, polarization purity is lower than $20$ dB inside the main-lobe, as cross-polarized field is not constrained with respect to the mask shape.

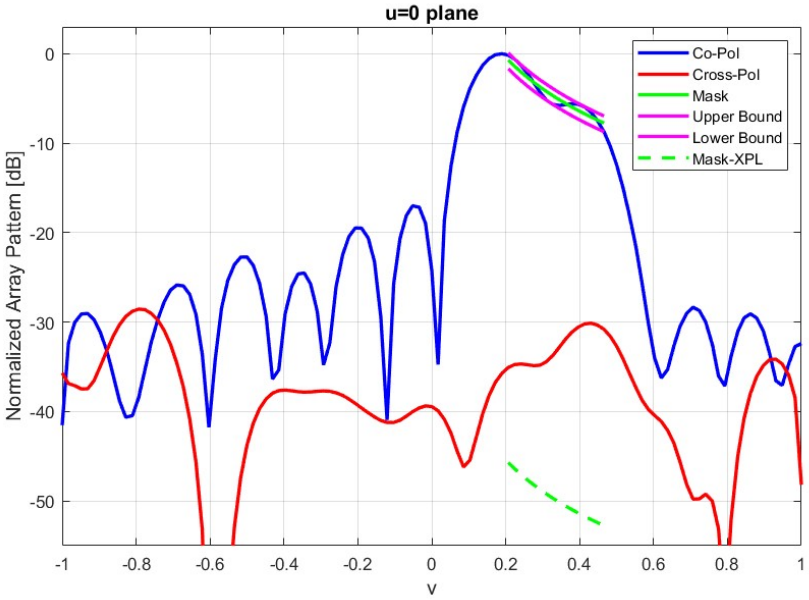


**Figure 5.1:** Array radiation pattern in the $u = 0$ plane (normalized, in dB) for a cosecant decaying mask (without cross-polarization shaping constraints), Co-pol: 45-Slant $(\varphi = 45, \eta = 0)$.

After motivating the need for the constraining of the cross-polarized field, the optimization in (5.11) is performed. The polarimetric performance of the dual-polarized architecture is shown in Table 5.1 for the two different masks. Moreover, for completeness, several array patterns are shown in Fig. 5.2.

**Table 5.1:** Polarimetric performance of the fully-polarized linear array with pattern synthesis

| **Mask** | $(\varphi, \eta)$ | **Pin** [W] | **Max Ripple** [dB] | **XPL** [dB] | **SLL**$_{co}$ [dB] | **SLL**$_{cr}$[dB] |
|---|---|---|---|---|---|---|
| **csc**$(\theta)$ | (45,0) | 5.01 | 0.97 | -44.04 | -17.00 | -21.93 |
| | (135,0) | 5.41 | 1.03 | -41.99 | -17.00 | -33.61 |
| | (45,90) | 5.33 | 0.86 | -43.11 | -17.07 | -26.75 |
| **Flat-Top** | (45,0) | 2.39 | 0.72 | -42.74 | -16.99 | -22.80 |
| | (135,0) | 2.35 | 1.31 | -41.07 | -24.21 | -30.33 |
| | (45,90) | 3.53 | 6.06* | -41.24 | -18.43 | -21.86 |

* *Although optimization is performed for this case as well, shaping and polarization requirements could not be met jointly. It is observed that the main-lobe is narrowing down considerably, resulting in high ripple at the edge of the main-lobe. This can be improved by relaxing the polarization requirements or narrowing down the imposed mask.*

From Fig. 5.2 it can be seen that both masks have been successfully synthesized when the co-polarization is 45-slant. Moreover, when the cosecant decaying mask is considered, it can be seen that the cross-polarization inside the main-lobe region is decaying with the cosecant rate, ensuring the polarization purity. When the polarimetric performance of the algorithm is examined through Table 5.1, it can be seen that the SLL criteria have been met for each polarization and mask type. Unlike the previous chapters, the XPL metric is measured as the difference between the co- and cross-polarization inside the main-lobe, since the main-lobe pattern is not constant. Although the XPL criterion of $-45$

dB could not be fully met, it is simulated to be less than $-41$ dB in the worst case, which is sufficient. Moreover, in the examined linear array with 13 elements (where the maximum input power is $13$ W), the input power levels appeared to be low, which was expected since the algorithm applied a considerable taper for shaping. Moreover, other than the synthesis of flat-top mask with LHCP being the co-polarization, the ripple size criterion is met with slight deterioration. However, for LHCP synthesis with a flat-top beam, there appeared to be a considerable deterioration, which is possibly due to the angular region for the cross-polarization to be suppressed being wide.

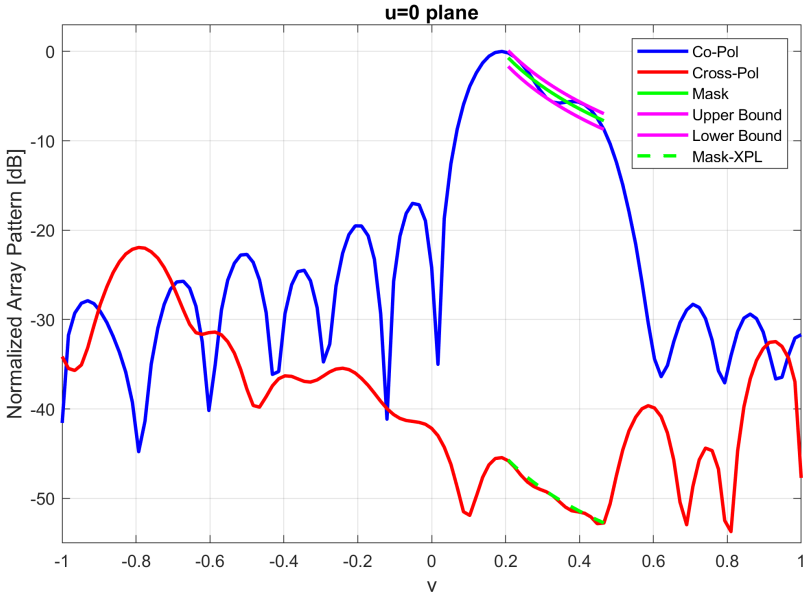


**(a)** Cosecant decaying mask

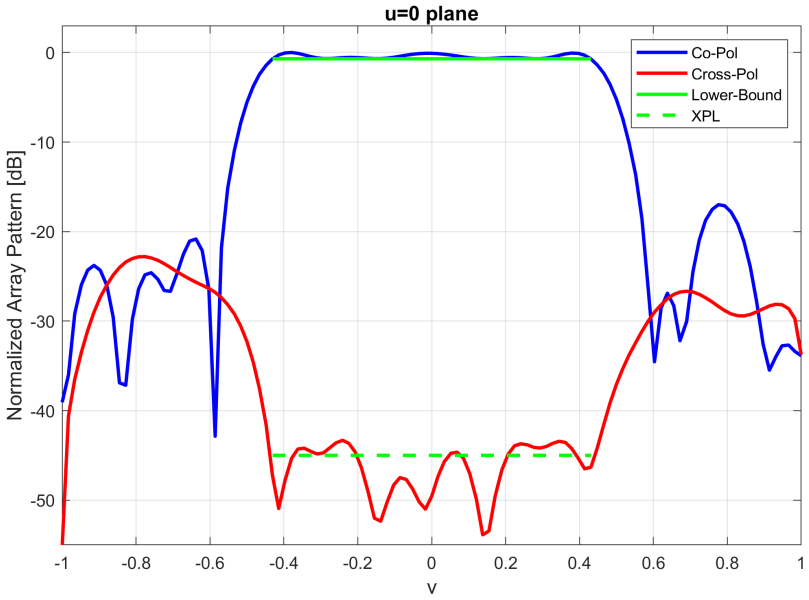


**(b)** Flat-top mask

**Figure 5.2:** Array radiation patterns in the $u = 0$ plane (normalized, in dB) for a cosecant decaying mask and a flat-top mask, Co-Pol: 45-Slant ($\varphi = 45, \eta = 0$).

### 5.1.2. Application on Planar Arrays

The shaping can be applied to planar arrays, where the pattern shaping can be performed on the elevation plane, and the shaped pattern can be steered on azimuth. The strategy is to apply the same set of coefficients as those obtained in the previous section to each column. Moreover, steering on azimuth can be simply performed by applying progressive phase shifts to each column of the array. The required phase shift to steer the beam to a plane defined by $u = u_0$ can be found through:

$$\beta_n = e^{-j\frac{2\pi}{\lambda}\cdot n\cdot d\cdot u_0} \tag{5.13}$$

where $n$ represents the $n^{th}$ column of the array, $\lambda$ is the wavelength, and $d$ is the uniform spacing between the columns of the array. The strategy is applied to the 13 by 13 planar array, using the coefficients obtained for the middle column of the array in Section 5.1.1. Radiation at $u_0 = 0$ and $u_0 = 0.26$ on azimuth are considered for the two masks:

**Table 5.2:** Polarimetric performance of the fully-polarized planar array with pattern synthesis

| **Mask** | **Direction** | $(\varphi, \eta)$ | **Pin** [W] | **Max Ripple**[dB] | **XPL**[dB] | **SLL**$_{co}$[dB] | **SLL**$_{cr}$[dB] |
|---|---|---|---|---|---|---|---|
| **csc**($\theta$) | **Broadside**($u_0 = 0$) | (45,0) | 65.17 | 0.96 | -30.62 | -13.51 | -22.86 |
| | | (135,0) | 70.28 | 1.03 | -42.51 | -13.45 | -34.84 |
| | | (45,90) | 69.29 | 0.84 | -33.05 | -13.56 | -26.27 |
| | **Steered**($u_0 = 0.26$) | (45,0) | 65.17 | 1.04 | -25.97 | -13.13 | -23.19 |
| | | (135,0) | 70.28 | 1.02 | -37.84 | -13.10 | -34.34 |
| | | (45,90) | 69.29 | 0.95 | -31.72 | -13.12 | -25.81 |
| **Flat-top** | **Broadside**($u_0 = 0$) | (45,0) | 31.13 | 0.92 | -35.13 | -13.52 | -22.86 |
| | | (135,0) | 30.59 | 1.25 | -36.15 | -13.51 | -28.51 |
| | | (45,90) | 45.95 | 6.28* | -29.92 | -13.55 | -21.85 |
| | **Steered** ($u_0 = 0.26$) | (45,0) | 31.13 | 0.95 | -28.81 | -13.12 | -23.48 |
| | | (135,0) | 30.59 | 1.34 | -31.48 | -13.10 | -30.09 |
| | | (45,90) | 45.95 | 6.34* | -27.35 | -13.09 | -22.65 |

* *These values are obtained through the poor optimization mentioned in Table 5.1. They can be improved by improving the optimization performed in the first stage.*

Table 5.2 shows the polarimetric performance of the planar array for two different masks and radiation directions. The maximum ripple and XPL metrics are obtained from the cut-plane on azimuth, whereas SLL metrics are obtained from the entire side-lobe region. It can be seen that for both masks, the maximum ripple deteriorated slightly as the beam is steered, which is negligible. Moreover, SLL$_{cr}$ is maintained well below $-17$ dB in each case. Although the beam shape is maintained in general, there is a considerable deterioration in XPL and SLL$_{co}$. Despite XPL did not exceed $-30$ dB for broadside radiation, it is simulated to be around $-27$ dB in several cases of steered radiation. In addition to XPL, the SLL$_{co}$ deteriorated considerably to $-13$ dB in each case. The reason behind the deterioration in XPL and SLL$_{co}$ is that the optimization is performed only with respect to the middle column of the planar array, and the coupling effects between the columns are not included in the optimization problem. Moreover, no optimization is performed for the steered radiation case. To overcome this problem, a desired mask on the entire u-v grid (instead of a single plane) could have been defined, and all antennas could have been included in the optimization problem (5.11). However, defining a mask on the entire u-v grid is not trivial, and including each antenna in the optimization problem would result in a **W** matrix with 456976 ($(4N)^2$) elements to be optimized, resulting in a huge computational burden. For completeness, several array radiation patterns are shown in Fig. 5.3.

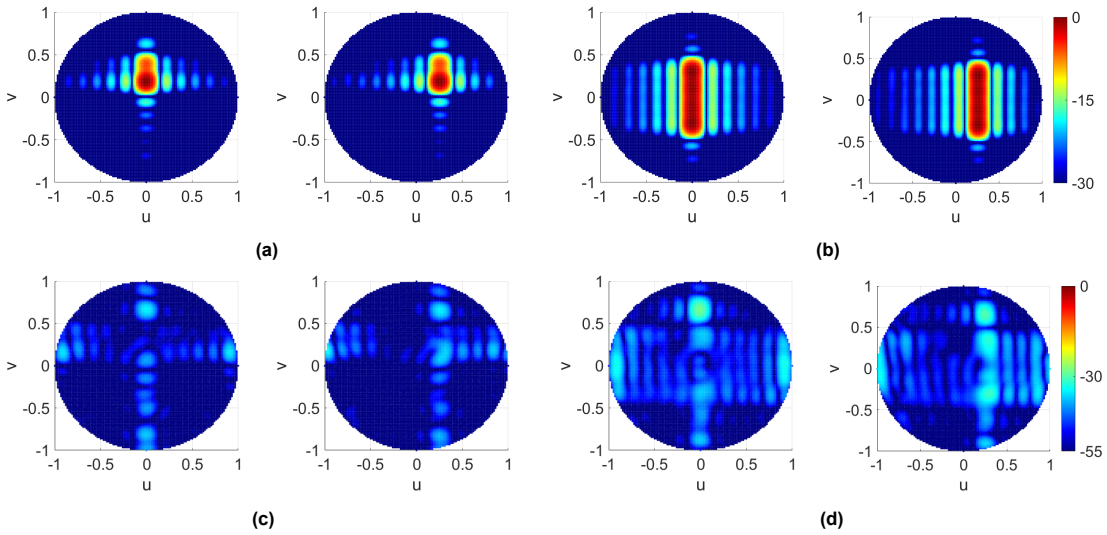


**Figure 5.3:** Array radiation patterns in the $uv$-plane (normalized, in dB) with the dual-polarized architecture for a broadside [$u_0 = 0$] and a scanned [$u_0 = 0.26$] beam: (a) co-pol.: ($\varphi = 135°, \eta = 0°$) - csc($\theta$) mask, (b) co-pol.: ($\varphi = 135°, \eta = 0°$) - Flat-top mask, (c) cross-pol.: ($\varphi = 135°, \eta = 0°$) - csc($\theta$) mask, (d) cross-pol.: ($\varphi = 135°, \eta = 0°$) - Flat-top mask

## 5.2. Pattern&Polarization Synthesis with the Low-Cost Architecture

A similar polarimetric pattern synthesis procedure can be performed for the low-cost architecture in Fig. 1.2b, where the ports of the same patch must be excited with the same amplitude. The optimization problem in (5.11) can be adjusted for the low-cost architecture:

$$
\begin{aligned}
\min_{\mathbf{W}^k} \quad & \mathrm{Tr}\left(\left(\mathbf{W}^{k-1} + \delta \mathbf{I}\right)^{-1} \mathbf{W}^k\right) \\
\text{s.t.} \quad & \mathrm{Tr}(\mathbf{Q}_{co,0}\mathbf{W}) = 1 \\
& l_i \leq \mathrm{Tr}(\mathbf{Q}_{co,i}\mathbf{W}) \leq u_i, \quad \forall(\vartheta_i, \phi_i) \in ML \\
& \mathrm{Tr}(\mathbf{Q}_{cr,i}\mathbf{W}) \leq \frac{u_i + l_i}{2} \cdot \left(10^{\frac{XPL}{20}}\right)^2, \quad \forall(\vartheta_i, \phi_i) \in ML \\
& \mathrm{Tr}(\mathbf{Q}_{co,i}\mathbf{W}) \leq \left(10^{\frac{SLL_{co}}{20}}\right)^2, \quad \forall(\vartheta_i, \phi_i) \in SL \\
& \mathrm{Tr}(\mathbf{Q}_{cr,i}\mathbf{W}) \leq \left(10^{\frac{SLL_{cr}}{20}}\right)^2, \quad \forall(\vartheta_i, \phi_i) \in SL \\
& \mathbf{W} \succeq 0 \\
& \mathrm{Tr}(\mathbf{Q}_{n1}\mathbf{W}) = \mathrm{Tr}(\mathbf{Q}_{n2}\mathbf{W}), \quad n = 1, \cdots, N_x
\end{aligned}
\tag{5.14}
$$

where $N_x$ represents the number of antennas in a single column of the planar array, and $\mathbf{Q}_{n1}$, $\mathbf{Q}_{n2}$ are:

$$
\mathbf{Q}_{n1}(i,i) = \begin{cases} 1, & \text{if } i = n \\ 1, & \text{if } i = n + 2N_x \\ 0, & \text{else} \end{cases} \qquad \mathbf{Q}_{n2}(i,i) = \begin{cases} 1, & \text{if } i = n + N_x \\ 1, & \text{if } i = n + 3N_x \\ 0, & \text{else} \end{cases} \tag{5.15}
$$

The last constraint in (5.14) forces the ports of the same patch to be excited with the same amplitude.

Since $\mathbf{Q}_{n1}$ and $\mathbf{Q}_{n2}$ are diagonal matrices, and $\text{diag}(\mathbf{W}) = [\mathbb{R}(\mathbf{w}_H)^2 \quad \mathbb{R}(\mathbf{w}_V)^2 \quad \mathbb{I}(\mathbf{w}_H)^2 \quad \mathbb{I}(\mathbf{w}_V)^2]$:

$$\mathbb{R}(w_{H,n})^2 + \mathbb{I}(w_{H,n})^2 = \mathbb{R}(w_{V,n})^2 + \mathbb{I}(w_{V,n})^2, \qquad n = 1, \cdots, N_x \tag{5.16}$$

forcing the port coefficients of an element to differ solely by a phase. It should be noted that, unlike the previous chapters, the quantization of the phases is not discussed.

### 5.2.1. Application on Linear Arrays

As in Section 5.1.1, the algorithm is initially performed on the middle column of the planar array explained in Section 2.5. A cosecant decaying mask and a flat-top mask with the properties explained in Section 5.1.1 are tried to be synthesized for the same polarization states.

**Table 5.3:** Polarimetric performance of the low-cost linear array with pattern synthesis

| **Mask** | $(\varphi, \eta)$ | **Pin** [W] | **Max Ripple**[dB] | **XPL**[dB] | **SLL**$_{co}$[dB] | **SLL**$_{cr}$[dB] |
|---|---|---|---|---|---|---|
| **csc($\theta$)** | (45,0) | 5.44 | 0.98 | -44.28 | -17.00 | -28.58 |
| | (135,0) | 5.28 | 1.03 | -44.46 | -16.99 | -30.61 |
| | (45,90) | 5.36 | 1.41 | -37.02 | -17.22 | -25.76 |
| **Flat-top** | (45,0) | 2.25 | 1.13 | -32.12 | -17.64 | -29.39 |
| | (135,0) | 2.35 | 1.41 | -37.89 | -24.26 | -31.01 |
| | (45,90) | 2.79 | 16.70* | -20.64 | -17.77 | -19.88 |

* *Although optimization is performed for this case as well, shaping and polarization requirements could not be met jointly. It is observed that the main-lobe is narrowing down considerably, resulting in high ripple at the edge of the main-lobe. This can be improved by relaxing the polarization requirements or narrowing down the imposed mask.*

Table 5.3 shows the polarimetric performance of the 13 element linear array with a low-cost architecture. Compared to the dual-polarized architecture (see Table 5.1), low-cost architecture synthesized a cosecant decaying mask with almost no deterioration using the slant polarizations as co-polarization (see Fig. 5.4a); when LHCP is considered, a slight increase in the ripple size has occurred and a considerable loss in XPL. When the flat-top mask is considered, a slight increase in the ripple size occurred for $45, 135$-slant, but XPL deteriorated considerably (see Fig. 5.4b). Although there is a considerable loss in XPL, it did not exceed $-32$ dB, which is sufficient for practical applications. However, the ripple size and XPL have considerably deteriorated when synthesizing LHCP with a flat-top shape. The reason for a ripple size of $16.7$ dB is that the main-lobe considerably narrowed compared to the targeted width, resulting in a huge difference at the edge of the targeted region. Moreover, XPL is simulated to be around $-21$ dB due to narrowing of the main-lobe, where co-polarization is significantly lower than expected. The deterioration in the first five cases in Table 5.3 was expected due to the lack of freedom of full amplitude control. Moreover, as explained, the unexpected deterioration in the last case is due main-lobe narrowing and co-polarization intensity lowering at the edge of the targeted region.

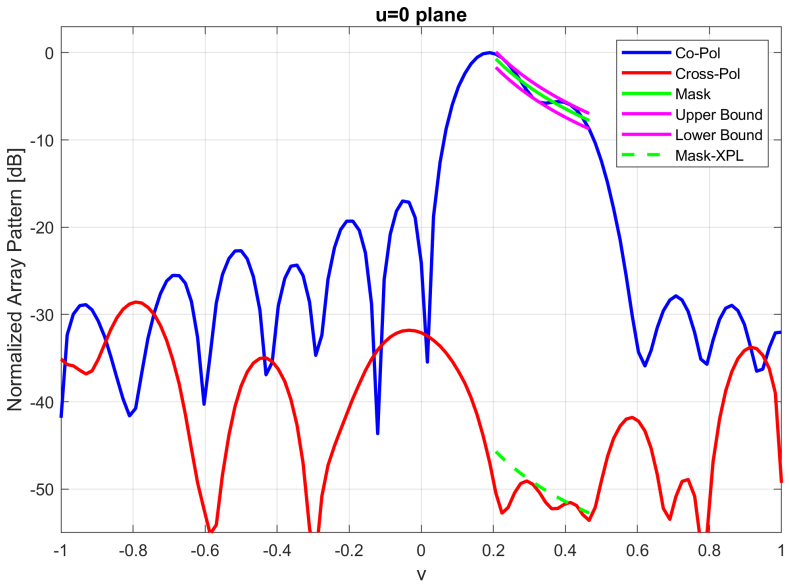


**(a)** Cosecant decaying mask

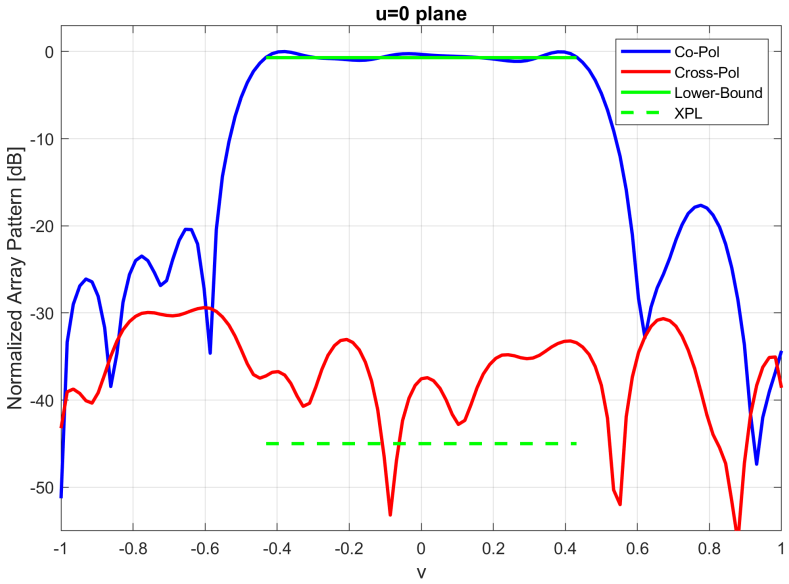


**(b)** Flat-top mask

**Figure 5.4:** Array radiation patterns in the $u = 0$ plane (normalized, in dB) for a cosecant decaying mask and a flat-top mask, Co-Pol: 45-Slant ($\varphi = 45, \eta = 0$).

### 5.2.2. Application on Planar Arrays

A similar procedure to that in Section 5.1.2 is performed to extend a low-cost linear array to a planar array whose polarimetric performance is shown in Table 5.4. As in Section 5.1.2, the maximum ripple metric remained at the same level as in the linear array case, $\text{SLL}_{cr}$ did not exceed $-20$ dB, and $\text{SLL}_{co}$ deteriorated to $-13$ dB level. As expected, XPL levels considerably deteriorated, which was the case in the fully-polarized planar array as well. As explained, this problem could be solved by jointly optimizing each excitation coefficient in the array; however, this will result in a huge computational burden. For completeness, several array radiation patterns are shown in Fig. 5.5.

**Table 5.4:** Polarimetric performance of the fully-polarized planar array with pattern synthesis

| Mask | Direction | $(\varphi, \eta)$ | Pin [W] | Max Ripple[dB] | XPL[dB] | SLL$_{co}$[dB] | SLL$_{cr}$[dB] |
|---|---|---|---|---|---|---|---|
| csc($\theta$) | Broadside($u_0 = 0$) | (45,0) | 70.67 | 0.95 | -30.04 | -13.52 | -31.21 |
| | | (135,0) | 68.69 | 1.03 | -35.78 | -13.45 | -31.04 |
| | | (45,90) | 69.72 | 1.23 | -33.85 | -13.57 | -26.30 |
| | Steered($u_0 = 0.26$) | (45,0) | 70.67 | 1.03 | -25.70 | -13.14 | -30.81 |
| | | (135,0) | 68.69 | 1.03 | -37.63 | -13.09 | -31.29 |
| | | (45,90) | 69.72 | 1.13 | -28.81 | -13.14 | -26.54 |
| Flat-top | Broadside($u_0 = 0$) | (45,0) | 29.20 | 1.25 | -31.04 | -13.48 | -29.13 |
| | | (135,0) | 30.55 | 1.34 | -32.46 | -13.50 | -31.71 |
| | | (45,90) | 36.32 | 16.60* | -21.71 | -13.54 | -19.90 |
| | Steered ($u_0 = 0.26$) | (45,0) | 29.20 | 1.25 | -27.79 | -13.10 | -28.17 |
| | | (135,0) | 30.55 | 1.43 | -30.91 | -13.09 | -32.19 |
| | | (45,90) | 36.32 | 16.28* | -21.15 | -13.15 | -19.76 |

* *These values are obtained through the poor optimization mentioned in Table 5.3. They can be improved by improving the optimization performed in the first stage.*

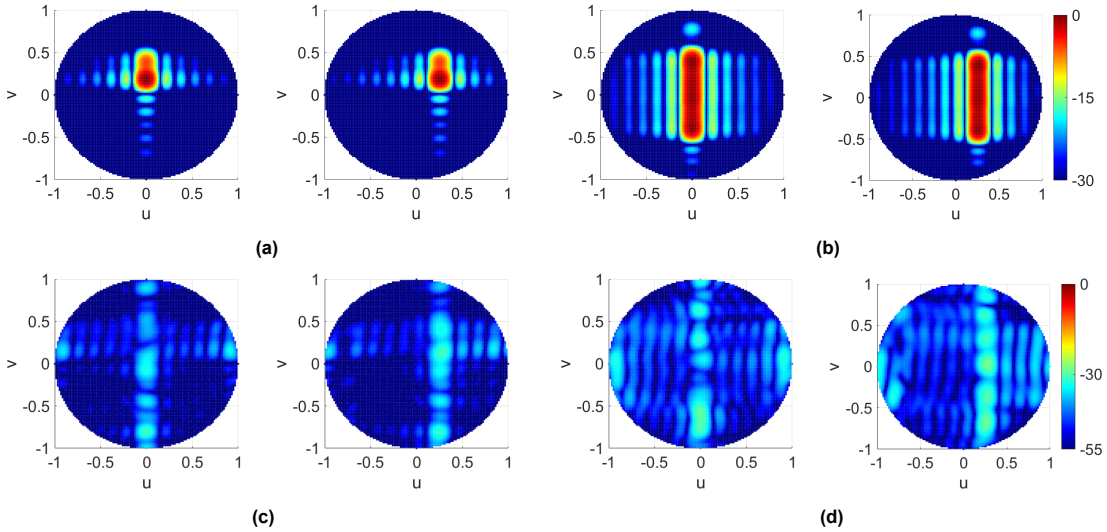


**Figure 5.5:** Array radiation patterns in the $uv$-plane (normalized, in dB) with the dual-polarized architecture for a broadside [$u_0 = 0$] and a scanned [$u_0 = 0.26$] beam: (a) co-pol.: ($\varphi = 45°, \eta = 0°$) - csc($\theta$) mask, (b) co-pol.: ($\varphi = 45°, \eta = 0°$) - Flat-top mask, (c) cross-pol.: ($\varphi = 45°, \eta = 0°$) - csc($\theta$) mask, (d) cross-pol.: ($\varphi = 45°, \eta = 0°$) - Flat-top mask

## 5.3. Intermediate Conclusions

In this chapter, joint pattern and polarization synthesis are performed for three polarization states: 45, 135-slant, and LHCP. A cosecant decaying pattern and a flat-top pattern are synthesized while meeting the polarization requirements. Synthesis is initially performed for the dual-polarized architecture. As the shaping requirements are not convex, the SDR technique is used. Moreover, in addition to the shaping and side-lobe constraints, the cross-polarization is constrained to be $45$ dB lower than the mask. Unlike the previous chapters, the cross-polarized field is also shaped as the magnitude of the co-polarized field varies inside the main-lobe, which would deteriorate the polarization purity if the cross-polarization was not suppressed accordingly. Afterwards, optimization is performed for the low-cost architecture in Fig. 1.2b (with variable phase shifters) by slightly adjusting the SDR algorithm. It must be noted that pattern shaping is performed on the elevation plane, and the shaped pattern is steered on the azimuth by simply applying progressive phase shifts to each column. As there was no optimization for the steered cases, side-lobe levels of the co-polarized field increased by $4$ dB. All optimizations are performed considering the electromagnetic effects, where the algorithms are shown to be robust against coupling effects.

# 6

# Conclusion and Recommendations for Future Work

## 6.1. Conclusion

The beamforming capabilities and performance of a PPAA profoundly depend on its RF architecture, where different architectures result in different optimization problems for the complex beamforming coefficients. It is known that a conventional dual-polarized architecture can synthesize any polarization with excellent performance, since there is full amplitude and phase control at each port. Although there is no concern with the performance of the dual-polarized architecture, it requires a substantial number of RF components to provide full amplitude and phase control at each port. A recent study by [8] addresses this problem by proposing a low-cost architecture in which both ports of an antenna element are excited with the same amplitude but with a different phase. The optimization strategy proposed by [8] for the low-cost architecture is shown to result in decent performance for the synthesis of H and V, but poor performance for the synthesis of any other polarization state.

The poor performance of the low-cost architecture for any other third polarization state develops the first novelty of this thesis: re-optimizing the polarization states of an element, defined by the fixed phase shift between its ports, such that the low-cost PPAA attains an acceptable polarimetric performance for three polarizations. Two new strategies are presented in Section 3.2: PA and CPS. Once the continuous phase shifts are obtained through the proposed methods, the phases are quantized with two different methods: regular with a distance function and Lloyd-Max quantization. The proposed PA and CPS methods indicated that the performance of the arbitrary third polarization, which was chosen to be LHCP, can be improved compared to [8] with reasonable deterioration in H and V. The quantization of PA and CPS with both methods showed that the Lloyd-Max quantized phases result in a lower deterioration in H and V, but also a lower improvement in LHCP, compared to [8]. This was expected since Lloyd-Max computes discrete levels based on the continuous phases. When PA and CPS are compared, it is observed that CPS largely exceeded the performance of PA, especially for LHCP synthesis. As Lloyd-Max quantized CPS output resulted in minimal loss in H and V, and significantly improved the LHCP, it is observed to provide the finest element polarization states. The stability of the proposed CPS algorithm against mutual coupling is demonstrated with full-wave simulations.

An important way to reduce the cost and complexity of a phased array is to decompose it into subarrays. Unlike regular phased arrays, the implementation of subarrayed PPAAs is not widely discussed in the literature, leading to the second novelty of the thesis. Since the elements of a PPAA have to be excited by two orthogonal feeds, RF architectures employing subarrays are not commonly implemented in PPAAs. However, it is shown in [8], and extended in this work, that the two feeds of an element can be coupled into a single RF chain through a fixed phase shifter. Once the feeds of an element are connected, neighboring elements can be subarrayed using a Wilkinson power divider. Although subarray size, shape, and orientation are all widely discussed optimization parameters in the literature for phased arrays, it is assumed that subarrays consist of two elements that can be stacked either horizontally or vertically. In other words, the tiling of the array surface into subarrays with two elements and the corresponding excitation coefficients for the tiles are optimized. Initially, optimizations are performed for the classical subarray architecture, where the antennas in the same subarray are excited with the same amplitude and phase. It is shown that the polarimetric performance of PPAA significantly degrades for synthesizing V and LHCP, and for steered radiation. To provide more degrees of freedom to subarrayed PPAA and minimize the deterioration compared to a regular PPAA, a new RF architecture and a corresponding optimization strategy are proposed: GSPD architecture, where elements in the same subarray are excited with the same amplitude but with a different phase. Initially, optimization of tiles and the beamforming weights is performed to make the array synthesize H and V with high performance, to show that the cost of the low-cost PPAA in [8] could be even reduced further. It is shown that with a slight loss in EIRP and almost no deterioration from the polarization purity and SLL criteria, the low-cost PPAA in [8] can be subarrayed. Moreover, it is realized that the excitation amplitudes almost remained the same for the synthesis of different polarizations and steering directions; therefore, variable gain amplifiers in GSPD are replaced with fixed gain amplifiers: FGPD architecture, which reduced the cost of the PPAA even further. It is shown that EIRP levels remain the same, but polarization purity considerably deteriorates for the steered radiation. Since the polarization purity is simulated to be around $35$ dB, the FGPD architecture can indeed be employed. Furthermore, the GSPD architecture is extended for the synthesis of LHCP using the previously obtained polarization states in Fig. 3.4d (output of CPS-Lloyd Max). It is observed that EIRP levels have slightly decreased, and polarization purity has deteriorated to $40$ dB, which is still acceptable.

Finally, polarization and pattern are jointly synthesized for the fully-polarized and low-cost PPAA. A cosecant and a flat-top mask are synthesized with different polarizations. Although there are some studies in the literature discussing joint polarization and pattern synthesis, to the best of the authors' knowledge, suppression of cross-polarized field with respect to the shape of the mask is not considered. As explained in Chapter 5, in addition to the co-polarized field, the cross-polarized field also has to be constrained to maintain the purity of the polarization, which is another novelty of the thesis. It is shown that the proposed method can meet the pattern shape and the polarization purity criteria, both for conventional and low-cost PPAA. Moreover, for both cases, the pattern shaping is performed on the elevation plane, and steering is performed on the azimuthal plane. Full-wave simulations show that the proposed algorithm can jointly synthesize pattern and polarization with linear arrays while meeting the constraints; however, the side-lobe levels rise when steering is performed with planar arrays, as there is no optimization.

## 6.2. Recommendations for Future Work

As PPAAs become more prevalent and larger in size, cutting-edge low-cost RF architectures will be studied and used in end products more frequently. Furthermore, PPAAs with extended beamforming capabilities in terms of polarization and pattern synthesis will be needed. This thesis attempted to ad-

dress these points with low-cost solutions, and several ensuing future discussion topics are as follows:

1. In Section 3.2, two novel optimization strategies are presented to extend the capability of the low-cost architecture to three polarizations. However, since the problem is not convex, a sequential approach is preferred for optimization. The element polarization states and beamforming weights could have been optimized simultaneously using a different strategy, possibly resulting in a superior polarimetric performance for the examined polarization states.
2. Throughout the thesis, all the nonlinearities related to RF components and feeding circuitry are neglected and not included in optimization. However, in a real setup, Wilkson power dividers would be used to split the power between ports, whose coupling effects must also be included in optimization. Moreover, beamformer ICs would be used in a real setup to provide the required amplitude and phase, which might also require to be modeled and calibrated, as the amplitude and phase may couple depending on the frequency.
3. In Chapter 4, different subarrayed RF architectures and optimization strategies are explored. For each case, subarrays are assumed to consist of two elements, either stacked horizontally or vertically. By examining different subarray sizes, shapes, and orientations, an array with a lower cost or superior polarimetric performance can be obtained.
4. In Chapter 5, the joint pattern and polarization synthesis for conventional and low-cost PPAAs is considered. Instead of performing the optimization for a linear array and then extending it to a planar array, which is shown to deteriorate the performance, the beamforming coefficients could have been directly obtained for a planar array. As this would require all elements to be considered in the optimization problem, a different strategy than using SDR is necessary. Moreover, the desired mask has to be defined over the entire grid.
5. In Chapter 5, it is noticed that the algorithm applies a considerable taper on the weights to meet the polarization and shaping requirements, which reduces the input power of the array and the range of the PPAA. A possible way to overcome this could be to impose a lower bound constraint on the amplitude of beamforming weights. However, since that constraint is not convex, it is not implemented in this thesis. Through different optimization techniques, input power can be included in optimization along with other constraints.

# References


[1] Alexander V Ryzhkov and Dušan S Zrnić. *Radar polarimetry for weather observations*. Vol. 486. Springer, 2019.

[2] GC McCormick. “On the completeness of polarization diversity measurements”. In: *Radio science* 24.4 (1989), pp. 511–518.

[3] V. Santalla and Y.M.M. Antar. “A comparison between different polarimetric measurement schemes”. In: *IEEE Transactions on Geoscience and Remote Sensing* 40.5 (2002), pp. 1007–1017.

[4] V. Santalla del Rio. “Least Squares Estimation of Doppler and Polarimetric Parameters for Weather Targets”. In: *IEEE Transactions on Geoscience and Remote Sensing* 45.11 (2007), pp. 3760–3772.

[5] Verónica Santalla del Río, José Manuel Pidre Mosquera, and María Vera-Isasa. “3-Pol Polarimetric Weather Measurements With Agile-Beam Phased-Array Radars”. In: *IEEE Transactions on Geoscience and Remote Sensing* 52.9 (2014), pp. 5783–5789.

[6] Michael R Andrews, Partha P Mitra, and Robert DeCarvalho. “Tripling the capacity of wireless communications using electromagnetic polarization”. In: *Nature* 409.6818 (2001), pp. 316–318.

[7] Abdurrahman H. Aljuhani et al. “A 256-Element Ku-Band Polarization Agile SATCOM Receive Phased Array With Wide-Angle Scanning and High Polarization Purity”. In: *IEEE Transactions on Microwave Theory and Techniques* 69.5 (2021), pp. 2609–2628. DOI: 10.1109/TMTT.2021.3056439.

[8] Jian Zhou et al. “Polarization-Reconfigurable Phased Array Architecture With Optimally Polarized Elements”. In: *IEEE Transactions on Antennas and Propagation* 73.1 (2025), pp. 201–215.

[9] Yanhui Liu et al. “Linearly Polarized Shaped Power Pattern Synthesis With Sidelobe and Cross-Polarization Control by Using Semidefinite Relaxation”. In: *IEEE Transactions on Antennas and Propagation* 66.6 (2018), pp. 3207–3212. DOI: 10.1109/TAP.2018.2816782.

[10] Shu-Lin Chen et al. “Generalized 2-D Numerical Pattern Synthesis Algorithm for Low Cross Polarization and Low Sidelobe Synthesis”. In: *IEEE Antennas and Wireless Propagation Letters* 16 (2017), pp. 2578–2581. DOI: 10.1109/LAWP.2017.2734841.

[11] Yanhui Liu et al. “Synthesizing Shaped Power Patterns for Linear and Planar Antenna Arrays Including Mutual Coupling by Refined Joint Rotation/Phase Optimization”. In: *IEEE Transactions on Antennas and Propagation* 68.6 (2020), pp. 4648–4657. DOI: 10.1109/TAP.2020.2975277.

[12] Benjamin Fuchs and Jean Jacques Fuchs. “Optimal Polarization Synthesis of Arbitrary Arrays With Focused Power Pattern”. In: *IEEE Transactions on Antennas and Propagation* 59.12 (2011), pp. 4512–4519. DOI: 10.1109/TAP.2011.2165492.

[13] Yufeng Ding et al. “Polarization Synthesis via Sequential Convex Optimizations”. In: *IEEE Antennas and Wireless Propagation Letters* 23.11 (2024), pp. 3516–3520. DOI: 10.1109/LAWP.2024.3413683.

[14] Benjamin Fuchs. “Polarization synthesis of arbitrary arrays with shaped beam pattern”. In: *2013 IEEE International Symposium on Phased Array Systems and Technology*. 2013, pp. 689–692. DOI: 10.1109/ARRAY.2013.6731913.

[15] Wei Zhang. “Optimal Synthesis of Array Focused Power Pattern With Arbitrary Polarization and Low Sidelobe Based on Nullspace”. In: *IEEE Transactions on Antennas and Propagation* 72.7 (2024), pp. 5714–5723. DOI: 10.1109/TAP.2024.3411690.

[16] David Schvartzman et al. “Enhanced Weather Surveillance Capabilities With Multiple Simultaneous Transmit Beams”. In: *IEEE Transactions on Radar Systems* 3 (2025), pp. 272–289. ISSN: 2832-7357. DOI: 10.1109/TRS.2025.3527882.

[17] Stephen Boyd and Lieven Vandenberghe. *Convex Optimization*. Cambridge University Press, 2004.

[18] Benjamin Fuchs and Jean Jacques Fuchs. “Optimal Narrow Beam Low Sidelobe Synthesis for Arbitrary Arrays”. In: *IEEE Transactions on Antennas and Propagation* 58.6 (2010), pp. 2130–2135. DOI: 10.1109/TAP.2010.2046863.

[19] Inc. CVX Research. *CVX: Matlab Software for Disciplined Convex Programming, version 2.0*. https://cvxr.com/cvx. Aug. 2012.

[20] Yan Li, Yu Gong, and Shaoqiu Xiao. “Synthesis of Modular Subarrayed Phased-Array With Shaped-Beams by Means of Sequential Convex Optimization”. In: *IEEE Antennas and Wireless Propagation Letters* 21.6 (2022), pp. 1168–1172. DOI: 10.1109/LAWP.2022.3160733.

[21] Benjamin Fuchs and Sébastien Rondineau. “Array Pattern Synthesis With Excitation Control via Norm Minimization”. In: *IEEE Transactions on Antennas and Propagation* 64.10 (2016), pp. 4228–4234. DOI: 10.1109/TAP.2016.2594300.

[22] Zhi-quan Luo et al. “Semidefinite Relaxation of Quadratic Optimization Problems”. In: *IEEE Signal Processing Magazine* 27.3 (2010), pp. 20–34. DOI: 10.1109/MSP.2010.936019.

[23] Benjamin Fuchs. “Application of Convex Relaxation to Array Synthesis Problems”. In: *IEEE Transactions on Antennas and Propagation* 62.2 (2014), pp. 634–640. DOI: 10.1109/TAP.2013.2290797.

[24] M. Fazel, H. Hindi, and S. Boyd. “Rank minimization and applications in system theory”. In: *Proceedings of the 2004 American Control Conference*. Vol. 4. 2004, 3273–3278 vol.4. DOI: 10.23919/ACC.2004.1384521.